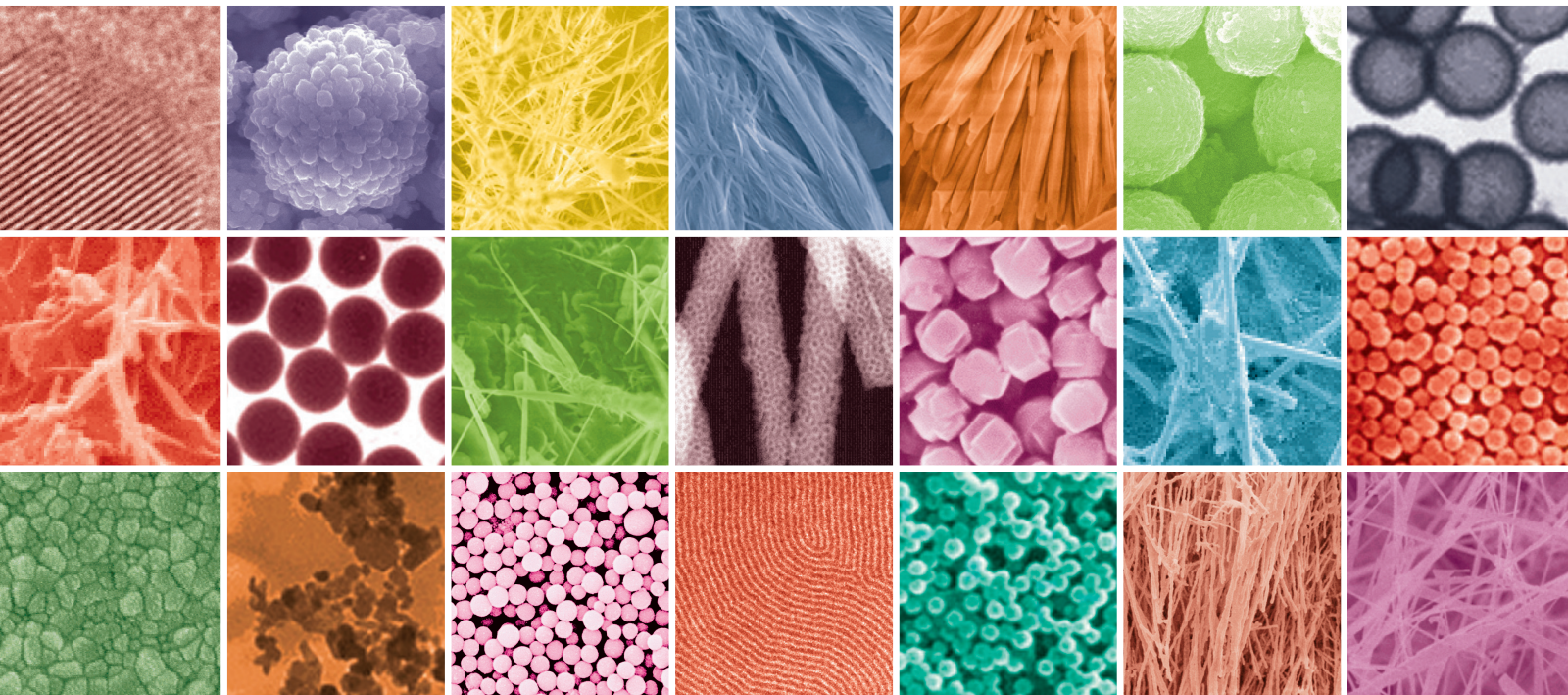


# Modeling of Nanodevices and Nanostructures

Guest Editors: Razali Ismail, Munawar A. Riyadi,  
and Mohammad Taghi Ahmadi





---

# **Modeling of Nanodevices and Nanostructures**

Journal of Nanomaterials

---

## **Modeling of Nanodevices and Nanostructures**

Guest Editors: Razali Ismail, Munawar A. Riyadi,  
and Mohammad Taghi Ahmadi



---

Copyright © 2014 Hindawi Publishing Corporation. All rights reserved.

This is a special issue published in "Journal of Nanomaterials." All articles are open access articles distributed under the Creative Commons Attribution License, which permits unrestricted use, distribution, and reproduction in any medium, provided the original work is properly cited.

## Editorial Board

Katerina E. Aifantis, USA  
Nageh K. Allam, USA  
Margarida Amaral, Portugal  
Xuedong Bai, China  
Lavinia Balan, France  
Enrico Bergamaschi, Italy  
Theodorian Borca-Tasciuc, USA  
C. Jeffrey Brinker, USA  
Christian Brosseau, France  
Xuebo Cao, China  
Shafiq Chowdhury, USA  
Kwang-Leong Choy, UK  
Cui ChunXiang, China  
Miguel A. Correa-Duarte, Spain  
Shadi A. Dayeh, USA  
Ali Eftekhari, USA  
Claude Estournés, France  
Alan Fuchs, USA  
Lian Gao, China  
Russell E. Gorga, USA  
Hongchen Chen Gu, China  
Mustafa O. Guler, Turkey  
John Z. Guo, USA  
Smrati Gupta, Germany  
Michael Harris, USA  
Zhongkui Hong, China  
Michael Z. Hu, USA  
David Hui, USA  
Y.-K. Jeong, Republic of Korea  
Sheng-Rui Jian, Taiwan  
Wanqin Jin, China  
Rakesh K. Joshi, UK  
Zhenhui Kang, China  
Fathallah Karimzadeh, Iran  
Alireza Khataee, Iran

Do K. Kim, Korea  
Alan K. T. Lau, Hong Kong  
Burtrand Lee, USA  
Jun Li, Singapore  
Benxia Li, China  
Xing-Jie Liang, China  
Shijun Liao, China  
Gong-Ru Lin, Taiwan  
Tianxi Liu, China  
Jun Liu, USA  
Songwei Lu, USA  
Daniel Lu, China  
Jue Lu, USA  
Ed Ma, USA  
Gaurav Mago, USA  
Santanu K. Maiti, India  
Sanjay R. Mathur, Germany  
Vikas Mittal, UAE  
Weihai Ni, Germany  
Sherine Obare, USA  
Atsuto Okamoto, Japan  
Abdelwahab Omri, Canada  
Edward A. Payzant, USA  
Kui-Qing Peng, China  
Anukorn Phuruangrat, Thailand  
Mahendra Rai, India  
Suprakas Sinha Ray, South Africa  
Ugur Serincan, Turkey  
Huaiyu Shao, Japan  
Donglu Shi, USA  
Vladimir Sivakov, Germany  
Marinella Striccoli, Italy  
Bohua Sun, South Africa  
Saikat Talapatra, USA  
Nairong Tao, China

Titipun Thongtem, Thailand  
Somchai Thongtem, Thailand  
Alexander Tolmachev, Ukraine  
Valeri P. Tolstoy, Russia  
Tsung-Yen Tsai, Taiwan  
Takuya Tsuzuki, Australia  
Raquel Verdejo, Spain  
Mat U. Wahit, Malaysia  
Zhenbo Wang, China  
Ruiping Wang, Canada  
Shiren Wang, USA  
Cheng Wang, China  
Yong Wang, USA  
Jinquan Wei, China  
Ching-Ping Wong, Hong Kong  
Xingcai Wu, China  
Guodong Xia, Hong Kong  
Ping Xiao, UK  
Zhi Li Xiao, USA  
Yangchuan Xing, USA  
Shuangxi Xing, China  
Nanping Xu, China  
Doron Yadlovker, Israel  
Yingkui Yang, China  
Khaled Youssef, USA  
Kui Yu, Canada  
William W. Yu, USA  
Haibo Zeng, China  
Tianyou Zhai, China  
Renyun Zhang, Sweden  
Bin Zhang, China  
Yanbao Zhao, China  
Lianxi Zheng, Singapore  
Chunyi Zhi, Hong Kong

# Contents

**Modeling of Nanodevices and Nanostructures**, Razali Ismail, Munawar A. Riyadi,  
and Mohammad Taghi Ahmadi  
Volume 2014, Article ID 417127, 2 pages

**Bilayer Graphene Application on NO<sub>2</sub> Sensor Modelling**, Elnaz Akbari, R. Yusof, M. T. Ahmadi,  
A. Enzevae, M. J. Kiani, H. Karimi, and M. Rahmani  
Volume 2014, Article ID 534105, 7 pages

**Gradient Elasticity Formulations for Micro/Nanoshells**, Bohua Sun and E. C. Aifantis  
Volume 2014, Article ID 846370, 4 pages

**Nonlocal Elasticity Theory for Transient Analysis of Higher-Order Shear Deformable Nanoscale Plates**,  
Woo-Young Jung and Sung-Cheon Han  
Volume 2014, Article ID 208393, 8 pages

**Flux Density through Guides with Microstructured Twisted Clad DB Medium**,  
M. A. Baqir and P. K. Choudhury  
Volume 2014, Article ID 629651, 6 pages

**Optimization of DNA Sensor Model Based Nanostructured Graphene Using Particle Swarm  
Optimization Technique**, Hedyeh Karimi, Rubiyah Yusof, Rasoul Rahmani,  
and Mohammad Taghi Ahmadi  
Volume 2013, Article ID 789454, 9 pages

**Influence of Electric Field Coupling Model on the Simulated Performances of a GaN Based Planar  
Nanodevice**, K. Y. Xu, Z. N. Wang, Y. N. Wang, J. W. Xiong, and G. Wang  
Volume 2013, Article ID 124354, 7 pages

**The Effect of Bilayer Graphene Nanoribbon Geometry on Schottky-Barrier Diode Performance**,  
Meisam Rahmani, Razali Ismail, Mohammad Taghi Ahmadi, Mohammad Javad Kiani, Mehdi Saeidmanesh,  
F. A. Hedyeh Karimi, Elnaz Akbari, and Komeil Rahmani  
Volume 2013, Article ID 636239, 8 pages

**Thermodynamic and Theoretical Study of the Preparation of New Buckyballs from Corannulene,  
Coronene, and Circulene**, Hasan R. Obayes, Ghadah H. Alwan, Ahmed A. Al-Amiery,  
Abdul Amir H. Kadhum, and Abu Bakar Mohamad  
Volume 2013, Article ID 451920, 8 pages

## Editorial

# Modeling of Nanodevices and Nanostructures

**Razali Ismail,<sup>1</sup> Munawar A. Riyadi,<sup>2</sup> and Mohammad Taghi Ahmadi<sup>3</sup>**

<sup>1</sup> Faculty of Electrical Engineering, Universiti Teknologi Malaysia (UTM), 81310 Johor Bahru, Johor, Malaysia

<sup>2</sup> Department of Electrical Engineering, Diponegoro University, Tembalang, Semarang 50275, Indonesia

<sup>3</sup> Nanotechnology Research Center, Department of Physics, Urmia University, P.O. Box 165, 11 km Sero, Urmia 57147, Iran

Correspondence should be addressed to Razali Ismail; [razali@fke.utm.my](mailto:razali@fke.utm.my)

Received 16 February 2014; Accepted 16 February 2014; Published 28 April 2014

Copyright © 2014 Razali Ismail et al. This is an open access article distributed under the Creative Commons Attribution License, which permits unrestricted use, distribution, and reproduction in any medium, provided the original work is properly cited.

Since its first development in more than half a century ago, the silicon-based transistors have been experiencing rapid growth following the trend known as Moore's Law. The transistor scaling into nanometer regime has reached decananometer dimension since the last decade, which brings about the unprecedented complexities in the fabrication process, especially in the effort to keep pace with the technology projection. In addition, the conventional device structure that has been around for decades is extremely hard to be scaled further due to many limitations. These obstacles generate broad interests on novel device architectures as well as involvement of new materials other than silicon. The industry is already preparing for the postsilicon era, with the enormous researches in emerging materials such as III-V compounds, SiGe, and carbon as can be observed from the International Technology Roadmap for Semiconductor (ITRS).

In parallel with the fabrication, semiconductor industries rely heavily on simulation to ramp up the prototyping time as well as to reduce the cost in development cycle. Hence, a proper, accurate model for device of interest is crucial to help in producing the necessary evaluation and projection of the final device performance. In the wake of these interests on novel devices, structures and materials alike, a number of modeling approaches have been investigated and formulated, either explicitly, analytically, or computationally intensive. The modeling work now takes greater influence which is crucial for simulating the behavior of those new nanostructures as well as predicting the performance for the future nanodevices. The inclusion of more sophisticated transport phenomena into the model with adopted quantum effect also

adds to the importance, as it is closely associated with the proper explanation of low dimensional structures.

In this special issue, several selected examples of current research efforts related to the modeling approach of nanostructures and nanodevices are presented. The modeling puts into perspective broad interest of the material involved. The paper by W. Y. Jung and S. C. Han elaborated the elastic theory of the nanoscale plate using Eringen's nonlocal differential constitutive relations and higher-order shear deformation theory (HSDT). The solutions of transient dynamic analysis of nanoscale plates are solved using the presented model, which is crucial for better understanding of the motion for such structural arrangement. The role of electric-field coupling on a two-dimensional electron gas (2DEG) GaN based planar nanodevice is modeled by K. Y. Xu et al. Two models are developed and simulated using the approach of 2D ensemble Monte Carlo (EMC) method combined with self-consistent 2D and 3D Poisson equation solution. It is revealed that the different coupling path of electric field contributes to the deviation of the wave shape with the variation of device parameters. The effect of graphene nanoribbon geometry on diode performance is explored by M. Rahmani et al. The model formulated bilayer graphene nanoribbon for Schottky-barrier diode using different stacking arrangements, that is, between a semiconductor (AB stacking) and metal (AA stacking) layers. The simulated model showed a strong dependency of the I-V characteristic on geometry and temperature. The result also showed that it has better performance compared to the silicon-based device for several metrics. H. R. Obayes et al. offer the theoretical study of buckyballs preparation from corannulene, coronene,

and circulene using density functional theory (DFT). Determination of the HOMO energy levels provides necessary information about the stability of the most symmetric buckyball with the most efficient gap energy, which showed good prospect towards solar cell applications.

Another example of microstructure modeling is the twisted clad containing DB medium, presented by M. A. Baqir and P. K. Choudhury. The propagation patterns of flux densities of the guiding structure are explored analytically for the varying pitch angles condition. B. Sun and E. C. Aifantis illustrate how to extend the second author's gradient theory of elasticity to shells. Three formulations are presented based on the implicit gradient elasticity constitutive relation.

As examples of microstructure-based device application, two papers elaborated the use of graphene microstructure for sensor modeling. Gas and chemical sensor, biosensor, and medical sensors are general sensor applications which are useful to human being and for industrial application. One of the best candidates as a detecting material is nanomaterials. When nanomaterials are appropriately engineered, they present a variety of outstanding and adjustable chemical and physical properties which can be used as a sensing element. E. Akbari et al. presented the modeling of bilayer graphene for NO<sub>2</sub> sensor using physical-based approach, while H. Karimi et al. used particle swarm optimization technique in optimizing the DNA sensor model. Both papers offer the understanding of graphene device in complex situation and when dealing with different substances.

We believe that this special issue could provide new insight on different approaches of nanodevices and nanostructure modeling. Whilst this special issue could not cover every aspect, it attempts to offer pointers on recent progress in these areas.

## Acknowledgments

The editors would like to thank the authors and coauthors for their scientific contributions. We also express our sincere gratitude to all reviewers for their valuable time and effort in maintaining the quality of this special issue.

*Razali Ismail  
Munawar A. Riyadi  
Mohammad Taghi Ahmadi*

## Research Article

# Bilayer Graphene Application on NO<sub>2</sub> Sensor Modelling

Elnaz Akbari,<sup>1</sup> R. Yusof,<sup>1</sup> M. T. Ahmadi,<sup>2,3</sup> A. Enzevae,<sup>4</sup> M. J. Kiani,<sup>2</sup>  
H. Karimi,<sup>5</sup> and M. Rahmani<sup>2</sup>

<sup>1</sup> Centre for Artificial Intelligence and Robotics (CAIRO), Universiti Teknologi Malaysia, 54100 Jalan Semarak, Kuala Lumpur, Malaysia

<sup>2</sup> Computational Nanoelectronic Research Group Faculty of Electrical Engineering, Universiti Teknologi Malaysia, 81310 Johor, Malaysia

<sup>3</sup> Nanotechnology Research Center Nanoelectronic Group, Physics Department, Urmia University, Urmia 57147, Iran

<sup>4</sup> Faculty of Mechanical Engineering, Universiti Teknologi Malaysia, 81310 Johor, Malaysia

<sup>5</sup> Malaysia-Japan International Institute of Technology (MJIIT), Universiti Teknologi Malaysia, 54100 Jalan Semarak, Kuala Lumpur, Malaysia

Correspondence should be addressed to R. Yusof; rubiyah@ic.utm.my

Received 11 September 2013; Accepted 9 January 2014; Published 24 April 2014

Academic Editor: Razali Ismail

Copyright © 2014 Elnaz Akbari et al. This is an open access article distributed under the Creative Commons Attribution License, which permits unrestricted use, distribution, and reproduction in any medium, provided the original work is properly cited.

Graphene is one of the carbon allotropes which is a single atom thin layer with sp<sup>2</sup> hybridized and two-dimensional (2D) honeycomb structure of carbon. As an outstanding material exhibiting unique mechanical, electrical, and chemical characteristics including high strength, high conductivity, and high surface area, graphene has earned a remarkable position in today's experimental and theoretical studies as well as industrial applications. One such application incorporates the idea of using graphene to achieve accuracy and higher speed in detection devices utilized in cases where gas sensing is required. Although there are plenty of experimental studies in this field, the lack of analytical models is felt deeply. To start with modelling, the field effect transistor- (FET-) based structure has been chosen to serve as the platform and bilayer graphene density of state variation effect by NO<sub>2</sub> injection has been discussed. The chemical reaction between graphene and gas creates new carriers in graphene which cause density changes and eventually cause changes in the carrier velocity. In the presence of NO<sub>2</sub> gas, electrons are donated to the FET channel which is employed as a sensing mechanism. In order to evaluate the accuracy of the proposed models, the results obtained are compared with the existing experimental data and acceptable agreement is reported.

## 1. Introduction

Currently, there are various kinds of hazardous gases which are harmful to the organic life and are difficult to observe and sense [1–3]. Therefore, a sensor or a detection system is a necessary component in environments where human presence is inevitable. In the case of gas sensors, the best sensor would be defined as one that is able to detect even one molecule or atom of the chemical or gas [4–6]. Gas sensor efficiency can be improved significantly by the state-of-the-art technology [7–11]. Sensor technology has become omnipresent in the modern life, and nanosensor provides the foundation for highly developed electronic technology. According to the studies, graphene is one of the crystalline allotropes by two-dimensional network of carbon atoms arranged on a honeycomb structure [12–14]. Also, graphene

has been widely implemented for the detection of various chemical materials including NO<sub>2</sub>, NH<sub>3</sub>, CO<sub>2</sub>, H<sub>2</sub>O, and CO because of its excellent adsorption properties and carrier mobility [15, 16]. Bilayer graphene (BLG) is the stack of two graphene layers, due to special features such as electrical, physical, and optical properties, and is known as an appropriate material to be used in nanotechnology especially in the sensor area [17, 18].

The twisted configuration and Bernal stacking are two common structures of bilayer graphene. In the former, the layers are rotating toward each other while, in the latter, half of the carbon atoms in one layer are standing over the other half [19, 20]. The electrical and optical features of bilayer graphene can be influenced by orientation and stacking order. The AA-stacked configuration is metallic, but the AB-stacked configuration, which is in our focus, behaves

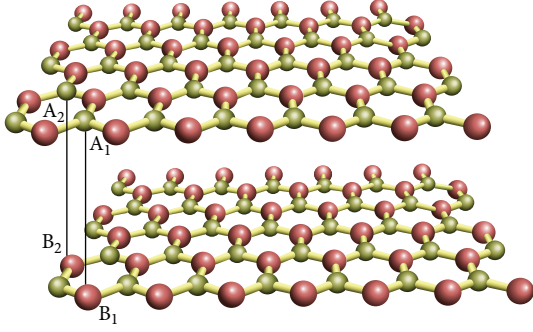


FIGURE 1: The schematic of bilayer graphene (AB-stacked configuration).

like a semiconductor material [21, 22]. In the AB structure of bilayer graphene with hexagonal carbon lattice, the atoms located on the top layer of BLG are  $A_1$  and  $A_2$ , whereas atoms on the bottom layer of BLG are labelled  $B_1$  and  $B_2$  [18] as shown in Figure 1.

One of the most interesting properties in BLG is its band structure. Through theoretical studies it has been assumed that, by applying a perpendicular electric field, the band gap can be induced by reducing the asymmetry of two graphene layers in the BLG [19]. The controllable band gap is one of the most excellent properties of BLG that makes it a promising material in nanotechnology. In Figure 2(a), the band structure of the unbiased BLG with no external perpendicular electric fields is shown. It demonstrates that the BLG is a zero gap semiconductor with four parabolic bands, where two inner bands contact each other near the Dirac points at zero energy and the two outer bands are separated by the interlayer hopping energy,  $\pm t$  [23, 24].

In the biased BLG, as shown in Figure 2(b), by applying a perpendicular electric field, a band gap is opened which is given by [26]

$$E_g = \frac{Vt_{\perp}}{\sqrt{V^2 + t_{\perp}^2}}, \quad (1)$$

where  $V = V_1 - V_2$  is the potential energy difference between the first and second layers and  $V_1$  and  $V_2$  are the potential energy of the first and second layers, respectively. The parameter  $V$  can be controlled externally; therefore, by adjusting  $V$ , the band gap can be tuned [25].

## 2. The Proposed Model

The sensitivity of graphene to the miniature applied voltage can be used in sensor technology. In Figure 3, nanosensor detection method is illustrated schematically. In this model, the bilayer graphene as a substrate of gas sensor has been used. As can be seen in the figure, it looks similar to the conventional field effect transistors (FET) which include a source metal, a drain metal, a silicon back gate, and a gate insulator [27]. A graphene channel connects the source and drain electrodes, a dielectric barrier layer ( $\text{SiO}_2$ ) separates the gate from the channel, and  $\text{SiO}_2$  is used under the graphene

as a dielectric layer while silicon acts as a back gate. When gas molecules attach to the surface or edges of CNT, carrier concentration will change. Due to this variability, the drain source current is a measurable parameter. This platform is employed in our model as a FET-based sensor structure [28].

The threshold voltage ( $V_{\text{TH}}$ ) of a MOSFET is usually defined as the gate voltage where an inversion layer forms at the interface between the insulating layer (oxide) and the substrate (body) of the transistor. MOSFET is a device used for amplifying or switching electronic signals. When the gate-source voltage is smaller than the threshold voltage ( $V_{\text{GS}} < V_{\text{TH}}$ ), there will be no conduction between the source and the drain, and the switch will be off. In contrast, when  $V_{\text{GS}} > V_{\text{TH}}$ , the gate will attract electrons, including an n-type conductive channel in the substrate below the oxide. Electrons will flow between n-doped terminals and the switch will be on.

The tight-binding method has been used to calculate the biased energy of BLGs, which indicates energy dispersion of BLG as follows [29, 30]:

$$E(K) = \frac{V_1 + V_2}{2} \pm \sqrt{\epsilon_k^2 + \frac{V^2}{4} + \frac{t_{\perp}^2}{2} \pm \frac{1}{2} \sqrt{4(V^2 + t_{\perp}^2)\epsilon_k^2 + t_{\perp}^4}}, \quad (2)$$

where  $\epsilon_k$  is the electron's dispersion in monolayer graphene and  $t_{\perp} = 0.32 \text{ eV}$  is the interlayer hopping energy. The wave vector in which the smallest gap is observed is given by

$$k_g = \frac{V}{2v_F\hbar} \sqrt{\frac{V^2 + 2t_{\perp}^2}{V^2 + t_{\perp}^2}}, \quad (3)$$

where the  $v_F \approx 1 \times 10^6 \text{ m}\cdot\text{s}^{-1}$  is the Fermi velocity [5] and  $\hbar$  is the reduced Planck constant. Near  $k_g$  the energy dispersion can be written as [31]

$$E(k) = \frac{E_g}{2} + \frac{\hbar^2}{2m^*} (|k| - k_g)^2 + \frac{V_1 + V_2}{2}, \quad (4)$$

where  $k = k_x\hat{i} + k_y\hat{j}$  and  $m^*$  is the effective mass in BLG. The density of states for BLG which indicates the number of states for each interval of energy at each energy level that can be occupied by electrons can be written as

$$\text{DOS} = \frac{\Delta n}{A\Delta E} = \left( \frac{\hbar^2}{m^*} \frac{(k - k_g)}{k} 2\pi \right)^{-1} = \frac{km^*}{2\pi\hbar^2 (k - k_g)}. \quad (5)$$

The velocity of electrons is directly proportional to the value of DOS at any instance. Average velocity of carriers in the first subband in bilayer graphene can be obtained by the accumulative velocity of all carriers divided by the number of carriers. The carrier drift velocity has been reported to be formulated in the following form [32]:

$$v = \int \frac{|\nu| \text{DOS}(E) F(E) dE}{n}. \quad (6)$$

From the kinetic energy principle,  $|\nu| = \sqrt{2E/m}$ ,  $\text{DOS}(E)$  is density of states,  $F(E) = 1/(1 + e^{(E-E_f)/K_B T})$  is the Fermi-Dirac distribution function which gives the probability of

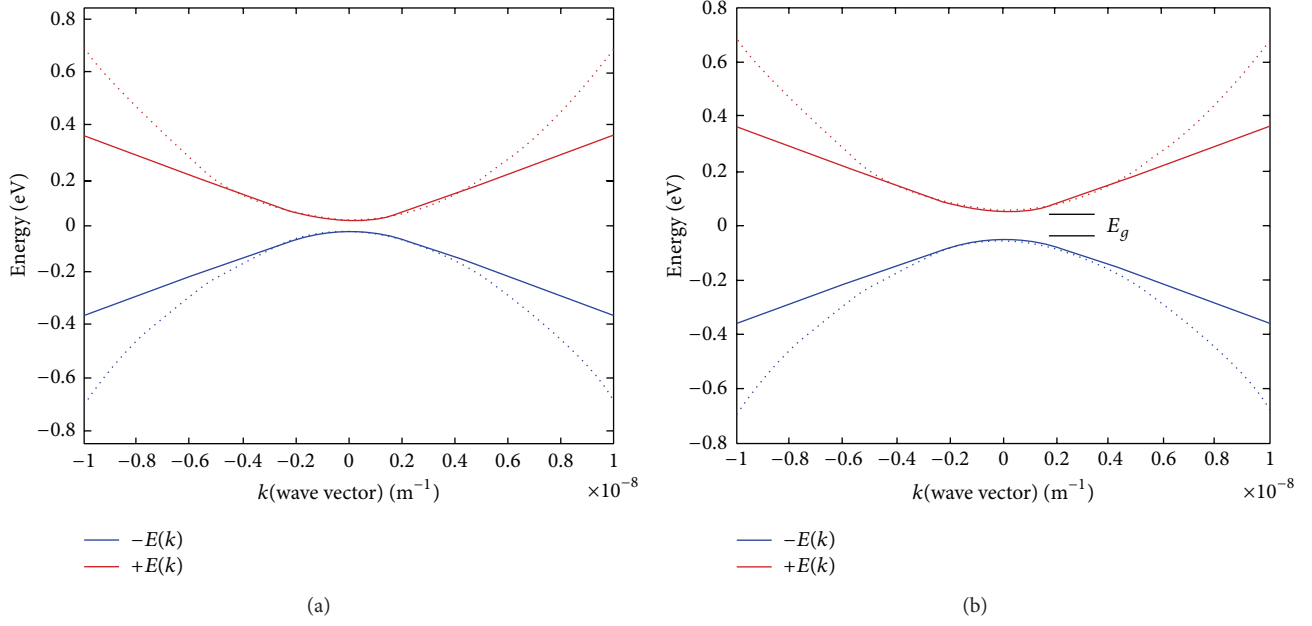


FIGURE 2: Band structure of BLG near the Dirac points for (a)  $V = 0$  (unbiased BLG) and (b)  $V \neq 0$  (biased BLG) [25].

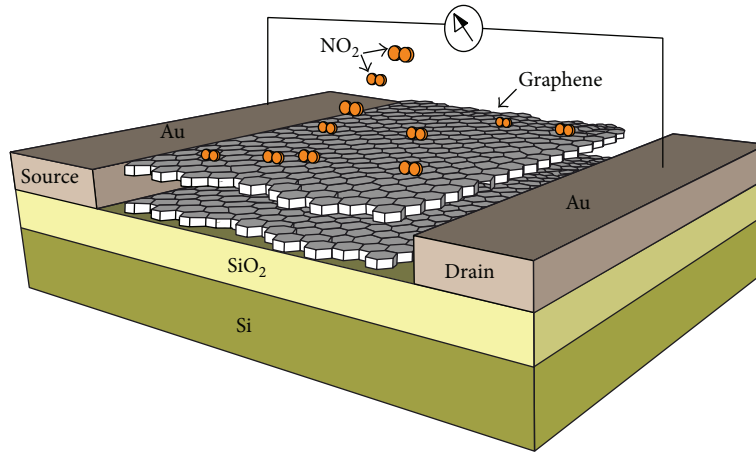


FIGURE 3: Proposed structure of gas sensor based on bilayer graphene.

occupation of a state at any energy level, and  $n$  is carrier concentration [33]. Hence, the integral of the numerator in (6) with respect to  $E$  can be rewritten as

$$\int |\nu| \text{DOS}(E) F(E) dE = \frac{1}{\pi \hbar^2} \int \frac{Ek}{(k - k_g)} \frac{1}{1 + e^{(E - E_f)/k_B T}} dE, \quad (7)$$

where  $k = \pm [2m^*(E - E_c)/\hbar^2]^{1/2} + k_g$ , giving

$$\int |\nu| \text{DOS}(E) F(E) dE = \frac{1}{\pi \hbar^2} \left( \int \frac{E}{1 + e^{(E - E_f)/k_B T}} dE \right.$$

$$\left. + \frac{k_g \hbar}{\sqrt{2m^*}} \int \frac{(E - E_c)^{-1/2}}{1 + e^{(E - E_f)/k_B T}} dE \right). \quad (8)$$

It has been attempted to write (8) in a form which can be solved using the Fermi integrals. The obtained equation is as follows:

$$\int |\nu| \text{DOS}(E) F(E) dE = \frac{(K_B T)^2}{\pi \hbar^2} \int \frac{x}{1 + e^{(x - \eta)}} dx + \frac{K_B T E_c}{\pi \hbar^2} \int \frac{dx}{1 + e^{(x - \eta)}} \quad (9)$$

$$+ \frac{K_B T k_g \hbar}{\pi \hbar^2 \sqrt{2m^*} \sqrt{K_B T}} \int \frac{x^{-1/2}}{1 + e^{(x - \eta)}} dx$$

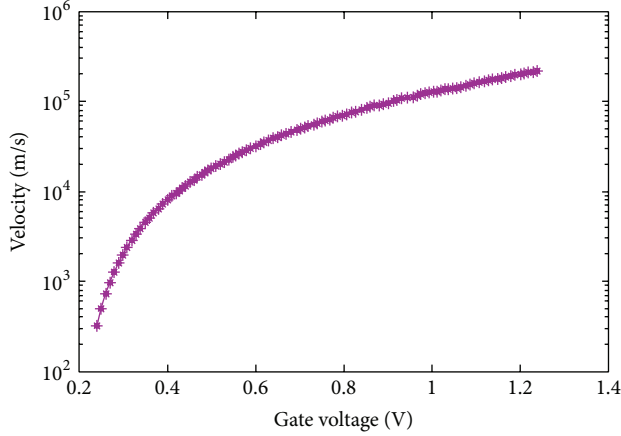
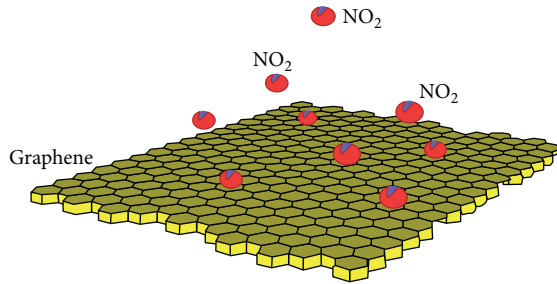


FIGURE 4: The velocity of BLG.

FIGURE 5: Schematic of NO<sub>2</sub> adsorption processes by surface area of graphene.

in which the orders of  $x$  in the numerator of the integrands are 1, 0, and  $-1/2$ , thus making the integrals equivalent to the Fermi integrals of orders 1, 0, and  $-1/2$ , respectively. This can finally give the following equation [34]:

$$\nu = \left[ \frac{(K_B T)^2}{\pi \hbar^2} f(1) + \frac{K_B T E_c}{\pi \hbar^2} f(0) + \frac{K_B T k_g}{\pi \hbar \sqrt{2m K_B T}} f\left(-\frac{1}{2}\right) \right] \times n^{-1}, \quad (10)$$

in which  $f(1)$ ,  $f(0)$ , and  $f(-1/2)$  are the Fermi integral of orders 1, 0, and  $-1/2$ , respectively. For the details on the derivation and mathematical representation of the Fermi integrals, the reader is referred to [34]. Velocity is evaluated in Figure 4 based on (10) [35].

As can be seen in Figure 5, when the sensor is exposed to gas, according to the chemical reaction between graphene and gas molecules, graphene experiences a change in the velocity of its carriers which can in turn cause alterations in the current and channel voltage. In other terms, the electron exchange between the gas and the surface of the graphene creates new carriers which change the velocity of electrons [36].

It can be concluded that the velocity of electrons in the presence of gas is equal to that of the no-gas state plus the

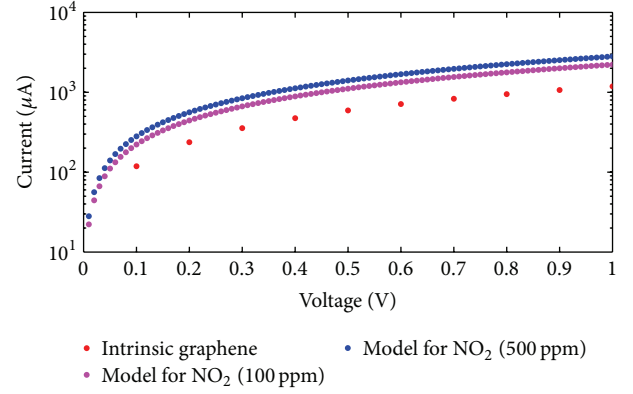


FIGURE 6: The comparison of current-voltage characteristics for 100 ppm and 500 ppm and intrinsic graphene based on proposed model.

velocity change when graphene is exposed to gas. Consider the following:

$$\nu_{\text{with gas}} = \nu_{\text{without gas}} + \nu_{\text{gas injected}}. \quad (11)$$

From this, the current-voltage relation can be derived as follows:

$$I = nq\nu A, \quad (12)$$

where  $n$  is charge carrier density,  $q$  is electrical charge,  $\nu$  is drift velocity of the charge carriers, and  $A$  is the area in which the charges are moving. In Figure 6, the current-voltage characteristic of intrinsic graphene exposed to ambient air only as well as the current-voltage characteristic of BLG based NO<sub>2</sub> sensor for graphene under 100 ppm and 500 ppm NO<sub>2</sub> concentration is plotted. By current-voltage characteristic of the presented model, it is demonstrated that current of gas sensor rises with increasing the NO<sub>2</sub> concentration. Therefore, it is notable that, based on the supposed model sensor,  $I$ - $V$  characteristic is controlled by NO<sub>2</sub> concentration.

When the sensor is exposed to the gas, the density of states can be divided into two parts; one is the density of states without gas  $\text{DOS}_{\text{WOG}}(E)$  and the second parameter is the density of states with gas proportional to  $\alpha F$ , which depends on different values of NO<sub>2</sub> gas concentration. Consider the following:

$$\text{DOS} = \text{DOS}_{\text{WOG}} + \text{DOS}_{\text{gas injected}}, \quad (13)$$

where  $\text{DOS}_{\text{gas injected}} \approx \alpha F$ .

In our study,  $\alpha$  is our control parameter; that is, by heuristically changing the values of  $\alpha$ , we attempt to set the results from the proposed model as close to the experimental results as possible. According to the relation between the

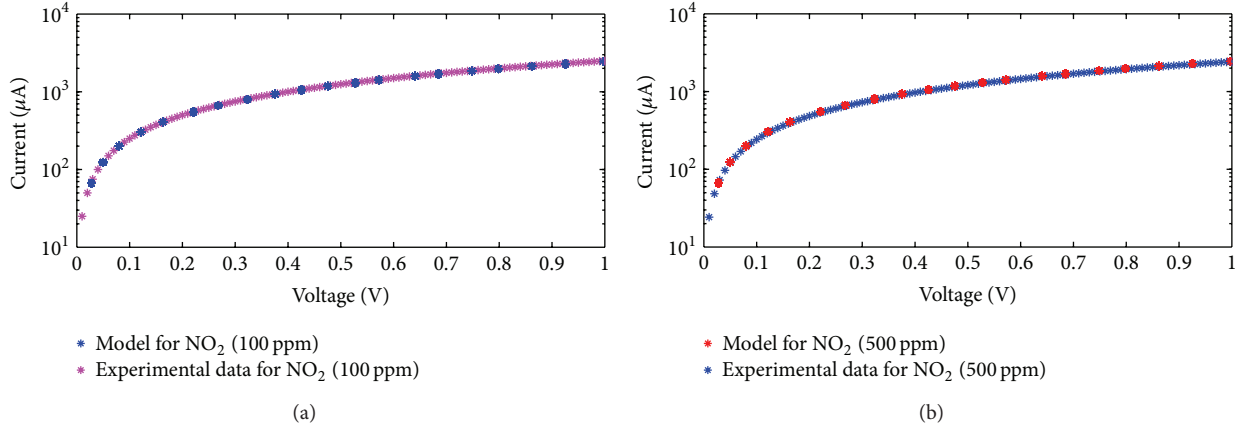


FIGURE 7: The current-voltage characteristics for (a) 100 ppm and (b) 500 ppm.

TABLE 1: Different  $F$  values with  $\alpha$  parameter.

Carrier concentration ( $F$ )	Parameter ( $\alpha$ )
100 ppm	0.077
500 ppm	0.016

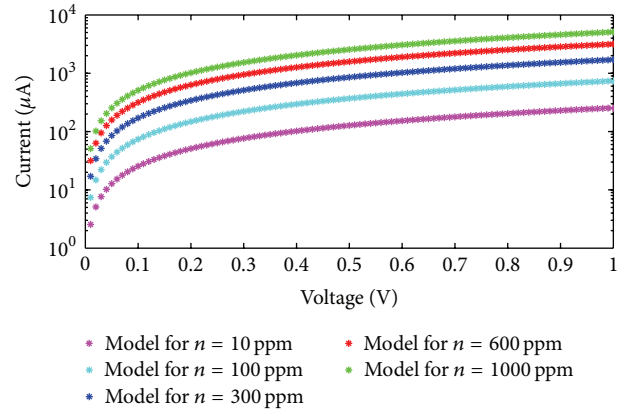
control parameter and density of states, we can write the following:

$$\begin{aligned}
 \nu_{\text{total}} &= \left[ \frac{(K_B T)^2}{\pi \hbar^2} f(1) + \frac{K_B T E_c}{\pi \hbar^2} f(0) \right. \\
 &+ \frac{K_B T k_g}{\pi \hbar \sqrt{2m K_B T}} f\left(-\frac{1}{2}\right) + \frac{2\alpha F}{m^*} (K_B T)^2 f(1) \\
 &\left. + \frac{2\alpha F}{m^*} K_B T E_c f(0) \right] \times n^{-1}, \quad (14)
 \end{aligned}$$

where  $n$  is the carrier concentration equal to  $n = 10^{16}$  for two-dimensional bilayer graphene [35].

The velocity of the graphene-based FET devices is influenced by the number of carriers changing in the channel. FET-based graphene with high sensitivity was applied to detect the  $\text{NO}_2$  gas, based on velocity variations. As depicted in Figures 7(a) and 7(b), the velocity of channel will change due to the adsorption of  $\text{NO}_2$  to the surface of the FET channel. The performance of graphene-based gas sensor under exposure of 100 ppm and 500 ppm of  $\text{NO}_2$  gas is evaluated and the analytical results of the proposed model for gas sensor with appropriate parameters are compared with the experimental data extracted from [16] which shows a good agreement. It is evident in the figure that the points calculated and obtained from our model satisfactorily coincide with the measurement data.

In the suggested model, different carrier concentrations are demonstrated in the form of  $\alpha$  parameter which is presented in Table 1.

FIGURE 8:  $I$ - $V$  characteristic of different values of  $\text{NO}_2$  carrier concentration.

According to the analytical model,  $\alpha$  is proposed as the controlling parameter of gas concentration. The analytic model based on data extracted can be written as follows:

$$\alpha = a e^{bx}. \quad (15)$$

Referring to the analytical model, the velocity will be enhanced as the amount of gas concentration increases. According to the extracted data, parameters  $a$  and  $b$  are calculated as  $a = 0.370$  and  $b = -1.57$ .

It is evident in Figure 8 that  $I$ - $V$  characteristic curve can be controlled by the carrier concentration factor. The current rises as a result of increase in the carrier concentration.

### 3. Conclusion

Graphene indicates amazing carrier transport properties and high sensitivity at the single molecule level which makes it a promising material for nanosensor applications. An innovative analysis of matching models using different values has been presented in this work to verify that the conductance of the graphene-based gas sensor is increased at higher carrier concentrations.  $\text{NO}_2$  gas effect in the FET channel

region in the form of carrier density variation influencing the carrier velocity is further modelled, and current-voltage characteristic of a bilayer graphene (BLG) as a NO<sub>2</sub> gas sensor is reported. Injected carriers from NO<sub>2</sub> on the carrier concentration of bilayer graphene surface are monitored. Furthermore, injected carriers as a function of gas concentration ( $f$ ) are demonstrated. It was shown that, as carrier concentration increases, the control parameter,  $\alpha$ , decreases. Finally, for the purpose of verification,  $I$ - $V$  characteristic of gas sensor in exposure to NO<sub>2</sub> is investigated and a comparative study between the model and experimental data from literature shows an acceptable agreement.

## Conflict of Interests

The authors declare that there is no conflict of interests regarding the publication of this paper.

## Acknowledgments

The authors would like to thank Ministry of Education Malaysia and Universiti Teknologi Malaysia for funding this research project through a research Grant (GUP-04H40) titled “Dimension Reduction & Data Clustering for High Dimensional & Large Datasets”.

## References

- [1] M. Ettore, V. la Ferrara, M. Mara, T. Polichetti, N. Ivana, and G. di Francia, “Gas sensors based on graphene: comparison of two different fabrication approaches,” *Chimica Oggi*, vol. 29, no. 1, pp. 39–41, 2011.
- [2] H. Yu, P. Xu, X. Xia et al., “Micro-/nanocombined gas sensors with functionalized mesoporous thin film self-assembled in batches onto resonant cantilevers,” *IEEE Transactions on Industrial Electronics*, vol. 59, no. 12, pp. 4881–4887, 2012.
- [3] E. Akbari, M. T. Ahmadi, M. J. Kiani et al., “Monolayer graphene based CO<sub>2</sub> gas sensor analytical model,” *Journal of Computational and Theoretical Nanoscience*, vol. 10, no. 6, pp. 1301–1304, 2013.
- [4] B. Huang, Z. Li, Z. Liu et al., “Adsorption of gas molecules on graphene nanoribbons and its implication for nanoscale molecule sensor,” *Journal of Physical Chemistry C*, vol. 112, no. 35, pp. 13442–13446, 2008.
- [5] M. Zhou, Y.-H. Lu, Y.-Q. Cai, C. Zhang, and Y.-P. Feng, “Adsorption of gas molecules on transition metal embedded graphene: a search for high-performance graphene-based catalysts and gas sensors,” *Nanotechnology*, vol. 22, no. 38, Article ID 385502, 2011.
- [6] E. Akbari, M. T. Ahmadi, Y. Rubiyah, M. H. Ghadiry, and M. Saeidmanesh, “Gas concentration effect on channel capacitance in graphene based sensors,” *Journal of Computational and Theoretical Nanoscience*, vol. 10, no. 10, pp. 2449–2452, 2013.
- [7] H. Jiang, “Chemical preparation of graphene-based nanomaterials and their applications in chemical and biological sensors,” *Small*, vol. 7, no. 17, pp. 2413–2427, 2011.
- [8] S. Kochmann, T. Hirsch, and O. S. Wolfbeis, “Graphenes in chemical sensors and biosensors,” *TrAC Trends in Analytical Chemistry*, vol. 39, 2012.
- [9] E. Akbari, R. Yousof, M. T. Ahmadi et al., “The effect of concentration on gas sensor model based on graphene nanoribbon,” *Neural Computing and Applications*, vol. 24, no. 1, pp. 143–146, 2014.
- [10] S. Okude, “Detection of chemical reactivity of intramolecular atom involves setting arbitrary atoms of intramolecular atom to alpha, and calculating magnitude of value of difference of preset parameter as index of chemical reactivity”.
- [11] M. Rahmani, “Analytical modeling of monolayer graphene-based NO<sub>2</sub> sensor,” *Sensor Letters*, vol. 11, no. 2, pp. 270–275, 2013.
- [12] O. Leenaerts, B. Partoens, and F. M. Peeters, “Adsorption of H<sub>2</sub>O, NH<sub>3</sub>, CO, NO<sub>2</sub>, and NO on graphene: a first-principles study,” *Physical Review B—Condensed Matter and Materials Physics*, vol. 77, no. 12, Article ID 125416, 2008.
- [13] Y.-H. Zhang, Y.-B. Chen, K.-G. Zhou et al., “Improving gas sensing properties of graphene by introducing dopants and defects: a first-principles study,” *Nanotechnology*, vol. 20, no. 18, Article ID 185504, 2009.
- [14] X.-L. Wei, Y.-P. Chen, W.-L. Liu, and J.-X. Zhong, “Enhanced gas sensor based on nitrogen-vacancy graphene nanoribbons,” *Physics Letters A: General, Atomic and Solid State Physics*, vol. 376, no. 4, pp. 559–562, 2012.
- [15] S. Hadlington, “Graphene sensor achieves ultimate sensitivity,” *Chemistry World*, vol. 4, no. 9, p. 29, 2007.
- [16] G. Ko, H.-Y. Kim, J. Ahn, Y.-M. Park, K.-Y. Lee, and J. Kim, “Graphene-based nitrogen dioxide gas sensors,” *Current Applied Physics*, vol. 10, no. 4, pp. 1002–1004, 2010.
- [17] A. Das, B. Chakraborty, and A. K. Sood, “Probing single and bilayer graphene field effect transistors by Raman spectroscopy,” *Modern Physics Letters B*, vol. 25, no. 8, pp. 511–535, 2011.
- [18] K.-T. Lam, C. Lee, and G. Liang, “Bilayer graphene nanoribbon nanoelectromechanical system device: a computational study,” *Applied Physics Letters*, vol. 95, no. 14, Article ID 143107, 2009.
- [19] S. M. Mousavi, M. T. Ahmadi, J. F. Webb et al., “Bilayer graphene nanoribbon carrier statistics in the degenerate regime,” in *Proceedings of the 4th Global Conference on Power Control and Optimization*, pp. 180–183, December 2010.
- [20] M. T. A. M. J. Kiani, E. akbari, M. Rahmani, H. karimi, and F. K. C. harun, “Analytical modeling of bilayer graphene based biosensor,” *Journal of Computational and Theoretical Nanoscience (CTN)*, 2012.
- [21] H. Hatami, N. Abedpour, A. Qaiumzadeh, and R. Asgari, “Conductance of bilayer graphene in the presence of a magnetic field: effect of disorder,” *Physical Review B—Condensed Matter and Materials Physics*, vol. 83, no. 12, Article ID 125433, 2011.
- [22] T. Yu, E.-K. Lee, B. Briggs, B. Nagabhirava, and B. Yu, “Reliability study of bilayer graphene—material for future transistor and interconnect,” in *Proceedings of the IEEE International Reliability Physics Symposium (IRPS '10)*, pp. 80–83, May 2010.
- [23] N. A. Amin, M. T. Ahmadi, Z. Johari, S. M. Mousavi, and R. Ismail, “Effective mobility model of graphene nanoribbon in parabolic band energy,” *Modern Physics Letters B*, vol. 25, no. 10, pp. 739–745, 2011.
- [24] M. T. Ahmadi, Z. Johari, N. A. Amin, A. H. Fallahpour, and R. Ismail, “Graphene nanoribbon conductance model in parabolic band structure,” *Journal of Nanomaterials*, vol. 2010, Article ID 753738, 4 pages, 2010.
- [25] M. T. Ahmadi, Z. Johari, N. A. Amin, and R. Ismail, “Band energy effect on carrier velocity limit in graphene nanoribbon,” *Journal of Experimental Nanoscience*, vol. 7, no. 1, pp. 62–73, 2012.

- [26] J. Nilsson, A. H. C. Neto, F. Guinea, and N. M. R. Peres, “Electronic properties of bilayer and multilayer graphene,” *Physical Review B—Condensed Matter and Materials Physics*, vol. 78, no. 4, Article ID 045405, 2008.
- [27] E. F. W. Olthuis, K. Erik, and A. van den Berg, *Sensing with FETs—Once, Now and Future*, UTpublications, 2007.
- [28] F. Schwierz, “Graphene transistors,” *Nature Nanotechnology*, vol. 5, no. 7, pp. 487–496, 2010.
- [29] M. Cheli, G. Fiori, and G. Iannaccone, “A semianalytical model of bilayer-graphene field-effect transistor,” *IEEE Transactions on Electron Devices*, vol. 56, no. 12, pp. 2979–2986, 2009.
- [30] M. Rahmani, R. Ismail, M. T. Ahmadi et al., “The effect of bilayer graphene nanoribbon geometry on schottky-barrier diode performance,” *Journal of Nanomaterials*, vol. 2013, Article ID 636239, 8 pages, 2013.
- [31] J. I. Väyrynen and T. Ojanen, “Electronic properties of graphene multilayers,” *Physical Review Letters*, vol. 107, no. 10, Article ID 109901, 2011.
- [32] M. T. Ahmadi, R. Ismail, M. L. P. Tan, and V. K. Arora, “The ultimate ballistic drift velocity in carbon nanotubes,” *Journal of Nanomaterials*, vol. 2008, no. 1, Article ID 769250, 2008.
- [33] M. T. Ahmadi and R. Ismail, “Graphene nanoribbon fermi energy model in parabolic band structure,” in *Proceedings of the UKSim/AMSS 1st International Conference on Intelligent Systems, Modelling and Simulation (ISMS '10)*, pp. 401–405, January 2010.
- [34] R. Kim and M. Lundstrom, *Notes on Fermi-Dirac Integrals*, 2nd edition, 2008.
- [35] M. Saeidmanesh, M. T. Ahmadi, and M. H. Ghadiry, “Perpendicular electric field effect on bilayer graphene carrier statistic,” *Journal of Computational and Theoretical Nanoscience*, vol. 10, no. 9, 2013.
- [36] J. Xia, F. Chen, J. Li, and N. Tao, “Measurement of the quantum capacitance of graphene,” *Nature Nanotechnology*, vol. 4, no. 8, 509 pages, 2009.

## Research Article

# Gradient Elasticity Formulations for Micro/Nanoshells

Bohua Sun<sup>1</sup> and E. C. Aifantis<sup>2,3,4</sup>

<sup>1</sup> Centre for Mechanics and Technology, Faculty of Engineering, Cape Peninsula University of Technology, Cape Town, South Africa

<sup>2</sup> Lab of Mechanics and Materials, Polytechnic School, Aristotle University, 54124 Thessaloniki, Greece

<sup>3</sup> Michigan Technological University, Houghton, MI 49931, USA

<sup>4</sup> King Abdulaziz University, Jeddah 21589, Saudi Arabia

Correspondence should be addressed to Bohua Sun; [sunb@cput.ac.za](mailto:sunb@cput.ac.za)

Received 4 October 2013; Accepted 23 January 2014; Published 20 February 2014

Academic Editor: Razali Ismail

Copyright © 2014 B. Sun and E. C. Aifantis. This is an open access article distributed under the Creative Commons Attribution License, which permits unrestricted use, distribution, and reproduction in any medium, provided the original work is properly cited.

The focus of this paper is on illustrating how to extend the second author's gradient theory of elasticity to shells. Three formulations are presented based on the implicit gradient elasticity constitutive relation  $(1 - l_d^2 \nabla^2) \sigma_{ij} = C_{ijkl} (1 - l_s^2 \nabla^2) \varepsilon_{kl}$  and its two approximations  $(1 + l_s^2 \nabla^2 - l_d^2 \nabla^2) \sigma_{ij} = C_{ijkl} \varepsilon_{kl}$  and  $\sigma_{ij} = C_{ijkl} (1 + l_d^2 \nabla^2 - l_s^2 \nabla^2) \varepsilon_{kl}$ .

## 1. Introduction

Many unexpected applications were found due to superior thermochemomechanical and optoelectromagnetic material properties noted at the nanoscale. Nanoscale structures, such as nanobeams, nanoplates, and nanoshells, were used in many MEMS and NEMS applications. Therefore, understanding the static and dynamic behaviour of them is important for reliable design of micro- and nanodevices.

Experimental studies are generally difficult at the nanoscale due to resolution limitation of available nanoprobes. Molecular dynamics (MD) experiments were therefore normally employed to understand nanoscale behavior. Unfortunately, MD studies are limited to small number of atoms and short time intervals. Continuum models were then proposed as an alternative solution method.

For mechanical behaviour modelling of nanostructures, the classical continuum mechanics models are not adequate because these models only contain bulk material properties and cannot capture inhomogeneously evolving microstructures and related size effects. To simulate nanostructures, a number of continuum theories have been used to predict the influence of nanoscale effects, such as couple stress and

Cosserat theories, nonlocal elasticity, and gradient elasticity. The gradient theory is an extension of classical theory to include additional higher-order spatial derivatives of strain and/or stress, as well as (internal) acceleration. It has been shown to be a powerful alternative tool for dealing with nanostructures without resorting to expensive MD computations.

The use of gradient elasticity to simulate the mechanical behaviour of materials and structures is not a novel idea—in fact, it has been advocated more than a century and a half ago; however, the scope has varied widely over the years. Pioneer work was done by Cauchy in 1850s [1, 2]. Cauchy suggested the use of higher-order spatial derivatives in the continuum equations describing elastic properties in order to approximate the behaviour of discrete lattice models with more accuracy, whereby the size of the elementary volume appeared as an additional constitutive parameter. As a followup of Cauchy's initial work on the subject, one may consider Cosserat's theory developed half a century later (early 1900s) [3]. Mindlin's [4, 5] strain gradient theory of elasticity involving five extra phenomenological constants should be mentioned, as reference to it is being made by researchers today. In modern times, Eringen [6–9] derived

a simple stress-gradient elasticity model from his earlier integral nonlocal theory, but interest in this work has remained largely dormant till the late 1990s. In early 1990s, Aifantis [10] proposed a robust strain gradient theory of elasticity, which has led to notably straightforward finite element implementations. This has been generalized in Aifantis [11, 12] to include both strain and stress gradients, thus incorporating the effects of both Eringen's and Aifantis' ingredients of gradient theories. For details, the reader should consult the articles listed in the first six references provided in the bibliography, as well as in Eringen's book [9] also listed there. In the last reference, an initial effort by the first author to apply gradient theory to nanoshells and nanoplates is outlined.

The key issue of formulations of gradient shell theory is how to fit the new gradient constitution equation into the general framework of shell theory. In this short paper, we will restrict ourselves only on that issue.

## 2. Linear Shell Theories Formulation [13]

The most common shell theories are those based on linear elasticity concepts. Linear shell theories predict adequately stresses and deformations for shells exhibiting small elastic deformations; that is, deformations for which it is assumed that the equilibrium equation conditions for deformed shell surfaces are the same as if they were not deformed, and Hooke's law applies. For the purpose of analysis, a shell may be considered as a three-dimensional body, and the methods of the theory of linear elasticity may then be applied. However, a calculation based on these methods will generally be very difficult and complicated. In the theory of shells, an alternative simplified method is therefore employed. According to this method and adapting some hypotheses, the 3D problem of shell equilibrium and straining may be reduced to the analysis of its middle surface only; that is, the given shell, as discussed earlier as a thin plate, may be regarded as some 2D body. In the development of thin shell theories, simplification is accomplished by reducing the shell problems to the study of deformations of the middle surface.

Shell theories of varying degrees of accuracy were derived, depending on the degree to which the elasticity equations were simplified. The approximations necessary for the development of an adequate theory of shells have been the subject of considerable discussions among investigators in the field. We present below a brief outline of elastic shell theories in an historical context.

Love [14] was the first investigator to present a successful approximation shell theory based on classical linear elasticity. To simplify the strain-displacement relationships and, consequently, the constitutive relations, Love applied, to the shell theory, the Kirchhoff hypotheses developed originally for the plate bending theory, together with the small deflection and thinness of the shell assumptions. This set of assumptions is commonly called the Kirchhoff-Love assumptions. The Love theory of thin elastic shells is also referred to as the first-order approximation shell theory. In spite of its popularity and common character, Love's theory was not free from

some deficiencies, including its inconsistent treatment of small terms, where some were retained and others were rejected, although they were of the same order. This meant that, for certain shells, Love's differential operator matrix on the displacements, in the equations of equilibrium, became unsymmetric. Obviously, this violated Betti's theorem of reciprocity. Love's theory [14] also contained some other inconsistencies. The need for a mathematically rigorous two-dimensional set of the shell equations employing the Kirchhoff-Love assumptions led to different versions of the first order approximation theories.

The middle surface of the shell is determined by the parametric representation  $\mathbf{r} = \mathbf{r}(\theta^1, \theta^2)$ . The covariant base vectors of the middle surface are defined by  $\mathbf{a}_\alpha = \mathbf{r}_{,\alpha}$ , the comma notation being used to denote partial derivative with respect to the parameters. The metric tensors of a surface are defined by  $a_{\alpha\beta} = \mathbf{a}_\alpha \cdot \mathbf{a}_\beta = a_{\beta\alpha}$ ,  $a^{\alpha\lambda} a_{\lambda\beta} = \delta_\beta^\alpha$ , where  $a_{\alpha\beta}$  and  $a^{\alpha\beta}$  are covariant and contravariant symmetric tensors of order two, respectively. The contravariant base vectors of a surface are given by  $\mathbf{a}^\alpha = a^{\alpha\beta} \mathbf{a}_\beta$  and the first fundamental forms of the metric tensors are given by  $\mathbf{a}^\alpha \cdot \mathbf{a}^\beta = a^{\alpha\beta}$ ,  $\mathbf{a}^\alpha \cdot \mathbf{a}_\beta = \delta_\beta^\alpha$ . Defining  $\mathbf{a}_3 = (1/\sqrt{a})\mathbf{a}_1 \times \mathbf{a}_2$ , we have the relations  $\mathbf{a}_3 \cdot \mathbf{a}_\alpha = 0$ ,  $\mathbf{a}_3 \cdot \mathbf{a}^\alpha = 0$ . The permutation tensors  $e_{\alpha\beta}$  and  $e^{\alpha\beta}$  are defined by  $e_{\alpha\beta} : e_{12} = -e_{21} = \sqrt{a}$ ,  $e_{\alpha\beta} = -e_{\beta\alpha}$ ,  $e^{\alpha\beta} = -e^{\beta\alpha}$ ,  $e_{11} = e_{22} = 0$  and  $e^{\alpha\beta} : e^{12} = -e^{21} = 1/\sqrt{a}$ ,  $e^{11} = e^{22} = 0$ . The following expressions are then obtained for the vector products of the base vectors:  $\mathbf{a}_\alpha \times \mathbf{a}_\beta = e_{\alpha\beta} \mathbf{a}_3$ ,  $\mathbf{a}^\alpha \times \mathbf{a}^\beta = e^{\alpha\beta} \mathbf{a}_3$ ,  $\mathbf{a}_3 \times \mathbf{a}_\alpha = e_{\alpha\beta} \mathbf{a}^\beta$ ,  $\mathbf{a}_3 \times \mathbf{a}^\alpha = e^{\alpha\beta} \mathbf{a}_\beta$ . The coefficients of the second fundamental form are  $b_{\alpha\beta} = b_{\beta\alpha} = \mathbf{a}_{\alpha,\beta} \cdot \mathbf{a}_3 = -\mathbf{a}_{3,\alpha} \cdot \mathbf{a}_\beta$ . Then the derivatives of the base vectors are determined by  $\mathbf{a}_{\alpha,\beta} = \mathbf{a}_{\beta,\alpha} = \left\{ \begin{smallmatrix} \lambda \\ \alpha \beta \end{smallmatrix} \right\} \mathbf{a}_\lambda + b_{\alpha\beta} \mathbf{a}_3$ ,  $\mathbf{a}_{3,\alpha} = -b_{\alpha\beta} \mathbf{a}_\beta$ ,  $\mathbf{a}_{,\beta}^\alpha = \mathbf{a}_{\beta,\alpha} = -\left\{ \begin{smallmatrix} \alpha \\ \lambda \beta \end{smallmatrix} \right\} \mathbf{a}^\lambda + b_{\beta\alpha}^\alpha \mathbf{a}_3$ . The Christoffel symbols of the second kind for the surface are defined by the familiar relationships  $\left\{ \begin{smallmatrix} \lambda \\ \alpha \beta \end{smallmatrix} \right\} = \mathbf{a}_{\alpha,\beta} \cdot \mathbf{a}^\lambda = -\mathbf{a}_{,\beta}^\lambda \cdot \mathbf{a}_\alpha = -\mathbf{a}_{,\alpha}^\lambda \cdot \mathbf{a}_\beta$ , which can be expressed in the following manner in terms of the metric tensor  $\left\{ \begin{smallmatrix} \lambda \\ \alpha \beta \end{smallmatrix} \right\} = a^{\nu\lambda} (1/2)(a_{\beta\lambda,\alpha} + a_{\lambda\alpha,\beta} - a_{\alpha\beta,\lambda})$ .

The displacement vector  $\mathbf{v}(\theta^1, \theta^2)$  is resolved in the directions of the base vectors  $\mathbf{a}^\alpha$  and the normal vector  $\mathbf{a}_3$ , so that  $\mathbf{v} = v_\beta \mathbf{a}^\beta + v_3 \mathbf{a}_3$ . The strain measures of the middle surface of the shell is defined by  $\varepsilon_{\alpha\beta} = (1/2)(a_{\alpha\beta}^* - a_{\alpha\beta})_{\text{lin}} = (1/2)\delta a_{\alpha\beta}$ . As the difference  $a_{\alpha\beta}^* - a_{\alpha\beta}$  between the metric tensors in the deformed state and in the reference state is again a tensor, we obtain  $\varepsilon_{\alpha\beta} = (1/2)(\mathbf{a}_\alpha \cdot \mathbf{v}_{,\beta} + \mathbf{a}_\beta \cdot \mathbf{v}_{,\alpha})$ , which expresses the strain tensor in terms of the displacement components. The derivative of the displacement vector is written as  $\mathbf{v}_{,\alpha} = \varepsilon_{\alpha\beta} \mathbf{a}^\beta + \boldsymbol{\omega} \times \mathbf{a}_\alpha$ , where  $\boldsymbol{\omega} = \omega_\alpha \hat{\mathbf{a}}^\alpha + \omega_3 \mathbf{a}_3$ ,  $\omega_\alpha = -(v_{3,\alpha} + b_{\alpha\beta}^\beta v_\beta)$ ,  $\omega_3 = (1/2)e^{\alpha\beta} v_{\beta|\alpha}$ , giving the components of the rotation vector in terms of the displacements. The bending tensor  $\kappa_{\alpha\beta}$  can be expressed in terms of the displacement components through the following expression:

$$\kappa_{\alpha\beta} = - \left[ v_{3|\alpha\beta} + b_{\alpha|\beta}^\lambda v_{\lambda} + \frac{3}{4} (b_{\alpha}^\lambda v_{\lambda|\beta} + b_{\beta}^\lambda v_{\lambda|\alpha}) - \frac{1}{4} (b_{\alpha}^\lambda v_{\beta|\lambda} + b_{\beta}^\lambda v_{\alpha|\lambda}) \right], \quad (1)$$

which along with

$$e^{\alpha\beta} \left[ \kappa_{\alpha\lambda|\beta} + \frac{1}{2} (b_{\alpha}^{\lambda} \varepsilon_{\lambda\gamma} - b_{\gamma}^{\lambda} \varepsilon_{\lambda\alpha})_{|\beta} + b_{\alpha}^{\lambda} (\varepsilon_{\beta\lambda|\gamma} - \varepsilon_{\beta\gamma|\lambda}) \right] = 0, \\ e^{\alpha\lambda} e^{\beta\mu} (\kappa_{\alpha\beta} b_{\lambda\mu} - \varepsilon_{\alpha\beta|\lambda\mu}) = 0 \quad (2)$$

are the three equations of compatibility for shells.

The distributed surface load  $p$  is resolved in the directions of the base vectors  $\mathbf{a}_{\alpha}$  and the normal vector  $\mathbf{a}_3$ ; that is,  $\mathbf{p} = p^{\alpha} \mathbf{a}_{\alpha} + p^3 \mathbf{a}_3$ . If we write  $\mathbf{N}^{\alpha}$  and  $\mathbf{M}^{\alpha}$  in the form  $\mathbf{N}^{\alpha} = N^{\alpha\beta} \mathbf{a}_{\beta} + Q^{\alpha} \mathbf{a}_3$ ,  $\mathbf{M}^{\alpha} = M^{\alpha\beta} \hat{\mathbf{a}}_{\beta}$ , it can be seen that  $N^{\alpha\beta}$ ,  $Q^{\alpha}$ , and  $M^{\alpha\beta}$  are tensors, the types and orders of which are given by the positions and the numbers of indices. The quantities  $N^{\alpha\beta}$ ,  $Q^{\alpha}$ , and  $M^{\alpha\beta}$  are referred to as the complete contact forces and couples. Hence, the six scalar equations of equilibrium of the shell are as follows:  $N^{\alpha\beta}_{|\alpha} - b_{\alpha}^{\beta} Q^{\alpha} + p^{\beta} = 0$ ,  $Q^{\alpha}_{|\alpha} + N^{\alpha\beta} b_{\alpha\beta} + p^3 = 0$ ,  $M^{\alpha\beta}_{|\alpha} - Q^{\beta} = 0$ ,  $e_{\alpha\beta} (N^{\alpha\beta} - b_{\alpha}^{\lambda} M^{\lambda\beta}) = 0$ . For a thin shell consisting of a homogeneous and isotropic elastic material, the constitutive equations for the effective contact equations have the form

$$N^{\alpha\beta} = \frac{Eh}{1 - \nu^2} \left[ (1 - \nu) a^{\alpha\lambda} a^{\beta\mu} + \nu a^{\alpha\beta} a^{\lambda\mu} \right] \varepsilon_{\lambda\mu}, \\ M^{\alpha\beta} = \frac{Eh^3}{12(1 - \nu^2)} \left[ (1 - \nu) a^{\alpha\lambda} a^{\beta\mu} + \nu a^{\alpha\beta} a^{\lambda\mu} \right] \kappa_{\lambda\mu}. \quad (3)$$

The specific strain energy of the shell is given by

$$e = \frac{1}{2} \left[ N^{\alpha\beta} \varepsilon_{\alpha\beta} + M^{\alpha\beta} \kappa_{\alpha\beta} \right]. \quad (4)$$

### 3. Gradient Theory of Elasticity

The implicit version of gradient elasticity, which combines both Eringen's stress-gradient and Aifantis' stable strain-gradient theory, can be summarized by the following gradient constitutive equation  $(1 - l_d^2 \nabla^2) \sigma_{ij} = C_{ijkl} (1 - l_s^2 \nabla^2) \varepsilon_{kl}$ . The stress gradient internal length may be set, under certain circumstances, equal to the internal length scale for dynamics ( $l_{\sigma} \approx l_d$ ). The strain gradient internal length is identified with the internal length scale for statics ( $l_{\varepsilon} \approx l_s$ ). The symbol  $\sigma_{ij}$  denotes the stress tensor and the symbol  $\varepsilon_{kl}$  denotes the strain tensor, while  $C_{ijkl}$  is the linear elastic stiffness tensor. It is worth noting that the length scales for statics and dynamics are not equal in general. When the static length scale is zero, the theory is a special form of Aifantis' strain-gradient elasticity, and when the dynamics length scale is zero, the theory reduces to Eringen's stress-gradient elasticity theory. When both internal length scale parameters tend to zero, the theory becomes Hooke's law of classical elasticity. Identification and quantification of the internal lengths have been discussed in Askes and Aifantis [15], which is beyond the focus of this paper.

Due to the fact that  $|l_d^2 l_s^2 \nabla^2| \sim 1$ , the gradient elasticity constitutive relations can be approximated up to 2nd order terms as follows:  $(1 + l_s^2 \nabla^2 - l_d^2 \nabla^2) \sigma_{ij} = C_{ijkl} \varepsilon_{kl}$ , or the

alternative form  $\sigma_{ij} = C_{ijkl} (1 + l_d^2 \nabla^2 - l_s^2 \nabla^2) \varepsilon_{kl}$ . These relations will be used in the sequel to derive robust approximate but quite general results appropriate for all formulations.

### 4. Formulation of Linear Gradient Shell

**Theory Based on**  $(1 - l_d^2 \nabla^2) \sigma_{ij} = C_{ijkl} (1 - l_s^2 \nabla^2) \varepsilon_{kl}$

Once we adopt the constitutive equation of implicit gradient elasticity  $(1 - l_d^2 \nabla^2) \sigma_{ij} = C_{ijkl} (1 - l_s^2 \nabla^2) \varepsilon_{kl}$ , then the corresponding theory for gradient shells can be easily formulated. For orthogonal coordinates, we have the two-dimensional Laplace operator

$$\nabla^2 (\dots) = \frac{1}{A_1 A_2} \left\{ \frac{\partial}{\partial \alpha_1} \left[ \frac{A_2}{A_1} \frac{\partial (\dots)}{\partial \alpha_1} \right] + \frac{\partial}{\partial \alpha_2} \left[ \frac{A_1}{A_2} \frac{\partial (\dots)}{\partial \alpha_2} \right] \right\}, \quad (5)$$

where  $A_i$  denote Lámé parameters of the mid-surface of the shell.

For a thin shell consisting of a homogeneous, isotropic elastic material, the constitutive equations for the effective contact equations have the constitutive equation (3).

Then, their gradient counterparts read as follows:

$$(1 - l_d^2 \nabla^2) N^{\alpha\beta} \\ = \frac{Eh}{1 - \nu^2} \left[ (1 - \nu) a^{\alpha\lambda} a^{\beta\mu} + \nu a^{\alpha\beta} a^{\lambda\mu} \right] (1 - l_s^2 \nabla^2) \varepsilon_{\lambda\mu}, \\ (1 - l_d^2 \nabla^2) M^{\alpha\beta} \\ = \frac{Eh^3}{12(1 - \nu^2)} \left[ (1 - \nu) a^{\alpha\lambda} a^{\beta\mu} + \nu a^{\alpha\beta} a^{\lambda\mu} \right] (1 - l_s^2 \nabla^2) \kappa_{\lambda\mu}. \quad (6)$$

The corresponding balance equations read

$$(1 - l_s^2 \nabla^2) \left[ N^{\alpha\beta}_{|\alpha} - b_{\alpha}^{\beta} Q^{\alpha} \right] + (1 - l_d^2 \nabla^2) p^{\beta} = 0, \\ (1 - l_s^2 \nabla^2) \left[ Q^{\alpha}_{|\alpha} + N^{\alpha\beta} b_{\alpha\beta} \right] + (1 - l_d^2 \nabla^2) p^3 = 0, \quad (7) \\ M^{\alpha\beta}_{|\alpha} - Q^{\beta} = 0.$$

The specific strain energy of the shell is given by  $W = [1 + (l_d^2 - l_s^2) \nabla^2] e$ , where  $e$  denotes the classical strain energy density of the shell; that is,

$$e = \frac{1}{2} \frac{Eh}{1 - \nu^2} \left[ (1 - \nu) \varepsilon^{\alpha\beta} \varepsilon_{\alpha\beta} + \nu \varepsilon_{\alpha}^{\alpha} \varepsilon_{\beta}^{\beta} \right] \\ + \frac{Eh^3}{24(1 - \nu^2)} \left[ (1 - \nu) \kappa^{\alpha\beta} \kappa_{\alpha\beta} + \nu \kappa_{\alpha}^{\alpha} \kappa_{\beta}^{\beta} \right]. \quad (8)$$

## 5. Formulation of Linear Gradient Shell

### Theory Based on $\sigma_{ij} \cong C_{ijkl}(1 + l_d^2 \nabla^2 - l_s^2 \nabla^2) \varepsilon_{kl}$

The appropriate gradient constitutive equations for this shell theory take the form

$$\begin{aligned} N^{\alpha\beta} &= \frac{Eh}{1-\nu^2} \left[ (1-\nu) a^{\alpha\lambda} a^{\beta\mu} + \nu a^{\alpha\beta} a^{\lambda\mu} \right] \\ &\quad \times \left( 1 + l_d^2 \nabla^2 - l_s^2 \nabla^2 \right) \varepsilon_{\lambda\mu}, \\ M^{\alpha\beta} &= \frac{Eh^3}{12(1-\nu^2)} \left[ (1-\nu) a^{\alpha\lambda} a^{\beta\mu} + \nu a^{\alpha\beta} a^{\lambda\mu} \right] \\ &\quad \times \left( 1 + l_d^2 \nabla^2 - l_s^2 \nabla^2 \right) \kappa_{\lambda\mu}, \end{aligned} \quad (9)$$

and the balance equations read

$$\begin{aligned} \left( 1 + l_d^2 \nabla^2 - l_s^2 \nabla^2 \right) \left[ N^{\alpha\beta}{}_{|\alpha} - b_{\alpha}^{\beta} Q^{\alpha} \right] + p^{\beta} &= 0, \\ \left( 1 + l_d^2 \nabla^2 - l_s^2 \nabla^2 \right) \left[ Q^{\alpha}{}_{|\alpha} + N^{\alpha\beta} b_{\alpha\beta} \right] + p^3 &= 0, \\ Q^{\beta} &= M^{\alpha\beta}{}_{|\alpha}. \end{aligned} \quad (10)$$

## 6. Formulation of Linear Gradient Shell

### Theory Based on $(1 + l_s^2 \nabla^2 - l_d^2 \nabla^2) \sigma_{ij} \cong C_{ijkl} \varepsilon_{kl}$

The appropriate gradient constitutive equations for this shell theory take the form

$$\begin{aligned} \left( 1 - l_d^2 \nabla^2 + l_s^2 \nabla^2 \right) N^{\alpha\beta} &= \frac{Eh}{1-\nu^2} \left[ (1-\nu) a^{\alpha\lambda} a^{\beta\mu} + \nu a^{\alpha\beta} a^{\lambda\mu} \right] \varepsilon_{\lambda\mu}, \\ \left( 1 - l_d^2 \nabla^2 + l_s^2 \nabla^2 \right) M^{\alpha\beta} &= \frac{Eh^3}{12(1-\nu^2)} \left[ (1-\nu) a^{\alpha\lambda} a^{\beta\mu} + \nu a^{\alpha\beta} a^{\lambda\mu} \right] \kappa_{\lambda\mu}, \end{aligned} \quad (11)$$

and the balance equations read

$$\begin{aligned} \left[ N^{\alpha\beta}{}_{|\alpha} - b_{\alpha}^{\beta} Q^{\alpha} \right] + \left( 1 - l_d^2 \nabla^2 + l_s^2 \nabla^2 \right) p^{\beta} &= 0, \\ \left[ Q^{\alpha}{}_{|\alpha} + N^{\alpha\beta} b_{\alpha\beta} \right] + \left( 1 - l_d^2 \nabla^2 + l_s^2 \nabla^2 \right) p^3 &= 0, \\ Q^{\beta} &= M^{\alpha\beta}{}_{|\alpha}. \end{aligned} \quad (12)$$

## 7. Conclusions

Various gradient (nano)shell models can be easily formulated by simply replacing the classical constitutive equations of classical elasticity with the constitutive equation of the implicit gradient elasticity  $(1 - l_d^2 \nabla^2) \sigma_{ij} = C_{ijkl} (1 - l_s^2 \nabla^2) \varepsilon_{kl}$  and its approximate versions of strain gradient  $\sigma_{ij} = C_{ijkl} (1 + l_d^2 \nabla^2 - l_s^2 \nabla^2) \varepsilon_{kl}$  and stress gradient  $(1 + l_s^2 \nabla^2 - l_d^2 \nabla^2) \sigma_{ij} = C_{ijkl} \varepsilon_{kl}$  counterparts. All formulations can also be extended in an analogous manner, to geometrically nonlinear theory of gradient shells [16].

## Conflict of Interests

The authors declare that there is no conflict of interests regarding the publication of this paper.

## Acknowledgment

E. C. Aifantis acknowledges support of GSRT under grants Thales Intermonu and ERC-13, as well as a HiCi grant from KAU.

## References

- [1] A. Cauchy, "Memoire sur les systemes isotropes de points materiels," in *Oeuvres completes—Tome II*, 1st Serie, pp. 351–386, Gauthier-Villars, Paris, France, 1850, reprint 1908.
- [2] A. Cauchy, "Memoire sur les vibrations d'un double systeme de molecules et de l'ether continu dans un corps cristallise," in *Oeuvres completes—Tome II*, 1st Serie, pp. 338–350, Gauthier-Villars, Paris, France, 1850, reprint 1908.
- [3] E. Cosserat and F. Cosserat, *Theorie des Corps Deformables*, Hermann et Fils, Paris, France, 1909.
- [4] R. D. Mindlin, "Micro-structure in linear elasticity," *Archive for Rational Mechanics and Analysis*, vol. 16, no. 1, pp. 51–78, 1964.
- [5] R. D. Mindlin, "Second gradient of strain and surface-tension in linear elasticity," *International Journal of Solids and Structures*, vol. 1, no. 4, pp. 417–438, 1965.
- [6] A. C. Eringen, "Nonlocal continuum theory for dislocations and fracture," in *The Mechanics of Dislocations*, E. C. Aifantis and J. P. Hirth, Eds., pp. 101–110, ASM, Metals Park, Ohio, USA, 1985.
- [7] A. C. Eringen, "Vistas of nonlocal continuum physics," *International Journal of Engineering Science*, vol. 30, no. 10, pp. 1551–1565, 1992.
- [8] A. C. Eringen, "On differential equations of nonlocal elasticity and solutions of screw dislocation and surface waves," *Journal of Applied Physics*, vol. 54, no. 9, pp. 4703–4710, 1983.
- [9] A. C. Eringen, *Nonlocal Continuum Field Theories*, Springer, 2012.
- [10] E. C. Aifantis, "On the role of gradients in the localization of deformation and fracture," *International Journal of Engineering Science*, vol. 30, no. 10, pp. 1279–1299, 1992.
- [11] E. C. Aifantis, "On the gradient approach: relation to Eringen's nonlocal theory," *International Journal of Engineering Science*, vol. 49, no. 12, pp. 1367–1377, 2011.
- [12] E. C. Aifantis, "Update on a class of gradient theories," *Mechanics of Materials*, vol. 35, pp. 259–280, 2009.
- [13] H. Mollmann, *Introduction to the Theory of Thin Shells*, John Wiley & Sons, New York, NY, USA, 1981.
- [14] A. E. H. Love, *A Treatise on the Mathematical Theory of Elasticity*, Cambridge University Press, Cambridge, UK, 4th edition, 1927.
- [15] H. Askes and E. C. Aifantis, "Gradient elasticity in statics and dynamics: an overview of formulations, length scale identification procedures, finite element implementations and new results," *International Journal of Solids and Structures*, vol. 48, no. 13, pp. 1962–1990, 2011.
- [16] B. Sun, "Gradient theory of nanoplates and nanoshells," in *Proceedings of the 12th Annual SPE Automotive Composites Conference and Exhibition (ACCE '12)*, Beijing, China, 2012.

## Research Article

# Nonlocal Elasticity Theory for Transient Analysis of Higher-Order Shear Deformable Nanoscale Plates

Woo-Young Jung<sup>1</sup> and Sung-Cheon Han<sup>2</sup>

<sup>1</sup> Department of Civil Engineering, Gangneung-Wonju National University, 7 Jukheon, Gangneung 210-702, Republic of Korea

<sup>2</sup> Department of Civil & Railroad Engineering, Daewon University College, 599 Shinwol, Jecheon 390-702, Republic of Korea

Correspondence should be addressed to Sung-Cheon Han; [hasc1203@daum.net](mailto:hasc1203@daum.net)

Received 9 October 2013; Revised 15 December 2013; Accepted 28 December 2013; Published 12 February 2014

Academic Editor: Munawar A. Riyadi

Copyright © 2014 W.-Y. Jung and S.-C. Han. This is an open access article distributed under the Creative Commons Attribution License, which permits unrestricted use, distribution, and reproduction in any medium, provided the original work is properly cited.

The small scale effect on the transient analysis of nanoscale plates is studied. The elastic theory of the nano-scale plate is reformulated using Eringen's nonlocal differential constitutive relations and higher-order shear deformation theory (HSDT). The equations of motion of the nonlocal theories are derived for the nano-scale plates. The Eringen's nonlocal elasticity of Eringen has ability to capture the small scale effects and the higher-order shear deformation theory has ability to capture the quadratic variation of shear strain and consequently shear stress through the plate thickness. The solutions of transient dynamic analysis of nano-scale plate are presented using these theories to illustrate the effect of nonlocal theory on dynamic response of the nano-scale plates. On the basis of those numerical results, the relations between nonlocal and local theory are investigated and discussed, as are the nonlocal parameter, aspect ratio, side-to-thickness ratio, nano-scale plate size, and time step effects on the dynamic response. In order to validate the present solutions, the reference solutions are employed and examined. The results of nano-scale plates using the nonlocal theory can be used as a benchmark test for the transient analysis.

## 1. Introduction

Due to their superior properties, nanoscale plates such as graphene [1], the two-dimensional (2D) counterpart of three-dimensional (3D) graphite, have attracted attention within the fields of solid-state physics, materials science, and nano-electronics. Experimentation with nano-scale size specimens is both difficult and expensive. Development of appropriate mathematical models for nanostructures, therefore, is essential. Approaches to the modeling of nanostructures are classified into three main categories: atomistic [2, 3], continuum [4–6], and hybrid atomistic-continuum mechanics [7–9]. The continuum mechanics approach is less computationally expensive and, furthermore, generates results that tend to be in good agreement with those of the atomistic and hybrid approaches [10, 11].

As small size analysis using local theory over-predicts results, correct prediction of micro-/nanostructures requires consideration of small-scale effect. Peddieson et al. [12]

applied nonlocal elasticity to the formulation of a nonlocal version of the Euler-Bernoulli beam model and concluded that nonlocal continuum mechanics could potentially play a useful role in nanotechnology applications. One of the well-known continuum mechanics theories that include small scale effects with good accuracy is Eringen's nonlocal theory [13, 14]. This, compared with classical continuum mechanics theory, can predict the behavior of the large nanosized structures, without a large number of equations.

Nonlocal elasticity theory has been widely applied to the bending, vibration, and buckling behavior of one-dimensional (1D) nanostructures including nanobeams, nanorods, and carbon nanotubes. Contrastingly, there has been no such work related to the transient analysis of nano-scale plate based on higher-order shear deformation theory (HSDT). However, some researchers have applied nonlocal elasticity theory to the study of various applications of micro- and nanostructures [15, 16]. Understanding the importance of employing nonlocal elasticity theory to small scale structures,

a number of researchers have reported on static, dynamic and stability analysis of 1D and 2D micro-/nanostructures [17–25]. Kiani [26] studied the free vibration of embedded single-walled nanotubes accounting for nonlocal effect using a meshless method. Nonlocal continuum-based modeling of a nanoplate subjected to a moving nanoparticle was presented by Kiani [27, 28]. Jomehzadeh and Saidi [29] investigated the decoupling of the nonlocal elasticity equations for three dimensional vibration analysis of nanoplates.

These studies [17–25] were based on classical and first-order theories of plates. The analysis of 2D nano-scale plates with accurate stress fields requires further study. The third-order shear deformation theory (TSDT) of Reddy [30] is based on a displacement field that includes the cubic term in the thickness coordinate; hence, the transverse shear strain and stress are represented as quadratic through the plate thickness and vanish on the bounding planes of the plate. Some studies, in fact, have incorporated the TSDT to obtain more accurate results [31–33]. It seems appropriate and potentially fruitful, therefore, to explore TSDT's extension to include size effects. The present study, accordingly, applies the nonlocal TSDT to the transient dynamic response of nano-scale plates.

To avoid the resonant behavior of such structures, a vibration analysis of their design is very important. Also, most of these structures, whether they are used in the civil, marine or aerospace field, are subjected to dynamic loads; therefore, there is a need to assess their transient response. However, transient analysis of nano-scale plates has not received adequate consideration. Work that exists on the vibration analysis of laminated composite and FGM plates can be found in [34, 35].

In the present work, nonlocal elasticity theory is applied to a transient analysis of nano-scale plates. Navier's method is used to solve the governing equations for simply supported boundary conditions. The effects of (i) the nonlocal parameter, (ii) size of the nano-scale plates, (iii) aspect ratios, and (iv) side-to-thickness ratios on the nondimensional dynamic responses are investigated. The present work will be helpful to the design of nano-electro-mechanical system or micro-electro-mechanical systems devices incorporating nano-scale plates.

## 2. Formulation

In classical local elasticity theory, stress at a point depends only on the strain at that point, whereas, in nonlocal elasticity theory, the stress at a point is a function of the strains at all points on the continuum. In other words, in nonlocal elasticity theory, stress at a point is determined by both stress at that point and spatial derivatives of it. According to Eringen [13, 14], the nonlocal constitutive behavior of a Hookean solid is represented by the differential constitutive relation

$$(1 - \mu \nabla^2) \sigma_{ij} = t_{ij}, \quad (1)$$

where  $t_{ij}$  is the local stress tensor,  $\sigma_{ij}$  is the nonlocal stress tensor, and the nonlocal parameter  $\mu$  is defined by

$$\mu = e_0^2 \bar{a}^2 \quad (2)$$

in which  $e_0$  is the material constant set by the experiment and  $\bar{a}$  is the internal characteristic length.

The relations between stress resultants in local theory and in nonlocal theory are defined by integrating plate thickness into (1) as

$$\begin{aligned} \mathcal{L}(M_{ij}^{(0)}) &= M_{ij}^{(0)L}, \\ \mathcal{L}(M_{ij}^{(1)}) &= M_{ij}^{(1)L}, \\ \mathcal{L}(M_{ij}^{(2)}) &= M_{ij}^{(2)L}, \end{aligned} \quad (3)$$

where  $\mathcal{L} = 1 - \mu \nabla^2$  and

$$\begin{aligned} \begin{Bmatrix} M_{\alpha\beta}^{(0)}, M_{\alpha\beta}^{(0)L} \\ M_{\alpha\beta}^{(1)}, M_{\alpha\beta}^{(1)L} \\ M_{\alpha\beta}^{(2)}, M_{\alpha\beta}^{(2)L} \end{Bmatrix} &= \int_{-h/2}^{h/2} \{\sigma_{\alpha\beta}, t_{\alpha\beta}\} \begin{Bmatrix} 1 \\ z \\ z^2 \end{Bmatrix} dz, \\ \begin{Bmatrix} M_{\alpha z}^{(0)}, M_{\alpha z}^{(0)L} \\ M_{\alpha z}^{(2)}, M_{\alpha z}^{(2)L} \end{Bmatrix} &= \int_{-h/2}^{h/2} \{\sigma_{\alpha z}, t_{\alpha z}\} \begin{Bmatrix} 1 \\ z^2 \end{Bmatrix} dz, \end{aligned} \quad (4)$$

where  $\alpha$  and  $\beta$  take the symbols  $x, y$ , the superscript  $L$  denotes the quantities in local third-order shear deformation theory, and  $h$  is the thickness of the plate.

In general, differential operator  $\nabla$  in (1) is the 3D Laplace operator. For 2D problems, the operator  $\nabla$  may be reduced to the 2D one. Thus, the linear differential operator  $\mathcal{L}$  becomes

$$\bar{\mathcal{L}} = 1 - \mu \left( \frac{\partial^2}{\partial x^2} + \frac{\partial^2}{\partial y^2} \right), \quad (5)$$

wherein it is clear that operator  $\bar{\mathcal{L}}$  is independent of the  $z$  direction.

The third-order shear deformation theory (TSDT) extends the first-order theory by assuming that shear strain and consequently shear stress are not constant through the plate thickness [30]. The displacement field of the third-order theory of plates is given by

$$\begin{aligned} u_\alpha &= u_\alpha^0 + z\phi_\alpha - c_1 z^3 (\phi_\alpha + w_{,\alpha}^0), \\ u_z &= w^0, \end{aligned} \quad (6)$$

where  $u_\alpha^0$  and  $w^0$  are the in plane displacements and transverse displacement of point on the midplane (i.e.,  $z = 0$ ), respectively,  $c_1 = 4/3h^2$ ,  $u_z$  is the transverse displacement of the mid-plane of the plate, and  $\phi_\alpha$  denotes the slope of the transverse normal on the mid-plane.

The variational statements facilitate the direct derivation of the equations of motion in terms of the displacements. The governing equations of the third-order nonlocal plate theory

can be derived, using the dynamic version of the principle of virtual displacement (Hamilton's principle), as

$$0 = \int_0^T (\delta U + \delta V - \delta K) dt, \quad (7)$$

where  $\delta U$  is the virtual strain energy,  $\delta V$  is the virtual work done by external forces, and  $\delta K$  is the virtual kinetic energy.

It can be seen from (1) that nonlocal behavior enters into the problem through the constitutive relations. The principal of virtual work, because it is independent of such relations, can be applied to derive the equilibrium equations of nonlocal nano-scale plates. On the basis of the principle of virtual displacements, then the governing equations are obtained [32]

$$\begin{aligned} \delta u_x^0: M_{xx,x}^{(0)} + M_{xy,y}^{(0)} - \overline{\mathcal{L}} (I_0 \ddot{u}_x^0) &= 0, \\ \delta u_y^0: M_{xy,x}^{(0)} + M_{yy,y}^{(0)} - \overline{\mathcal{L}} (I_0 \ddot{u}_y^0) &= 0, \\ \delta w^0: M_{zx,x}^{(0)} + M_{zy,y}^{(0)} - c_2 (M_{zx,x}^{(2)} + M_{zy,y}^{(2)}) \\ &+ c_1 (M_{xx,xx}^{(2)} + M_{yy,yy}^{(2)} + 2M_{xy,xy}^{(2)}) \\ &- \overline{\mathcal{L}} [-q_z + I_0 \ddot{w}^0 + c_1 I_4 (\ddot{\phi}_{x,x} + \ddot{\phi}_{y,y}) \\ &- c_1^2 I_6 (\ddot{\phi}_{x,x} + \ddot{\phi}_{y,y} + \ddot{w}_{,xx}^0 + \ddot{w}_{,yy}^0)] = 0, \\ \delta \phi_x: M_{xx,x}^{(1)} + M_{xy,y}^{(1)} - c_1 (M_{xx,x}^{(2)} + M_{xy,y}^{(2)}) - M_{zx}^{(0)} + c_2 M_{zx}^{(2)} \\ &- \overline{\mathcal{L}} [I_2 \ddot{\phi}_x - c_1 I_4 (\ddot{\phi}_x + \ddot{w}_{,x}^0) \\ &- c_1 (I_4 \ddot{\phi}_x - c_1 I_6 (\ddot{\phi}_x + \ddot{w}_{,x}^0))] = 0, \\ \delta \phi_y: M_{xy,x}^{(1)} + M_{yy,y}^{(1)} - c_1 (M_{xy,x}^{(2)} + M_{yy,y}^{(2)}) - M_{zy}^{(0)} + c_2 M_{zy}^{(2)} \\ &- \overline{\mathcal{L}} [I_2 \ddot{\phi}_y - c_1 I_4 (\ddot{\phi}_y + \ddot{w}_{,y}^0) \\ &- c_1 (I_4 \ddot{\phi}_y - c_1 I_6 (\ddot{\phi}_y + \ddot{w}_{,y}^0))] = 0, \end{aligned} \quad (8)$$

where  $I_k = \int_{-h/2}^{h/2} \rho(z)^k dz$  ( $k = 0, 2, 4, 6$ ) and  $c_2 = 3c_1$ , in which  $\rho$  is the mass density. From these, by setting  $\overline{\mathcal{L}} = 1$ , the equations of motion of the conventional third-order plate theory are obtained.

### 3. Navier Solutions of Nonlocal Third-Order Shear Deformation Theory

Here, analytical solutions to the free and forced vibration of simply supported plates are presented using the nonlocal third-order plate theory in order to illustrate the small scale effects on deflections and natural frequencies of the plates. For the set of simply supported boundary conditions, the Navier solution can be obtained [32]. According to Navier

solution theory, the generalized displacements at middle of the plane ( $z = 0$ ) are expanded in double Fourier series as

$$\begin{aligned} \{u_x^0(x, y, t), \phi_x(x, y, t)\} &= \sum_{m=1}^{\infty} \sum_{n=1}^{\infty} \{U_{mn}, X_{mn}\} \Lambda_1, \\ \{u_y^0(x, y, t), \phi_y(x, y, t)\} &= \sum_{m=1}^{\infty} \sum_{n=1}^{\infty} \{V_{mn}, Y_{mn}\} \Lambda_2, \quad (9) \\ \{w^0(x, y, t), q_z(x, y, t)\} &= \sum_{m=1}^{\infty} \sum_{n=1}^{\infty} \{W_{mn}, Q_{mn}\} \Lambda_3, \end{aligned}$$

where  $\Lambda_1 = \cos \xi x \sin \eta y \cdot e^{i\omega_{mn}t}$ ,  $\Lambda_2 = \sin \xi x \cos \eta y \cdot e^{i\omega_{mn}t}$ , and  $\Lambda_3 = \sin \xi x \sin \eta y \cdot e^{i\omega_{mn}t}$ , in which,  $\xi = m\pi/a$ ,  $\eta = n\pi/b$ ,  $i = \sqrt{-1}$ ,  $t$  is the time and  $\omega_{mn}$  is the natural frequency.

Substituting (9) into (8), the matrix form obtained is

$$[\mathbf{K}] \{\Delta\} + [\mathbf{M}] \{\dot{\Delta}\} = \{Q\}, \quad (10)$$

where  $\{\Delta\} = \{U_{mn}, V_{mn}, W_{mn}, X_{mn}, Y_{mn}\}$ ,  $[\mathbf{K}]$  is the stiffness matrix,  $[\mathbf{M}]$  is the mass matrix, dot-superscript convention indicates the differentiation with respect to the time variable  $t$ , and  $\{Q\}$  is the force vector. For this study, the Newmark- $\beta$  time integration method is used.

In order to investigate the transient response of a laminated composite and nano-scale plate, a parametric study is carried out according to different dynamic loading conditions. The load acting on the plate is distributed over its entire surface and varied with time according to

$$q(x, y, t) = q_z F(t), \quad (11)$$

where  $q_z = \sum_{m=1}^{\infty} \sum_{n=1}^{\infty} Q_{mn} \sin \alpha x \sin \beta y$ , the  $Q_{mn}$  is the coefficient for some typical load [32],  $F(t) = \{1, 0 \leq t\}$ : rectangular step loading, and

$$F(t) = \begin{cases} 1, & 0 \leq t \leq t_1 \\ 0, & t \geq t_1 \end{cases} : \text{rectangular pulse loading}, \quad (12)$$

in which  $t_1 = 1000 \mu\text{s}$ .

## 4. Numerical Results and Discussion

To validate this present study, several numerical examples are solved to test the performance in free and forced vibration analyses. Examples include composite materials for confirmation of crucial features or for comparison with previous published analysis results. Specially, a mistake in a reference is corrected for the purpose of an accurate comparison.

**4.1. Validation.** In order to validate the results of the forced vibration analysis, a transient analysis of the simply supported cross-ply ( $0^\circ/90^\circ$ ) plate shown in Figure 1 is carried out under sinusoidal step loading intensity  $q_0 = 10$  with  $\Delta t = 5 \mu\text{s}$ . The rectangular plate, shown in Figure 1, is analyzed for the natural vibration of laminated composite plate, and results are presented in Figure 2.

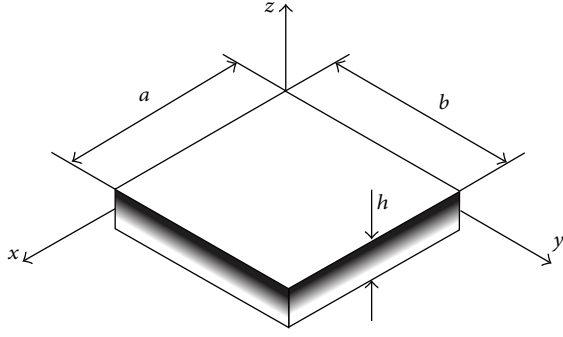


FIGURE 1: Geometry of laminated composite and nanoscale plates.

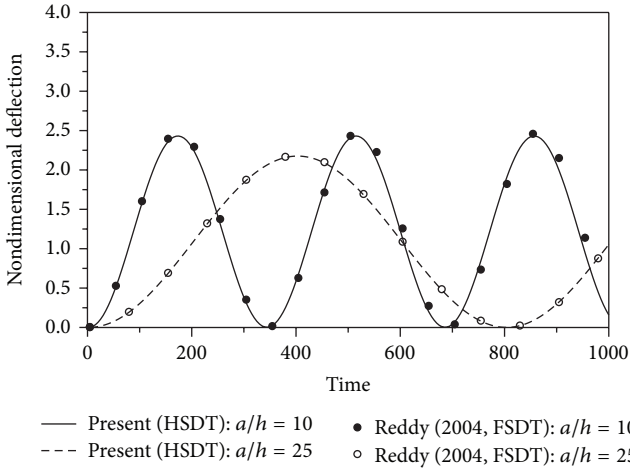


FIGURE 2: Dynamic response of laminated composite plate under suddenly applied step load.

The geometric and material properties applied are as follows:

$$\begin{aligned}
 a = b = 25 \text{ cm}, \quad \Delta t = 5 \mu\text{s}, \quad \rho = 8 \times 10^{-8} \text{ N} \cdot \text{s}^2/\text{cm}^4, \\
 E_1 = 25E_2, \quad E_2 = 2.1 \times 10^6 \text{ N/cm}^2, \\
 G_{12} = G_{13} = 0.5E_2, \quad G_{23} = 0.2E_2, \\
 \nu_{12} = \nu_{13} = \nu_{23} = 0.25, \quad q_0 = 10 \text{ N/cm}^2.
 \end{aligned} \tag{13}$$

The center deflection versus time of a cross-ply plate ( $0^\circ/90^\circ$ ) is compared with the results by Reddy [32]. Figure 2 shows the present results and the results by Reddy [32]. It can be seen that the difference between the two results is almost negligible.

The results are presented in the nondimensional form using the equation:

$$\bar{w} = w \times \frac{E_2 h^3}{q_0 b^4} \times 10^2. \tag{14}$$

**4.2. Free Vibration of Nanoscale Plate.** The analytical free vibration responses are numerically evaluated here for an

TABLE 1: Nondimensional frequency of simply supported nanoscale plate with various nonlocal parameter ( $\mu$ ).

$\mu$	$a/h = 10, b/a = 1$		$a/h = 10, b/a = 2$	
	Aghababaei and Reddy [36]	Present	Aghababaei and Reddy [36]	Present
0	0.0930	0.0930	0.0589	0.0589
1	0.0850	0.0850	0.0556	0.0556
2	0.0788	0.0788	0.0527	0.0527
3	0.0737	0.0737	0.0503	0.0503
4	0.0696	0.0695	0.0482	0.0482
5	0.0660	0.0660	0.0463	0.0463

TABLE 2: Nondimensional material and geometric properties.

$E$	$\nu$	$a = b$	$\rho$	$q_z$
$30 \times 10^6$	0.3	10	$5 \times 10^{-6}$	1.0

isotropic plate to discuss the effects of nonlocal parameter  $\mu$  on the plate vibration response. Table 1 shows the nondimensional frequencies of simply supported nano-scale plates with various values of nonlocal parameter  $\mu$ . The nanoscale plate is made of the following material properties:

$$E = 2.6, \quad \nu = 0.3, \quad \rho = 1.0. \tag{15}$$

The results are presented in the non-dimensional form using the equation:

$$\bar{\omega}_{11} = \omega_{11} \times h \sqrt{\frac{\rho}{G}}. \tag{16}$$

The results based on HSDT plate theory with various values of nonlocal parameter  $\mu$  are compared with those reported by Aghababaei and Reddy [36]. It can be seen that when the aspect ratios are 1 and 2, the two sets of results are identical. Table 1 also shows that the material property ( $E = 30 \times 10^6$ ) presented by Aghababaei and Reddy [36] is not accurate, and that, for accurate comparison by (15), it should be modified.

**4.3. Forced Vibration of Nanoscale Plate under Step Load.** The non-dimensional geometric and material data on the nanoscale plate are provided in Table 2.

The results of a forced vibration analysis of laminated composite plate under a distributed rectangular step load with  $\Delta t = 5 \mu\text{s}$  and a variable nonlocal parameter are plotted in Figure 3. The nonlocal parameters are  $\mu = 0, 0.25, 1.0, 2.25, \text{ and } 4$ , because  $e_0 \bar{a}$  in (2) should be smaller than 2.0 nm for carbon nanotubes (Q. Wang and C. M. Wang [37]). The results show the profound scale effect for the higher values of nonlocal parameter. In other words, the local elasticity theory under-predicts the dynamic response. Thus also, if local elasticity results are used for experimental determination of Young's modulus, the value will be under-predicted.

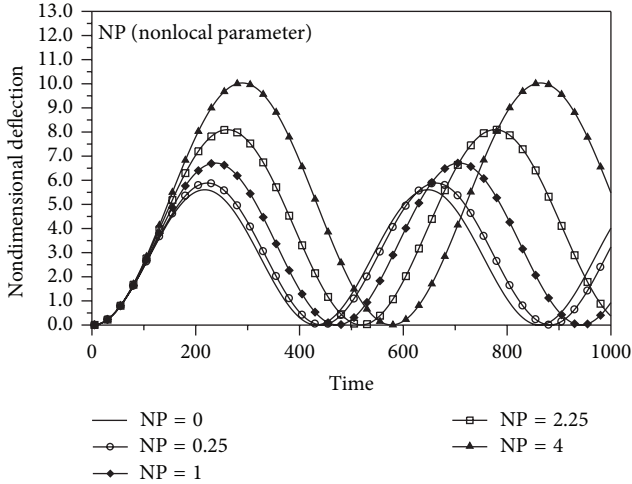


FIGURE 3: Dynamic response of nano-scale plate under suddenly applied step load with variable nonlocal parameter.

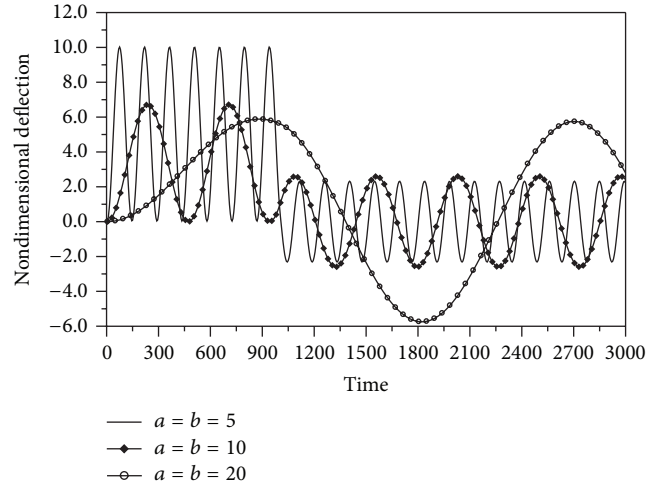


FIGURE 5: Dynamic response of nano-scale plate under suddenly applied pulse load of variable size ( $\mu = 1, t_1 = 1000 \mu s$ ).

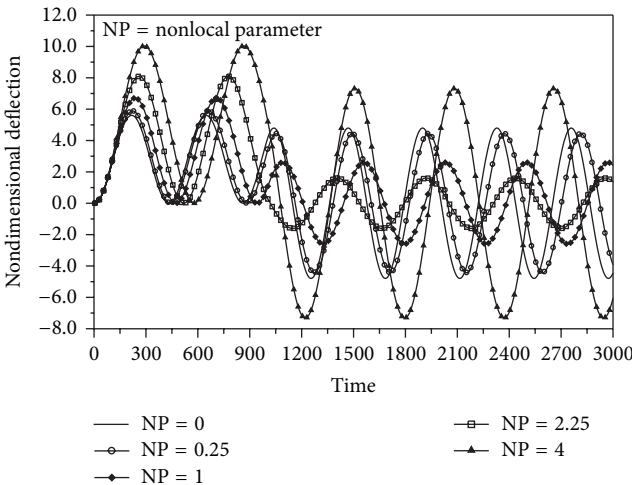


FIGURE 4: Dynamic response of nano-scale plate under suddenly applied pulse load ( $t_1 = 1000 \mu s$ ).

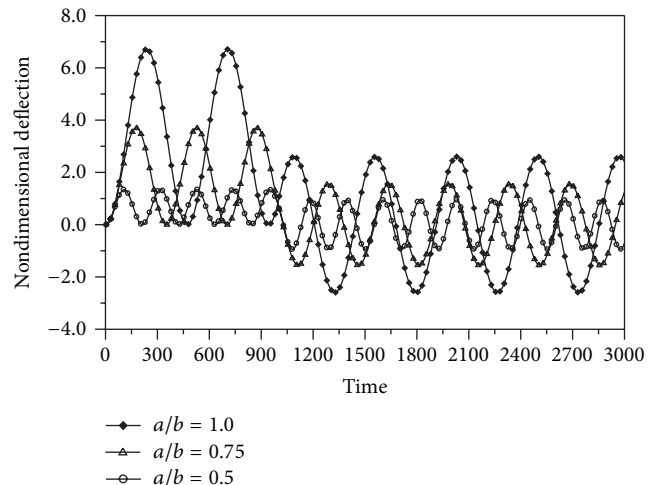


FIGURE 6: Dynamic response of nano-scale plate of variable aspect ratio under suddenly applied pulse load ( $\mu = 1, t_1 = 1000 \mu s$ ).

4.4. Forced Vibration of Nanoscale Plate under Pulse Load.

A forced vibration analysis of center deflection under the rectangular pulse loading is carried out using the same material. The plot of the center deflection versus time is shown in Figure 4. As can be seen, the maximum deflection increases until the applied loading is removed after  $t_1 = 1000 \mu s$ , due to the nonlocal parameters increase due to stiffness degradation. After removal of the load, however, a change of the maximum deflection occurs. This phenomenon is expected to vary with the point at which the load is removed. Accordingly, the amplitude also changes after the load removal.

Figure 5 shows the variation of dynamic response with respect to the length of the nano-scale plate, which varies from 5 nm to 20 nm. The nonlocal variable is assumed to be 1. As the size of the nano-scale plate increases, the amplitude and frequency of the dynamic response decrease.

The dynamic response due to the change of the aspect ratio ( $a/b = 0.5, 0.75, 1.0$ ) of the nano-scale plate is shown in Figure 6. The nonlocal variable is again assumed to be 1. The amplitude and the period of the dynamic response decrease, as the aspect ratio decreases. When the aspect ratio changes from 1 to 0.75, the maximum deflection is reduced by 45%: when the aspect ratio changes from 0.75 to 0.5, the reduction is 64%.

Figure 7 shows the dynamic response of a nano-scale plate of variable side-to-thickness ratio under a suddenly applied pulse load. Typically in the case of isotropic plates or laminated composite plates, the side-to-thickness ratio is more than 20, and the effect of shear deformation is very small. Similarly, in the case of the nano-scale plate shown in Figure 7 with a side-to-thickness ratio of 20 or greater, there is no effect on the maximum deflection. But when the side-to-thickness ratio decreases, the frequency of the

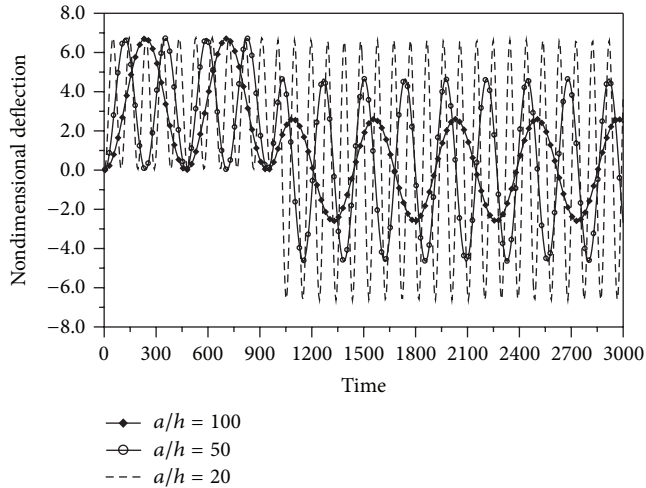


FIGURE 7: Dynamic response of nano-scale plate of variable side-to-thickness ratio under suddenly applied pulse load ( $\mu = 1$ ,  $t_1 = 1000 \mu\text{s}$ ).

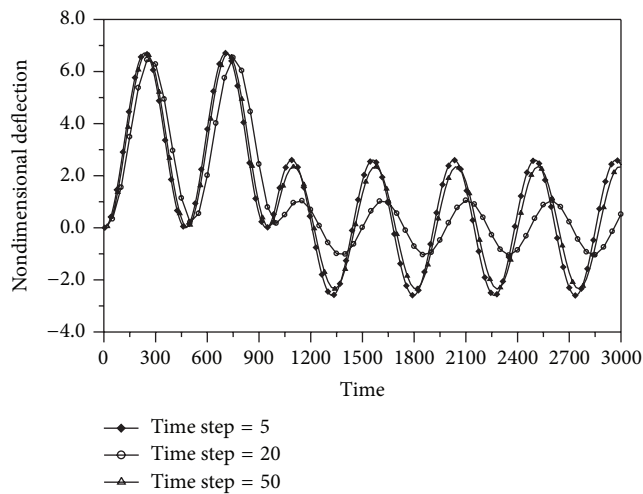


FIGURE 8: Dynamic response of nano-scale plate under suddenly applied pulse load with variable time step ( $\mu = 1$ ,  $t_1 = 1000 \mu\text{s}$ ).

dynamic response is increased; though there is no difference in its amplitude. Notably, the frequency with a the side-to-thickness ratio of 50 is twice that with a the side-to-thickness ratio of 100, due to the doubling of the thickness of the nano-scale plate.

Next, the effect of the time step on the accuracy of the solutions is investigated using a nano-scale plate under distributed pulse loading. Figure 8 shows the nondimensionalized center transverse deflection for three different time steps. A larger time step reduces the amplitude and increases the period. For all of the time steps below  $10 \mu\text{s}$ , the effect is not noticeable on the graph. In all the subsequent cases then the time step =  $5 \mu\text{s}$  is used. The difference between the maximum deflection of time step  $5 \mu\text{s}$  and that of  $50 \mu\text{s}$  is about 3%. It is expected therefore that, in order to obtain an accurate dynamic response, an appropriate choice of the loading time interval is required.

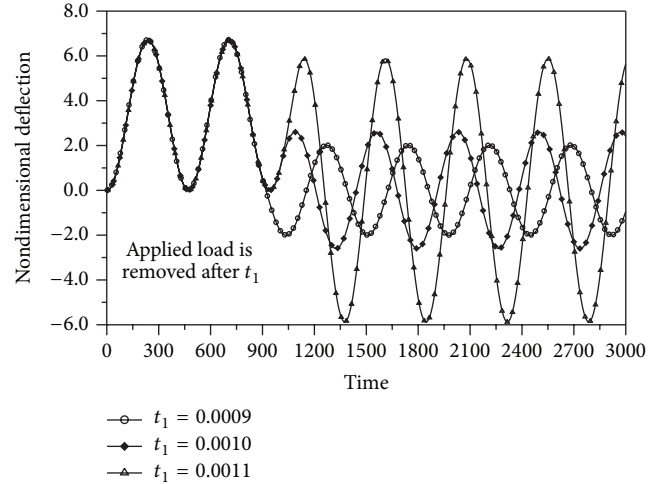


FIGURE 9: Dynamic response of nano-scale plate under suddenly applied pulse load ( $\mu = 1$ ,  $t_1 = 900 \mu\text{s}$ ,  $1000 \mu\text{s}$ , and  $1100 \mu\text{s}$ ).

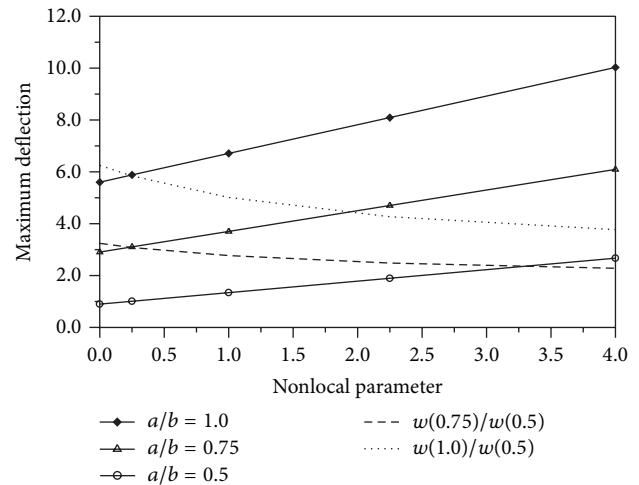


FIGURE 10: Maximum deflection of nano-scale plate of various aspect ratio with nonlocal parameter.

Figure 9 shows the dynamic response of the nano-scale plate under a suddenly applied pulse load and a variable time step. The change of the amplitude occurred according to the time in which the load is removed.

In order to study the effect of nonlocal parameter on the maximum deflection, the predicted results of the present nonlocal plate model have been illustrated in Figure 10. As it is obvious from Figure 10, the predicted results of nonlocal plate model generally increase with the nonlocal parameter, irrespective of the aspect ratio ( $a/b$ ). As the nonlocal parameter increases, the ratios ( $w_{(a/b=1.0)}/w_{(a/b=0.5)}$ ) and ( $w_{(a/b=0.75)}/w_{(a/b=0.5)}$ ) of the proposed nonlocal plate decrease. In other words, the effect of nonlocal parameters on maximum deflection is more significant when the aspect ratio is 0.5 ( $a/b = 0.5$ ).

Figure 11 plots the absolute value of maximum deflection of the nano-scale plate under suddenly applied step and

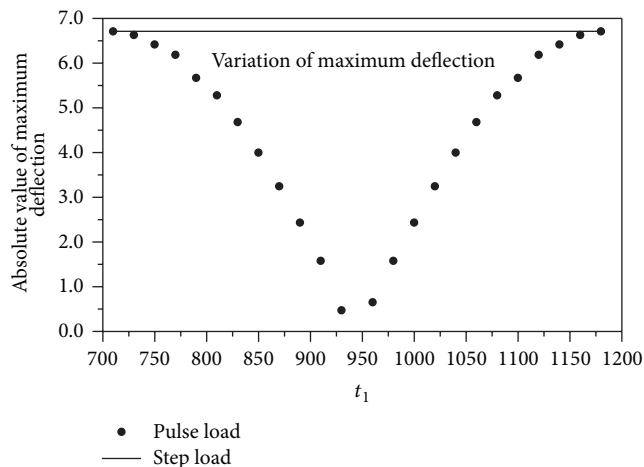


FIGURE 11: Absolute value of maximum deflection of nano-scale plate under suddenly applied step and pulse load with variable  $t_1$  ( $\mu = 1$ ).

pulse load with variable  $t_1$ . The maximum deflection when changing from 710 to 940 shows a negative value, and when changing from 950 to 1180, it shows a positive value. It would be expected that this absolute value of maximum deflection curve maintains a constant shape and that the maximum value of each deflection curves does not exceed the maximum deflection when subjected to a step load.

## 5. Conclusions

In this paper, equations of motion under nonlocal third-order shear deformation theory (TSDT) as well as analytical solutions for bending and free vibration are derived to elucidate the effect of nonlocal parameters. In order to illustrate the effects of nonlocal theories on plate response, numerical results for simply supported rectangular plates are presented. It is found that nonlocal theory can be applied to the analysis of nano-scale plates where the small size effects are significant.

Using the Eringen's nonlocal elasticity theory, the dynamic responses of nano-scale plates are studied. The higher-order shear deformation theory (HSDT) is applied to capture the quadratic variation of shear strain and consequently shear stress as function of plate thickness. It is determined that the effect of nonlocal constitutive relations is to increase the magnitude of deflections and decrease the amplitude of frequencies. Additionally, it is found that the difference between nonlocal theory and local theory is significant for high values of nonlocal parameter.

From the present work, the following conclusions are drawn.

- (1) The dynamic response computed by nonlocal elasticity is always larger compared with the local elasticity value. The stiffness of a nano-scale plate by nonlocal elasticity is small compared with that by local elasticity. Correspondingly, the amplitude and period are large.

- (2) As the size of a nano-scale plate decreases, the effect of nonlocal elasticity becomes more significant and dynamic response increased. With aspect ratio decreases of  $a/b = 1.0$  to  $0.75$  and  $0.75$  to  $0.5$ , the amplitude and frequency of the dynamic response decrease from  $1.0$  to  $0.75$ , the maximum deflection is reduced by  $45\%$ , and from  $0.75$  to  $0.5$ , there is a  $64\%$  reduction.
- (3) In the case of a nano-scale plate of side-to-thickness ratio larger than  $20$ , the effect of shear deformation is very small. When the side-to-thickness ratio decreases, there is no difference in the amplitude of the dynamic response, but its frequency increases.
- (4) The effect of a larger time step is to reduce the amplitude and increase the period. It is expected therefore that, in order to obtain accurate dynamic response, an appropriate choice of loading time interval is required.

The dynamic response of the nano-scale plate can serve as a benchmark for future guidelines to nano-scale structural design under nonlocal elasticity theory. Especially, the maximum deflection of a nano-scale plate under a suddenly applied step and pulse load with variable  $t_1$  will be contributed for the purpose of a future benchmark test applicable to the transient analysis of nano-scale structures. Further, it will be necessary to include, in transient analysis, the nonlocal elasticity theory for nano-scale shell and other boundary conditions.

## Conflict of Interests

The authors declare that there is no conflict of interests regarding the publication of this paper.

## Acknowledgments

This work was supported by the National Research Foundation of Korea (NRF) Grant funded by the Korea Government (MEST) (no. 2011-0028531).

## References

- [1] A. K. Geim and K. S. Novoselov, "The rise of graphene," *Nature Materials*, vol. 6, no. 3, pp. 183–191, 2007.
- [2] P. Ball, "Roll up for the revolution," *Nature*, vol. 414, no. 6860, pp. 142–144, 2001.
- [3] R. H. Baughman, A. A. Zakhidov, and W. A. de Heer, "Carbon nanotubes—the route toward applications," *Science*, vol. 297, no. 5582, pp. 787–792, 2002.
- [4] M. Aydogdu, "Axial vibration of the nanorods with the nonlocal continuum rod model," *Physica E*, vol. 41, no. 5, pp. 861–864, 2009.
- [5] S. C. Pradhan and J. K. Phadikar, "Small scale effect on vibration of embedded multilayered graphene sheets based on nonlocal continuum models," *Physics Letters A*, vol. 373, no. 11, pp. 1062–1069, 2009.

- [6] J. N. Reddy and S. D. Pang, "Nonlocal continuum theories of beams for the analysis of carbon nanotubes," *Journal of Applied Physics*, vol. 103, no. 2, Article ID 023511, 2008.
- [7] B. H. Bodily and C. T. Sun, "Structural and equivalent continuum properties of single-walled carbon nanotubes," *International Journal of Materials and Product Technology*, vol. 18, no. 4–6, pp. 381–397, 2003.
- [8] C. Li and T.-W. Chou, "A structural mechanics approach for the analysis of carbon nanotubes," *International Journal of Solids and Structures*, vol. 40, no. 10, pp. 2487–2499, 2003.
- [9] C. Li and T.-W. Chou, "Single-walled carbon nanotubes as ultrahigh frequency nanomechanical resonators," *Physical Review B*, vol. 68, no. 7, Article ID 073405, 2003.
- [10] C. M. Wang, V. B. C. Tan, and Y. Y. Zhang, "Timoshenko beam model for vibration analysis of multi-walled carbon nanotubes," *Journal of Sound and Vibration*, vol. 294, no. 4, pp. 1060–1072, 2006.
- [11] Q. Wang and V. K. Vardan, "Characteristics of carbon nanotubes," *International Journal of Solids and Structures*, vol. 43, pp. 254–265, 2005.
- [12] J. Peddieson, G. R. Buchanan, and R. P. McNitt, "Application of nonlocal continuum models to nanotechnology," *International Journal of Engineering Science*, vol. 41, no. 3–5, pp. 305–312, 2003.
- [13] A. C. Eringen, "On differential equations of nonlocal elasticity and solutions of screw dislocation and surface waves," *Journal of Applied Physics*, vol. 54, no. 9, pp. 4703–4710, 1983.
- [14] A. C. Eringen, *Nonlocal Continuum Field Theories*, Springer, New York, NY, USA, 2002.
- [15] H. Lu, H. Sun, A. Mao, H. Yang, H. Wang, and X. Hu, "Preparation of plate-like nano  $\alpha$ -Al<sub>2</sub>O<sub>3</sub> using nano-aluminum seeds by wet-chemical methods," *Materials Science and Engineering A*, vol. 406, no. 1–2, pp. 19–23, 2005.
- [16] T. Sumitomo, H. Kakisawa, and Y. Kagawa, "Nanoscale structure and mechanical behavior of growth lines in shell of abalone *Haliotis gigantea*," *Journal of Structural Biology*, vol. 174, no. 1, pp. 31–36, 2011.
- [17] C. M. Wang and W. H. Duan, "Free vibration of nanorings/arches based on nonlocal elasticity," *Journal of Applied Physics*, vol. 104, no. 1, Article ID 014303, 2008.
- [18] T. Murmu and S. C. Pradhan, "Buckling analysis of a single-walled carbon nanotube embedded in an elastic medium based on nonlocal elasticity and Timoshenko beam theory and using DQM," *Physica E*, vol. 41, no. 7, pp. 1232–1239, 2009.
- [19] L. Wang, "Wave propagation of fluid-conveying single-walled carbon nanotubes via gradient elasticity theory," *Computational Materials Science*, vol. 49, no. 4, pp. 761–766, 2010.
- [20] S. Narendar and S. Gopalakrishnan, "Terahertz wave characteristics of a single-walled carbon nanotube containing a fluid flow using the nonlocal Timoshenko beam model," *Physica E*, vol. 42, no. 5, pp. 1706–1712, 2010.
- [21] S. Narendar and S. Gopalakrishnan, "Ultrasonic wave characteristics of nanorods via nonlocal strain gradient models," *Journal of Applied Physics*, vol. 107, no. 8, Article ID 084312, 2010.
- [22] S. Narendar and S. Gopalakrishnan, "Strong nonlocalization induced by small scale parameter on terahertz flexural wave dispersion characteristics of a monolayer graphene," *Physica E*, vol. 43, no. 1, pp. 423–430, 2010.
- [23] Q. Wang and V. K. Vardan, "Application of nonlocal elastic shell theory in wave propagation analysis of carbon nanotubes," *Smart Materials and Structures*, vol. 16, no. 1, article 022, pp. 178–190, 2007.
- [24] S. C. Pradhan, "Buckling of single layer graphene sheet based on nonlocal elasticity and higher order shear deformation theory," *Physics Letters A*, vol. 373, no. 45, pp. 4182–4188, 2009.
- [25] J. N. Reddy, "Nonlocal nonlinear formulations for bending of classical and shear deformation theories of beams and plates," *International Journal of Engineering Science*, vol. 48, no. 11, pp. 1507–1518, 2010.
- [26] K. Kiani, "A meshless approach for free transverse vibration of embedded single-walled nanotubes with arbitrary boundary conditions accounting for nonlocal effect," *International Journal of Mechanical Sciences*, vol. 52, no. 10, pp. 1343–1356, 2010.
- [27] K. Kiani, "Nonlocal continuum-based modeling of a nanoplate subjected to a moving nanoparticle. Part I: theoretical formulations," *Physica E*, vol. 44, no. 1, pp. 229–248, 2011.
- [28] K. Kiani, "Nonlocal continuum-based modeling of a nanoplate subjected to a moving nanoparticle. Part II: parametric studies," *Physica E*, vol. 44, no. 1, pp. 249–269, 2011.
- [29] E. Jomehzadeh and A. R. Saidi, "Decoupling the nonlocal elasticity equations for three dimensional vibration analysis of nano-plates," *Composite Structures*, vol. 93, no. 2, pp. 1015–1020, 2011.
- [30] J. N. Reddy, "A simple higher-order theory for laminated composite plates," *Journal of Applied Mechanics*, vol. 51, no. 4, pp. 745–752, 1984.
- [31] J. N. Reddy and C. M. Wang, "Deflection relationships between classical and third-order plate theories," *Acta Mechanica*, vol. 130, no. 3–4, pp. 199–208, 1998.
- [32] J. N. Reddy, *Mechanics of Laminated Composite Plates and Shells*, CRC Press, Boca Raton, Fla, USA, 2nd edition, 2004.
- [33] S. J. Lee and J. N. Reddy, "Nonlinear deflection control of laminated plates using third-order shear deformation theory," *International Journal of Mechanics and Materials in Design*, vol. 1, pp. 33–61, 2004.
- [34] W.-H. Lee and S.-C. Han, "Free and forced vibration analysis of laminated composite plates and shells using a 9-node assumed strain shell element," *Computational Mechanics*, vol. 39, no. 1, pp. 41–58, 2006.
- [35] S.-C. Han, G. R. Lomboy, and K.-D. Kim, "Mechanical vibration and buckling analysis of FGM plates and shells using a four-node quasi-conforming shell element," *International Journal of Structural Stability and Dynamics*, vol. 8, no. 2, pp. 203–229, 2008.
- [36] R. Aghababaei and J. N. Reddy, "Nonlocal third-order shear deformation plate theory with application to bending and vibration of plates," *Journal of Sound and Vibration*, vol. 326, no. 1–2, pp. 277–289, 2009.
- [37] Q. Wang and C. M. Wang, "The constitutive relation and small scale parameter of nonlocal continuum mechanics for modelling carbon nanotubes," *Nanotechnology*, vol. 18, no. 7, Article ID 075702, 2007.

## Research Article

# Flux Density through Guides with Microstructured Twisted Clad DB Medium

M. A. Baqir and P. K. Choudhury

*Institute of Microengineering and Nanoelectronics, Universiti Kebangsaan Malaysia, UKM, Bangi 43600, Selangor, Malaysia*

Correspondence should be addressed to P. K. Choudhury; [pankaj@ukm.my](mailto:pankaj@ukm.my)

Received 21 October 2013; Accepted 2 December 2013; Published 2 January 2014

Academic Editor: Razali Ismail

Copyright © 2014 M. A. Baqir and P. K. Choudhury. This is an open access article distributed under the Creative Commons Attribution License, which permits unrestricted use, distribution, and reproduction in any medium, provided the original work is properly cited.

The paper deals with the study of flux density through a newly proposed twisted clad guide containing DB medium. The inner core and the outer clad sections are usual dielectrics, and the introduced twisted windings at the core-clad interface are treated under DB boundary conditions. The pitch angle of twist is supposed to greatly contribute towards the control over the dispersion characteristics of the guide. The eigenvalue equation for the guiding structure is deduced, and the analytical investigations are made to explore the propagation patterns of flux densities corresponding to the sustained low-order hybrid modes under the situation of varying pitch angles. The emphasis has been put on the effects due to the DB twisted pitch on the propagation of energy flux density through the guide.

## 1. Introduction

Metamaterials are artificially designed mediums that owe unusual phenomena, such as reversal of Snell's law and Doppler's effect, negative reflection/refraction, and many others. These exotic features are basically due to the structures of materials rather than their compositions, and are used in many interesting applications, for example, cloaking, perfect lensing, and power confinement [1–4]. References [5, 6] describe negative index chiral metamaterial based on *eight-crank molecule* designed structure; homogeneous as well as isotropic behavior of chiral medium, based on the periodic inclusion of cranks, have been demonstrated.

During the last couple of decades, complex structured guides have attracted the R&D community, primarily because of their varieties of potential applications that include optical sensing, integrated optics, and microwaves devices. The electromagnetic behavior of guides can be tailored by altering structural geometry, medium composition, and the nature of excited electromagnetic field. References [7–11] describe several forms of waveguide structures and their electromagnetic response. Reference [8] demonstrates wave propagation through chiral nihility metamaterial, a special

class of chiral medium, in which the real part of permittivity and permeability simultaneously becomes zero, while its chirality remains nonzero. In the context of complex optical micro- and/or nanostructures, helical clad optical guides offer control over the dispersion behavior through suitable adjustments of the helix pitch angle [12–16]. Such helical forms or the twists can be written on fiber structures by the use of current advancements in nanotechnology.

The usefulness of DB boundary conditions in the construction of spherical and cylindrical cloaks has been reported in the literature [3]. Within the context, the DB boundary conditions were introduced by Lindell et al. [17–19], in which the normal components of both electric and magnetic fields vanish at the interface [20–22]. DB medium can be easily realized in the case of anisotropic medium if the normal component of permittivity and permeability simultaneously becomes zero; that is,

$$\hat{n} \cdot \vec{B} = 0, \quad \hat{n} \cdot \vec{D} = 0. \quad (1)$$

In the case of isotropic medium, the boundary conditions can be written as

$$\hat{n} \cdot \vec{H} = 0, \quad \hat{n} \cdot \vec{E} = 0. \quad (2)$$

In the present paper, we investigate the propagation through twisted clad guiding medium, wherein helical windings are introduced as DB medium at the dielectric core-clad interface. To the best of our knowledge, such guiding structures are not yet discussed in the literature, and the present work would be the first investigation of the fundamental electromagnetic behavior of microstructured guides with DB medium twisted clad. Rigorous analyses are made of the associated boundary-value problem implementing Maxwell's equations, and the dispersion relations of the guide are deduced followed by the estimation of supported flux density patterns.

## 2. Theoretical Approach

We consider a cylindrical twisted clad guiding medium, as shown in Figure 1, the core/clad sections of which are linear, isotropic, homogeneous, and lossless dielectrics. A DB based microstructured sheath helix is introduced at the core-clad interface, treated under the suitable boundary conditions. Although the sheath is tightly wound, each of the turns is insulated from the neighboring ones. In Figure 1,  $\Psi$  represents the angle that the conducting helical windings make with respect to the normal drawn on to the fiber surface in the longitudinal direction.

We assume  $n_{\text{core}}$  and  $n_{\text{clad}}$  as the refractive indices (RIs) of core and clad regions of the guide, respectively, and  $a$  as the core radius, the clad section being infinitely extended. The time  $t$ -harmonic and axis  $z$ -harmonic wave propagates down the guiding structure, considering the guide to be elongated along the  $z$ -direction. Such an assumption leads to the transverse electric/magnetic field components to be of the forms as

$$E_{r1} = -\frac{j}{u^2} \left[ \beta u A J'_v(ur) + \frac{j\omega\mu v}{r} B J_v(ur) \right] e^{j(\omega t - \beta z + v\varphi)}, \quad (3a)$$

$$H_{r1} = \frac{j}{u^2} \left[ \frac{j\omega\mu v}{r} A J_v(ur) - \beta u B J'_v(ur) \right] e^{j(\omega t - \beta z + v\varphi)}, \quad (3b)$$

$$E_{\varphi 1} = -\frac{j}{u^2} \left[ \frac{j\beta v}{r} A J_v(ur) - \omega\mu u B J'_v(ur) \right] e^{j(\omega t - \beta z + v\varphi)}, \quad (4a)$$

$$H_{\varphi 1} = -\frac{j}{u^2} \left[ \omega\mu u A J'_v(ur) + \frac{j\beta v}{r} B J_v(ur) \right] e^{j(\omega t - \beta z + v\varphi)}, \quad (4b)$$

wherein  $u = \sqrt{(n_{\text{core}} k_0)^2 - \beta^2}$ . Similarly, the transverse components of fields in the clad section can be written as

$$E_{r2} = -\frac{j}{w^2} \left[ \beta w C K'_v(wr) + \frac{j\omega\mu v}{w} D K_v(wr) \right] e^{j(\omega t - \beta z + v\varphi)}, \quad (5a)$$

$$H_{r2} = \frac{j}{w^2} \left[ \frac{j\omega\mu v}{r} C K_v(wr) - \beta w D K'_v(wr) \right] e^{j(\omega t - \beta z + v\varphi)}, \quad (5b)$$

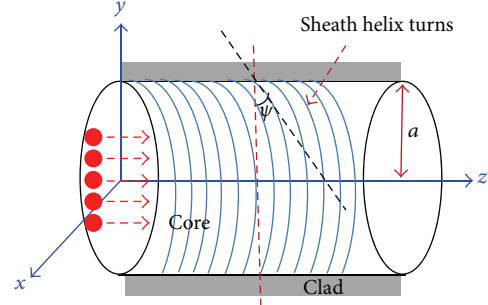


FIGURE 1: Longitudinal view of the guiding structure.

$$E_{\varphi 2} = -\frac{j}{w^2} \left[ \frac{j\beta v}{r} C K_v(wr) - \omega\mu w D K'_v(wr) \right] e^{j(\omega t - \beta z + v\varphi)}, \quad (6a)$$

$$H_{\varphi 2} = -\frac{j}{w^2} \left[ \omega\mu w C K'_v(wr) + \frac{j\beta v}{r} D K_v(wr) \right] e^{j(\omega t - \beta z + v\varphi)}, \quad (6b)$$

with  $w = \sqrt{\beta^2 - (n_{\text{clad}} k_0)^2}$ . In the above set of equations,  $\mu$  and  $\epsilon$  are, respectively, the permeability and the permittivity of the medium,  $\omega$  is the angular frequency in the unbounded medium,  $\beta$  is the propagation constant in the medium,  $k_0$  is the free-space propagation constant,  $v$  is the azimuthal mode index, and primes represent differentiation with respect to the arguments of field functions. Also  $A$ ,  $B$ ,  $C$ , and  $D$  are unknown constants, to be estimated by the use of boundary conditions.

Now, considering the existence of DB twisted clad, boundary conditions will essentially include vanishing normal components of electric/magnetic fields and continuous tangential components of the same at the medium interface. Implementation of this ultimately leads to the evolution of a set of four homogeneous equations, followed by the dispersion relation (as obtained by collecting the coefficients of unknown constants) given as

$$\begin{aligned} f(\beta) &= \frac{1}{4} \omega^2 \mu \epsilon w^2 \{K_{v-1}(aw) + K_{v+1}(aw)\}^2 \sin^2 \psi \\ &\times \left[ \frac{v^2 \omega^2 \mu \epsilon}{a^2 u^4} J_v^2(au) (\cos \psi - \sin \psi)^2 \right. \\ &\quad \left. - \frac{\beta^2}{4} \{J_{v-1}(au) - J_{v+1}(au)\}^2 (\sin \psi - \cos \psi)^2 \right] \\ &+ \left\{ K_v(aw) \cos \psi + \frac{v\beta}{aw^2} J_v(au) \sin \psi \right\} \\ &\times \left\{ K_v(aw) \cos \psi - \frac{v\beta}{aw^2} K_v(aw) \cos \psi \right\} \\ &\times \left\{ \frac{v^2 \mu \epsilon \omega^2}{a^2 u^4} J_v^2(au) - \frac{1}{4} \beta^2 (J_{v-1}(au) - J_{v+1}(au))^2 \right\} \\ &\times (\sin \psi - \cos \psi)^2 = 0. \end{aligned} \quad (7)$$

The unknown coefficients could be determined solving the aforesaid four equations obtained after implementing the boundary conditions. After some rigorous mathematical steps, the coefficients  $A$ ,  $B$ , and  $C$  can be determined in terms of the coefficient  $D$  as follows:

$$A = -j \frac{u^2 a J'_v(ua) \Theta (u^2 a \gamma \Delta - \Xi \xi) + w^2 a (\Theta \xi - \omega \epsilon K_v(wa))}{\omega \epsilon a w^2 \gamma (\Theta \xi - \omega \epsilon K_v(wa) \delta)} D,$$

$$B = \frac{u J_v(ua) \Theta (u^2 a \gamma \Delta - \Xi \xi) + w^2 a (\Theta \xi - \omega \epsilon K_v(wa) \delta)}{w^2 a \gamma (\Theta \xi - \omega \epsilon K_v(wa) \delta)} D,$$

$$C = j \frac{u^2 a \gamma \Delta - \omega^2 \mu \epsilon w^3 K'_v(wa) \xi}{\omega \epsilon K_v(wa) (w^2 a \cos \psi - \beta v \sin \psi) \xi - \delta} D, \quad (8)$$

where

$$\begin{aligned} \gamma &= \omega^2 \mu \epsilon u^2 J_v(ua) J'_v(ua) \sin \psi \\ &\quad - \beta J'_v(ua) (u^2 a J_v(ua) \cos \psi + \beta v J_v(ua) \sin \psi), \\ \xi &= J_v^2(ua) (u^2 a \cos \psi + \beta v \sin \psi) - \beta u^2 a^2 J'_v(ua) \sin \psi, \\ \Theta &= \omega \epsilon K_v(wa) (w^2 a \cos \psi - \beta v \sin \psi), \\ \Delta &= w^2 K_v(wa) \cos \psi + \beta v K_v(wa) \sin \psi, \\ \Xi &= \omega^2 \mu \epsilon w^3 K_v(wa) \sin \psi, \\ \delta &= \omega \epsilon u w a^2 K_v(wa) \sin \psi. \end{aligned} \quad (9)$$

Now, the flux density in the guide along the direction of propagation can be estimated, and, following the procedure in [11], it will finally assume the forms corresponding to the core/clad sections, as follows:

$$(S_z)_{\text{Core}} = \frac{\beta}{2u^4} (\epsilon |A|^2 + \mu |B|^2) \left\{ \left( \frac{v}{r} \right)^2 J_v^2(ur) + \left( \frac{u}{2} \right)^2 \sigma \right\},$$

$$(S_z)_{\text{Clad}} = \frac{\beta}{2w^4} (\epsilon |C|^2 + \mu |D|^2) \left\{ \left( \frac{v}{r} \right)^2 K_v^2(wr) + \left( \frac{w}{2} \right)^2 \Lambda \right\}, \quad (10)$$

with

$$\begin{aligned} \sigma &= J_{v-1}^2(ur) + J_{v+1}^2(ur) - 2J_{v-1}(ur) J_{v+1}(ur), \\ \Lambda &= K_{v-1}^2(wr) + K_{v+1}^2(wr) - 2K_{v-1}(wr) K_{v+1}(wr). \end{aligned} \quad (11)$$

Equations (10) can be written in terms of only one unknown constant, for example, in terms of  $D$ , as determined by the use of (8).

### 3. Results and Discussion

We now investigate the propagation features of flux density through DB twisted clad microstructured guide. However, for this purpose, it remains essential to evaluate the allowed values of propagation constants corresponding to different sustained modes under the conditions when the DB twists are typically oriented perpendicular as well as parallel to

TABLE I: Hybrid mode propagation constants.

Pitch angle $\psi$	Core radius $a$	Mode	Propagation constant $\beta$ ( $\text{m}^{-1}$ )
$0^\circ$	$10 \mu\text{m}$	$\text{EH}_{01}$	$5.970 \times 10^6$
		$\text{EH}_{11}$	$5.975 \times 10^6$
		$\text{EH}_{21}$	$5.968 \times 10^6$
	$20 \mu\text{m}$	$\text{EH}_{01}$	$5.960 \times 10^6$
		$\text{EH}_{11}$	$5.965 \times 10^6$
		$\text{EH}_{21}$	$5.970 \times 10^6$
$90^\circ$	$10 \mu\text{m}$	$\text{EH}_{01}$	$5.850 \times 10^6$
		$\text{EH}_{11}$	$5.890 \times 10^6$
		$\text{EH}_{21}$	$5.870 \times 10^6$
	$20 \mu\text{m}$	$\text{EH}_{01}$	$5.950 \times 10^6$
		$\text{EH}_{11}$	$5.980 \times 10^6$
		$\text{EH}_{21}$	$5.965 \times 10^6$

the direction of wave propagation. For the computational purpose, we consider the RI values of the core and the clad sections as 1.485 and 1.470, respectively, and the operating wavelength is taken to be  $1.55 \mu\text{m}$ . The chosen parameters are, indeed, the widely accepted ones in the case of modeling and simulations related to the electromagnetic properties of optical fibers. Also, we consider two typical values of core radius as  $10 \mu\text{m}$  and  $20 \mu\text{m}$ , the clad radius being fixed at  $100 \mu\text{m}$ . The behavior of normalized flux density through core/clad regions is studied considering three low-order hybrid  $\text{EH}_{01}$ ,  $\text{EH}_{11}$ , and  $\text{EH}_{21}$  modes having propagation constants, as obtained by the use of eigenvalue (7), as shown in Table I.

Figures 2(a) and 2(b), respectively, demonstrate the normalized flux density patterns through core and clad regions of guide having core radius  $10 \mu\text{m}$  under the situation when the DB twist is oriented perpendicular to the direction of propagation; that is,  $\Psi = 0^\circ$ . In all the figures, the results corresponding to the  $\text{EH}_{01}$ ,  $\text{EH}_{11}$ , and  $\text{EH}_{21}$  modes are represented by black dash-dot, solid red, and dashed blue lines. We observe from Figure 2(a) that the flux generally exhibits an oscillatory trend in the core region of the guiding medium. Also, in the central region of the core,  $\text{EH}_{11}$  hybrid mode has higher energy than the other two  $\text{EH}_{01}$  and  $\text{EH}_{21}$  modes. Further, flux densities due to the  $\text{EH}_{01}$  and  $\text{EH}_{11}$  modes decrease with the increase in radial distance, whereas that due to the  $\text{EH}_{21}$  mode exhibits a minor increase only.

In the clad section, as Figure 2(b) shows, the aforesaid three hybrid modes exhibit similar flux characteristics, and it remains extremely small as compared to that in the core region. At the core-clad interface, it shows relatively large value, and then step-falls with a little increase in clad radius, and become almost vanishing as the radius is further increased.

Figures 3(a) and 3(b) correspond to the situations when the DB helical windings are put parallel to the optical axis, that is, the helix pitch  $\Psi = 90^\circ$ . We observe in this case that the confinements of flux in the core section (Figure 3(a)) exhibit almost similar patterns, as observed in the case when

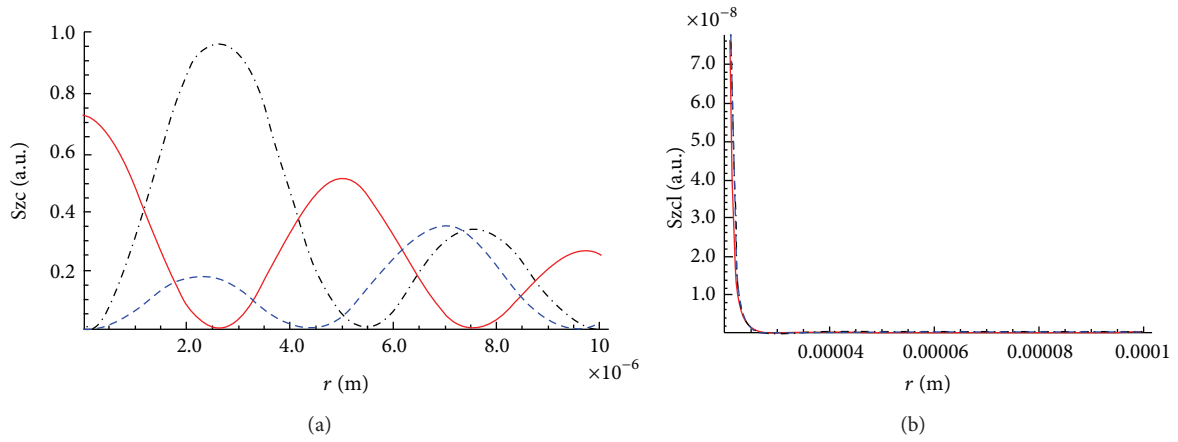


FIGURE 2: Flux density through the core (a) and clad (b) corresponding to  $10 \mu\text{m}$  core radius and  $0^\circ$  helix pitch.

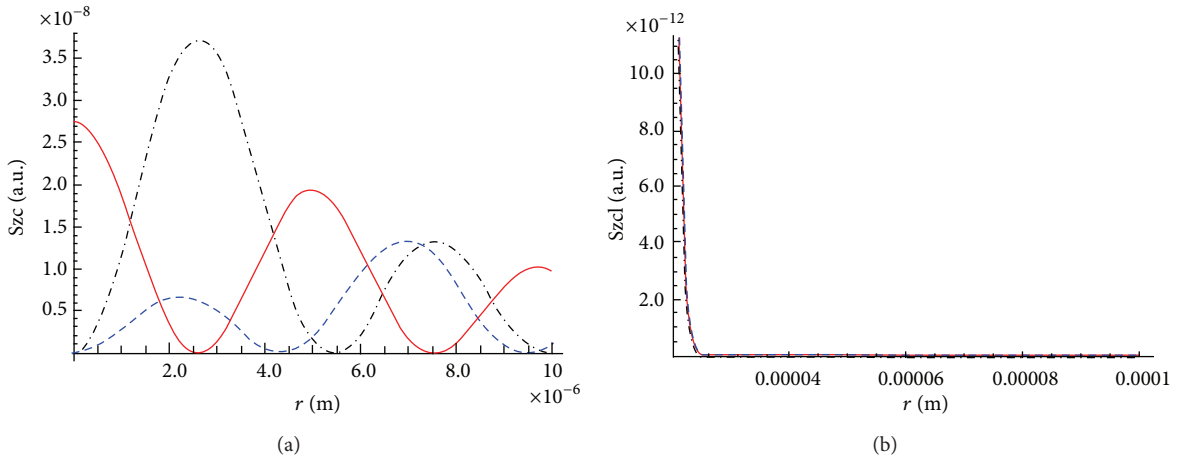


FIGURE 3: Flux density through the core (a) and clad (b) corresponding to  $10 \mu\text{m}$  core radius and  $90^\circ$  helix pitch.

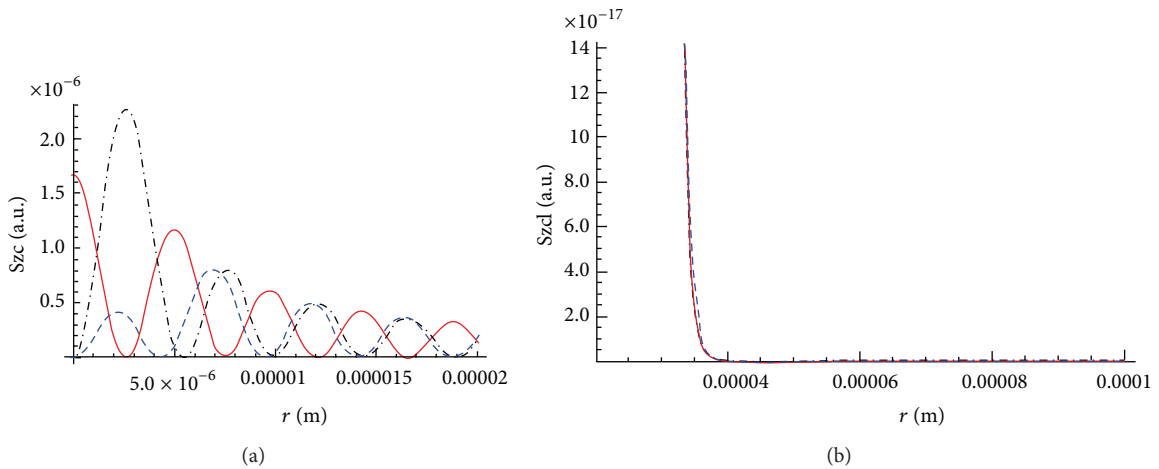


FIGURE 4: Flux density through the core (a) and clad (b) corresponding to  $20 \mu\text{m}$  core radius and  $0^\circ$  helix pitch.

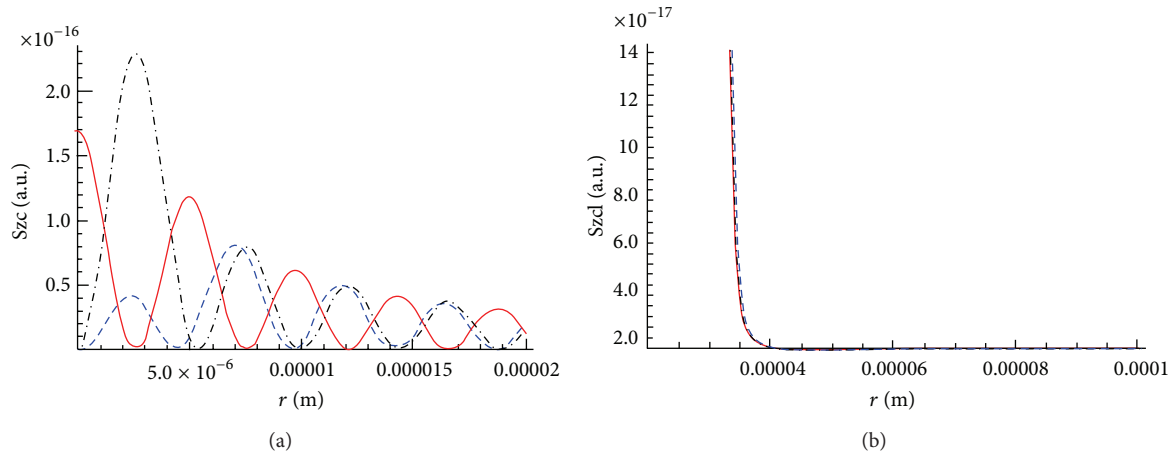


FIGURE 5: Flux density through the core (a) and clad (b) corresponding to 20  $\mu\text{m}$  core radius and  $90^\circ$  helix pitch.

DB twists are oriented in the direction perpendicular to the wave propagation (Figure 2(a)), but its values are drastically reduced corresponding to all the sustained modes. Otherwise, the  $\text{EH}_{01}$  and  $\text{EH}_{11}$  modes correspond to higher power than the  $\text{EH}_{21}$  mode in the central region of core section. In the clad section too, the flux is further reduced (Figure 3(b)) as compared to the case of Figure 2(b), exhibiting similar density patterns, as observed before, for the situation of  $\Psi = 0^\circ$ . Thus, comparing the results of Figures 2 and 3, we notice the effect of introducing DB sheath helix structure at the dielectric core-clad interface. We find that making the angle of pitch (of DB helix) as  $90^\circ$  greatly reduces the propagation of power, and therefore, a change in pitch would make the guide to amplify or attenuate the signal depending upon lowering or increasing its value. This clearly demonstrates the importance of such guiding structures.

Figures 4 and 5 correspond to the situation when the core radius is doubled, that is, increased to 20  $\mu\text{m}$ . We observe that the trends of flux density patterns are almost similar to the situation as observed before for 10  $\mu\text{m}$ , but the oscillations of flux are increased in this case. This is very much obvious due to more room for the fields to be sustained, thereby causing dispersion and so forth. However, in this as well, we observe that the increase of pitch of DB twist essentially reduces the flow of flux density, as evidenced by Figures 4 and 5.

#### 4. Conclusion

The eigenvalue equation is deduced for the aforesaid structure, and the propagation features of the low-order hybrid modes are estimated. Investigations are made of the energy flux density patterns corresponding to the sustained modes, and the effects are observed due to the alterations of pitch angles of the microstructured DB twists introduced at the dielectric core-clad interface. The flux patterns reveal profound effect of helix pitch, and making the DB windings parallel to the axis of guide greatly reduces power confinements in the guiding region. As such, these guides may be used for the purpose of amplifying and/or attenuating signals in optical systems.

#### Conflict of Interests

The authors declare that there is no conflict of interest regarding the publication of this manuscript.

#### Acknowledgments

The authors are grateful to Professors S. Shaari and B.Y. Majlis for constant encouragement and help. Also, they are thankful for the Ministry of Higher Education (Malaysia) for providing financial support to the work. The authors are grateful to the anonymous reviewer for making constructive criticisms.

#### References

- [1] V. G. Veselago, "The electrodynamics of substances with simultaneously negative values of  $\epsilon$  and  $\mu$ ," *Soviet Physics Uspekhi*, vol. 10, no. 4, pp. 509–514, 1968.
- [2] J. B. Pendry, "Negative refraction makes a perfect lens," *Physical Review Letters*, vol. 85, no. 18, pp. 3966–3969, 2000.
- [3] A. D. Yaghjian, "Extreme electromagnetic boundary conditions and their manifestation at the inner surfaces of spherical and cylindrical cloaks," *Metamaterials*, vol. 4, no. 2-3, pp. 70–76, 2010.
- [4] N. Landy and D. R. Smith, "A full-parameter unidirectional metamaterial cloak for microwave," *Nature Materials*, vol. 12, pp. 25–28, 2013.
- [5] A. J. Garcia-Collado, G. J. Molina-Cuberos, J. Margineda, M. J. Núñez, and E. Martín, "Isotropic and homogeneous behavior of chiral media based on periodical inclusions of cranks," *IEEE Microwave and Wireless Components Letters*, vol. 20, no. 3, pp. 175–177, 2010.
- [6] G. J. Molina-Cuberos, Á. J. García-Collado, I. Barba, and J. Margineda, "Chiral metamaterials with negative refractive index composed by an eight-cranks molecule," *IEEE Antennas and Wireless Propagation Letters*, vol. 10, pp. 1488–1490, 2011.
- [7] P. K. Choudhury and R. A. Lessard, "An estimation of power transmission through a doubly clad optical fiber with an annular core," *Microwave and Optical Technology Letters*, vol. 29, no. 6, pp. 402–405, 2001.

- [8] S. Tretyakov, I. Nefedov, A. Sihvola, S. Maslovski, and C. Simovski, "Waves and energy in chiral nihility," *Journal of Electromagnetic Waves and Applications*, vol. 17, no. 5, pp. 695–706, 2003.
- [9] S. C. Yeow, M. H. Lim, and P. K. Choudhury, "A rigorous analysis of the distribution of power in plastic clad linear tapered fibers," *Optik*, vol. 117, no. 9, pp. 405–410, 2006.
- [10] P. K. Choudhury and W. K. Soon, "On the transmission by liquid crystal tapered optical fibers," *Optik*, vol. 122, no. 12, pp. 1061–1068, 2011.
- [11] M. A. Baqir and P. K. Choudhury, "On the energy flux through a uniaxial chiral metamaterial made circular waveguide under PMC boundary," *Journal of Electromagnetic Waves and Applications*, vol. 26, no. 16, pp. 2165–2175, 2012.
- [12] U. N. Singh, O. N. Singh II, P. Khastgir, and K. K. Dey, "Dispersion characteristics of a helically clad step-index optical fiber—analytical study," *Journal of the Optical Society of America B*, vol. 12, no. 7, pp. 1273–1278, 1995.
- [13] D. Kumar and O. N. Singh II, "Modal characteristic equation and dispersion curves for an elliptical step-index fiber with a conducting helical winding on the core-cladding boundary—an analytical study," *Journal of Lightwave Technology*, vol. 20, no. 8, pp. 1416–1424, 2002.
- [14] C. C. Siong and P. K. Choudhury, "Propagation characteristics of tapered core helical clad dielectric optical fibers," *Journal of Electromagnetic Waves and Applications*, vol. 23, no. 5, pp. 663–674, 2009.
- [15] K. Y. Lim, P. K. Choudhury, and Z. Yusoff, "Chirofibers with helical windings—an analytical investigation," *Optik*, vol. 121, no. 11, pp. 980–987, 2010.
- [16] M. Ghasemi and P. K. Choudhury, "On the sustainment of optical power in twisted clad dielectric cylindrical fiber," *Journal of Electromagnetic Waves and Applications*, vol. 27, no. 11, pp. 1382–1391, 2013.
- [17] I. V. Lindell and A. H. Sihvola, "Electromagnetic boundary and its realization with anisotropic metamaterial," *Physical Review E*, vol. 79, no. 2, Article ID 026604, 2009.
- [18] I. V. Lindell, H. Wallén, and A. Sihvola, "General electromagnetic boundary conditions involving normal field components," *IEEE Antennas and Wireless Propagation Letters*, vol. 8, pp. 877–880, 2009.
- [19] I. V. Lindell and A. H. Sihvola, "Electromagnetic boundary conditions defined in terms of normal field components," *IEEE Transactions on Antennas and Propagation*, vol. 58, no. 4, pp. 1128–1135, 2010.
- [20] I. V. Lindell, A. Sihvola, L. Bergamin, and A. Favaro, "Realization of the  $D'B'$  boundary condition," *IEEE Antennas and Wireless Propagation Letters*, vol. 10, pp. 643–646, 2011.
- [21] I. V. Lindell and A. H. Sihvola, "SHDB boundary condition realized by pseudo-chiral media," *IEEE Antennas and Wireless Propagation Letters*, vol. 12, pp. 591–594, 2013.
- [22] M. A. Baqir and P. K. Choudhury, "Propagation through uniaxial anisotropic chiral waveguide under DB boundary conditions," *Journal of Electromagnetic Waves and Applications*, vol. 27, no. 6, pp. 783–793, 2013.

## Research Article

# Optimization of DNA Sensor Model Based Nanostructured Graphene Using Particle Swarm Optimization Technique

Hediyeh Karimi,<sup>1,2</sup> Rubiyah Yusof,<sup>1,2</sup> Rasoul Rahmani,<sup>1</sup> and Mohammad Taghi Ahmadi<sup>3,4</sup>

<sup>1</sup> Centre for Artificial Intelligence and Robotics, Universiti Teknologi Malaysia, 54100 Kuala Lumpur, Malaysia

<sup>2</sup> Malaysia-Japan International Institute of Technology (MJIIT), Universiti Teknologi Malaysia, 54100, Malaysia

<sup>3</sup> Computational Nanoelectronic Research Group, Faculty of Electrical Engineering, Universiti Teknologi Malaysia, 81310 Johor, Malaysia

<sup>4</sup> Physics Department, Nanotechnology Research Center Nanoelectronic Group, Urmia University, Urmia 57147, Iran

Correspondence should be addressed to Rubiyah Yusof; [rubiyah@ic.utm.my](mailto:rubiyah@ic.utm.my)

Received 14 July 2013; Revised 5 October 2013; Accepted 6 November 2013

Academic Editor: Munawar A. Riyadi

Copyright © 2013 Hediyeh Karimi et al. This is an open access article distributed under the Creative Commons Attribution License, which permits unrestricted use, distribution, and reproduction in any medium, provided the original work is properly cited.

It has been predicted that the nanomaterials of graphene will be among the candidate materials for postsilicon electronics due to their astonishing properties such as high carrier mobility, thermal conductivity, and biocompatibility. Graphene is a semimetal zero gap nanomaterial with demonstrated ability to be employed as an excellent candidate for DNA sensing. Graphene-based DNA sensors have been used to detect the DNA adsorption to examine a DNA concentration in an analyte solution. In particular, there is an essential need for developing the cost-effective DNA sensors holding the fact that it is suitable for the diagnosis of genetic or pathogenic diseases. In this paper, particle swarm optimization technique is employed to optimize the analytical model of a graphene-based DNA sensor which is used for electrical detection of DNA molecules. The results are reported for 5 different concentrations, covering a range from 0.01 nM to 500 nM. The comparison of the optimized model with the experimental data shows an accuracy of more than 95% which verifies that the optimized model is reliable for being used in any application of the graphene-based DNA sensor.

## 1. Introduction

In the recent decade, DNA biosensors have been widely considered as a promising means of diagnostic prediction in genetic research such as cancer or hereditary disease due to their rapid and sensitive response, as well as the simple and convenient operation [1, 2]. The interface between nanomaterials and biosystems is emerging as one of the most various and dynamic areas of intense research [3]. In order to overcome the limit of planar semiconductor devices regarding sensitivity and potential for integration [4, 5], these nanomaterials are commonly proposed in sensor platform. Nanoscale channel confinement of planar FETs makes them extremely sensitive to electric perturbations, due to their one-dimensional structures. Therefore, obtaining a high sensitivity does not provide a worthy and reliable sensor. The implementation of nanomaterials of graphene in graphene field effect transistor (GFETs) constitutes an

important step toward low-cost, easy handle, and highly sensitive molecular diagnostics [6, 7]. On the other hand, graphene with a two-dimensional thick monoatomic block of a carbon allotrope offers a large detection area (as seen in Figure 1) for DNA sensing compared with other known nanomaterials [8–11].

The research to date tends to focus on the impact of graphene-based materials in electronic and optoelectronic devices along with their potential applications [6].

## 2. Materials and Methods

**2.1. Graphene-Based DNA Sensor Structure.** Over the past few decades, a lot of information has become available on field-effect devices for DNA detection which is reported in the literature [12–21]. DNA sensors usually presented in diverse sensor configurations such as electrolyte-silicon (ES) structures, depletion- and enhancement-mode FETs, floating-gate

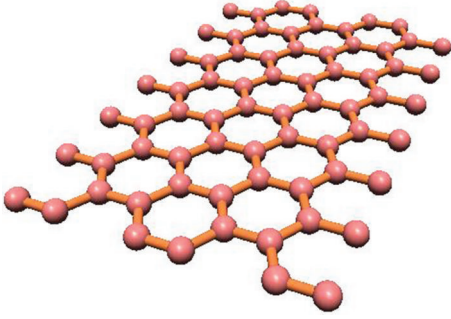


FIGURE 1: Monolayer graphene structure with one atom thickness.

FET, and FET devices with or without a reference electrode.  $\text{SiO}_2$ , silanized  $\text{SiO}_2$ ,  $\text{SiO}_2\text{-Si}_3\text{N}_4$ ,  $\text{SiO-poly-L-lysine}$  were employed as various gate-insulator materials with different thicknesses (from 2 to 100 nm) in various DNA immobilization methods (such as adsorption, covalent attachment, biotin-vidin complexation, and linker molecules) [22]. As reported in [16], the densities of the immobilized DNA varies from  $2.4 \times 10^8$  to  $5 \times 10^{13}$  molecules/ $\text{cm}^2$  and hybridization buffer solutions with different electrolyte concentrations (from 10 nM to 1 nM) were examined to obtain the higher adsorption. In addition, the mostly reported flat-band or threshold voltage shift induced upon the DNA hybridization reach from several mV up to around 1.9 V. The focus of this theoretical study will be on developing the DNA-sensors-based graphene nanomaterials which have emerged as one of the most popular devices holding great promise to provide a straightforward platform of patience diagnosis [23, 24].

As shown in Figure 2, the schematic of the DNA sensor consists of a 300-nm  $\text{SiO}_2$  layer as a back-gate dielectric and a doped silicon substrate as the back gate which was proposed for modeling of DNA sensor in our previous studies [9, 25]. Based on that, graphene layer acts as a conducting channel connected to the source and drain electrodes which are made from  $\text{Au}$ . An  $\text{Ag/AgCl}$  reference electrode commonly acts as a gate for measuring the electrical characteristics in a liquid-gated or electrochemically gated configuration that controls the current along the graphene sheet between the two electrodes [26–28]. Considering that the gate leakage effect is not considered in the current study, the DNA sensors were exposed to a phosphate buffer solution (PBS) containing the DNA molecules. In order to understand whether DNA molecules are adsorbed on the graphene surface or not, source-drain conductance were measured before and after exposing the DNA sensor to the different concentration of DNA molecules [3].

It is noteworthy to explain the DNA adsorption effect on nanomaterials of graphene surface, as well as the proposed model. The FET devices are very practical for measuring the surface charge and therefore the charge changes because a DNA adsorption event can be measured with a high accuracy. It has been demonstrated that the interaction between DNA molecules and graphene layer causes a significant change in the conductance of the graphene-based DNA sensor through the nonelectrostatic gating mechanism

[29, 30]. In Figure 3, the effect of DNA concentration on the gate voltage at nanomolar concentrations is explored. It is generally suggested that the electronic-doping (n-doping) effect by the adsorbed charge species has a significant impact on conductance change of graphene-based transistors [31]. Moreover, the conductivity of the graphene-based DNA sensor is influenced by the increased number of carriers in the channel. As the number of DNA molecules increased from 0.01 to 500 nM, due to the negative charges of DNA molecules, it could be expected that the gate voltage would shift leftwards to the lower amounts [32, 33]. Based on the detection mechanism, we recently proposed an analytical model for detection of DNA molecules in which the DNA concentration was modeled by a gate voltage [9].

Although there are lots of works presented on the experimental progress, the detection mechanism is not understood quantitatively. On the other hand, modeling and simulation using partial differential equations (PDE) play a critical role in determining the current-voltage characteristics, sensitivity, and the behaviour of the sensing devices exposed to DNA molecules. Our proposed model is capable of performing the electrical detection of DNA molecules by modeling the conductance of the graphene sheets. The conductance of the large channel in graphene materials is obtained in the ohmic scaling law using Landauer formula [34].

Consider

$$G = \frac{2q^2}{h} \int_{-\infty}^{+\infty} dEM(E)T(E) \left( -\frac{df}{dE} \right), \quad (1)$$

where  $q$  is the electron charge,  $h$  denotes Planck's constant,  $E$  represents the energy band structure,  $T(E)$  is the transmission probability,  $M(E)$  is the number of modes, and  $f$  denotes the Fermi-Dirac distribution function [34, 35]. In other words,  $T(E)$  is the average probability of electron transmission in the channel from one electrode to another. Since the channel is assumed ballistic, the probability is considered equal to one ( $T(E) = 1$ ) [36–38]. In order to highlight the effect of DNA adsorption on graphene, DNA concentration as a function of gate voltage is assumed and sensing factor is defined. High carrier mobility reported from experiments in the graphene leads to assume a completely ballistic carrier transportation in the graphene [39]. In the nonsaturation region, the DNA concentration model is employed as a function of gate voltage and the ideal current-voltage relation for the n-channel FET from [34] is modified as

$$I_d = \frac{3q^2 (3\pi a^3 t^3 k_{BT})^{1/2}}{hL} \times [\mathcal{F}_{-1/2}(\eta) + \mathcal{F}_{-1/2}(-\eta)] \times \left( \frac{\alpha}{F} V_{gs(\text{withoutDNA})} - V_t \right), \quad (2)$$

where  $a_{\text{C-C}} = 1.42 \text{ \AA}$  is carbon-carbon (C–C) bond length,  $t = 2.7 \text{ (eV)}$  is the nearest neighbor C–C tight binding overlap energy,  $L$  is the length of conducting channel,  $V_t$  refers to the threshold voltage,  $\alpha$  is DNA sensing factor, and  $F$  is DNA concentration. Different concentrations of DNA molecules

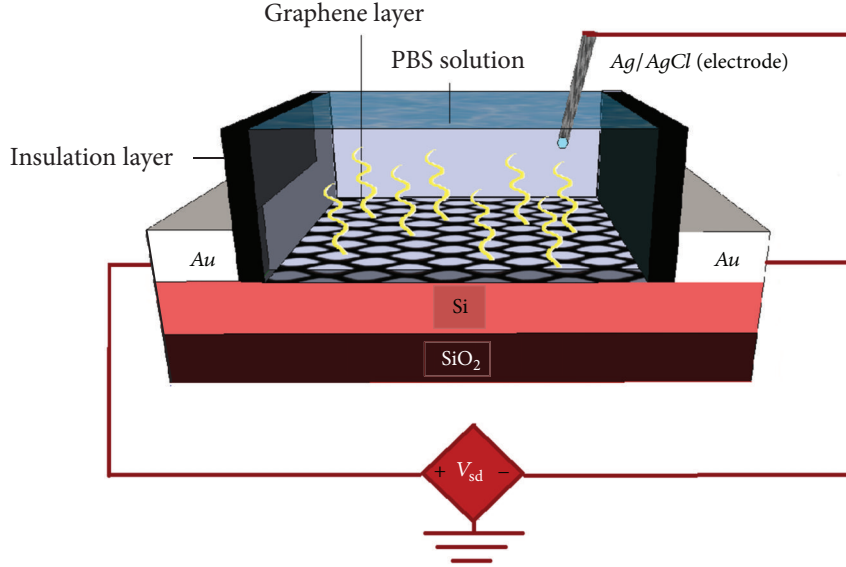


FIGURE 2: Schematics of DNA sensor measurement setup operated by liquid gating where a device is gated through an  $Ag/AgCl$  reference electrode inserted in the electrolyte.

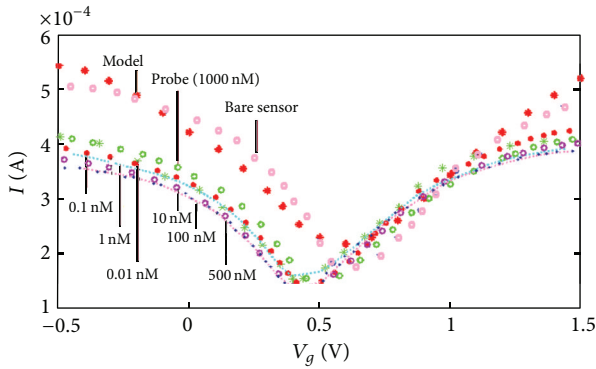


FIGURE 3: Transfer characteristics of graphene FET for different concentrations of DNA molecule.

were presented in the form of  $F$  parameter. Thus, the DNA molecules adsorbed on graphene surface by iteration method are modeled as

$$\alpha = AF^2 + BF + C. \quad (3)$$

From extracted data,  $(A, B, C)$  parameters are calculated and obtained as  $A = 13$ ,  $B = 50$ , and  $C = 4070$ . Eventually, according to the proposed model of DNA sensor using nanostructured graphene layer, the current-voltage characteristic is modified as

$$I_d = \frac{3q^2 (3\pi a^3 t^3 k_{BT})^{1/2}}{hL} \times [\mathcal{F}_{-1/2}(\eta) + \mathcal{F}_{-1/2}(-\eta)] \times \left( \frac{13F^2 + 50F + 4070}{F} V_{gs(\text{withoutDNA})} - V_t \right). \quad (4)$$

All theoretical  $I_d$ - $V_g$  characteristics of graphene FET for DNA concentration are plotted in [30] changing from 0.01 to 500 nM. It is stated that the sensor model with the proposed parameters represents the same trends as those reported as experimental data [3, 9]. Since the values of the parameters  $A$ ,  $B$ , and  $C$  in (3) are calculated based on trial and error, there is necessity of a methodological approach for obtaining a viable and accurate model which is reliable for being used in different applications of the graphene-based DNA sensor. To this aim, a swarm-based evolutionary algorithm (EA) called particle swarm optimization (PSO) is used for optimizing the mathematical model shown in (3). In important applications of DNA sensors such as hybridization detection, the behaviour of  $I_d$ - $V_g$  characteristic around  $V_{g \min}$  is very important and determinant. Therefore, a proper and reliable model should be capable of providing the same features with experimental data around the mentioned area. The better the modelled curve fits the experimental result, the more the reliable model is achieved. In the current study, the optimized model using PSO provides a fitter  $I_d$ - $V_g$  characteristic compared with the previous mathematic model, especially around the  $V_{g \min}$  point which is very important for the main applications of the model.

The PSO technique is widely used in optimizing different sorts of problems including fine materials, medical science, control theory, and energy issues [40–43]. The important facts which make PSO popular among the researchers are its fastness, its ability to avoid being trapped in the local optima, and its capability of being employed in any type of optimization problem [44–48]. Swarm intelligence techniques have several advantages that make them useful for optimization applications. Some of these advantages are scalability, flexibility, robustness, and low production costs. Scalability means particles can be added to the swarm without making any change in the overall behaviour of the colony. In other words,

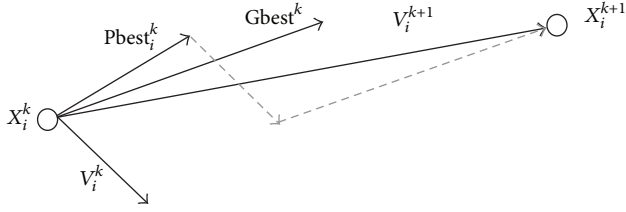


FIGURE 4: A simple diagram for movement of a sample particle in PSO.

individuals typically have a limited range of interaction with their neighborhood, so that the introduction of a new particle does not directly affect the whole swarm [49]. That helps to change the scale and size of the swarm easily, based on the size of the search space defined. Flexibility gives the ability to the swarm to be adapted to different problems under different circumstances. A well-designed swarm algorithm can exploit and explore an unknown territory, even encountering a huge gap in the search space. With regard to the robustness, if a few faulty individuals exist in the swarm, they may not affect the global optimum found by the swarm. The fourth main advantage is having low production costs. This is respective to the computational cost and memory size per unit of the individuals which gives the possibility of being used in small cheap components. The main advantage of the particle swarm optimization technique over other global optimization methods such as simulated annealing is having a large number of agents which makes the particle swarm technique resilient to the local optima points of the search space. In other words, it helps the algorithm in not being trapped in the local optima points.

**2.2. Particle Swarm Optimization (PSO).** The PSO algorithm is mainly based on the movement of a population of particles as a “Swarm.” This movement is inspired from a school of fish or a bird flock [50–52]. The evaluation of the search space is being performed step by step. There are some parameters which need to be saved at each step, since they will be needed in calculating the parameters of the next step. Equations (4) and (5) show the velocity and location of  $i$ th particle at  $k$ th step.

Consider

$$V_i^{k+1} = W \times V_i^k + c_1 \times r_1 (Gbest_i^k - X_i^k) \quad (5)$$

$$+ c_2 \times r_2 (Pbest_i^k - X_i^k),$$

$$X_i^{k+1} = X_i^k + V_i^k, \quad (6)$$

$i = 1, 2, \dots, \text{nop}$  (number of particles);  $k = 1, 2, \dots, k_{\max}$  (maximum iteration number), where,  $K$  is the iteration number;  $i$  is the particle number;  $W$  refers to the inertia weight coefficient which is normally chosen between 0.5 and 1.2;  $c_1$  and  $c_2$  are acceleration constants;  $r_1$  and  $r_2$  are random values between 0 and 1;  $V_i^k$  is the velocity of particle  $i$  at iteration  $k$ ; and  $X_i^k$  indicates the position of particle  $i$  at iteration  $k$ .

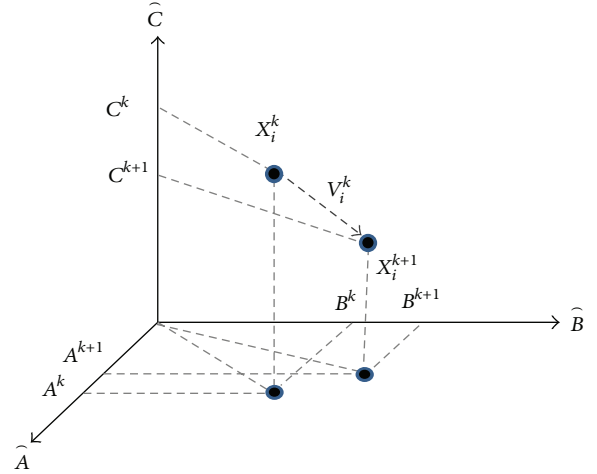


FIGURE 5: The search space of the problem.

Besides the above parameters which should be calculated for each particle, there are some social parameters that lead the swarm to the region which contains the global optima. “Personal best” and “Global best” are two parameters which are being used in all the PSO versions. They are normally shown as “Pbest” and “Gbest,” respectively. The Pbest is known as the best location that each particle experienced so far during the runtime, and the Gbest is the best global optimum found so far by the swarm. Figure 4 shows a simple diagram of movement of a typical particle.

### 3. Implementing Particle Swarm Optimization in DNA Sensor

**3.1. Representation of the Search Space.** Swarm is the particles which are moving and giving solutions for solving the problem. The particles move in the domain of the problem space and each of them represents a solution for the problem. The parameters to be optimized in the DNA sensor model are  $A$ ,  $B$ , and  $C$  coefficients as in (2). Figure 5 illustrates a three-dimensional search space of the problem. If  $\hat{A}$ ,  $\hat{B}$ , and  $\hat{C}$  are the vectors which return  $A$ ,  $B$ , and  $C$ , respectively, then particle  $i$  flies in the search space to find the best possible values for the respective parameters. Vector  $V_i$  is the movement velocity vector of the particle  $i$  which is obtained from (4).

In the optimization process, each location represented by the particles is a possible solution. The search space consists of arrays and matrices. For example,  $X[i][j]$  is a matrix of the location of the particles in the proposed algorithm, while  $i$  indicates the particle and  $j$  is the index of the optimizing parameter. In Figure 5, the dimension of the  $X[i][j]$  matrix will be  $200 \times 3$ , if we consider the number of particles to be equal to 200.

**3.2. Fitness Function and Parameter Selection.** To evaluate the solutions proposed by the particles, we need to define a fitness function. The fitness function has to be able to

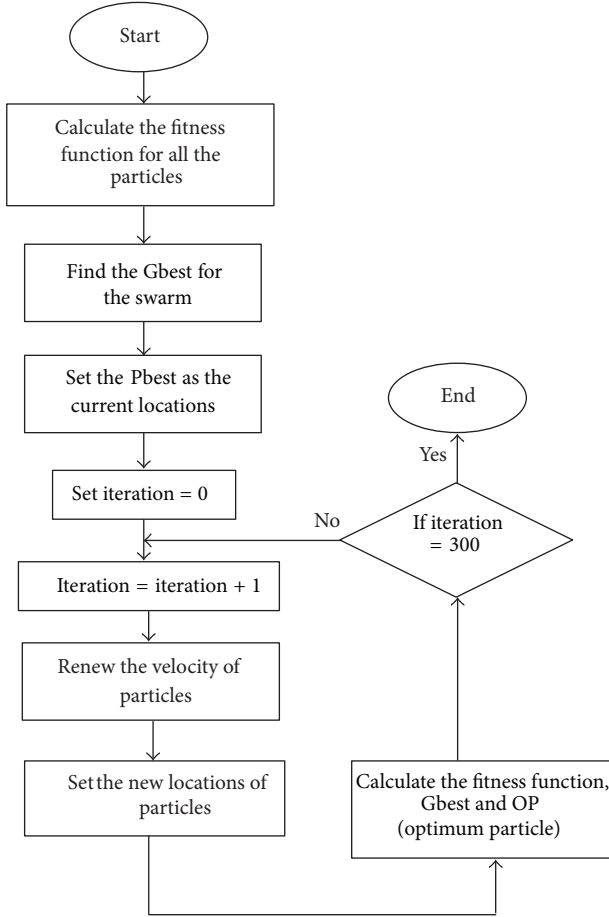


FIGURE 6: A flowchart of PSO-based algorithm for optimizing the DNA sensor.

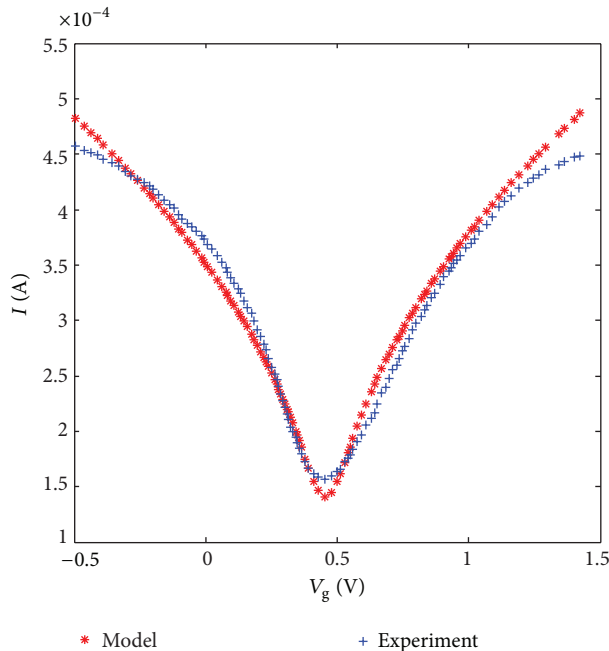


FIGURE 7: The experimental and optimized model waveforms for the bare DNA sensor.

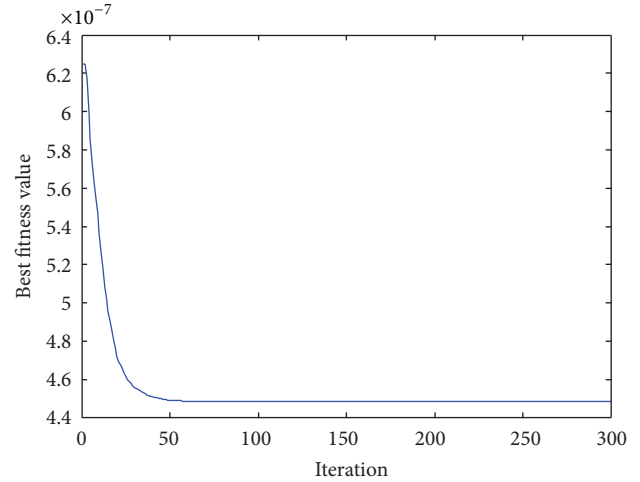


FIGURE 8: The convergence profile of the optimization process using PSO technique.

determine which solution is better and more efficient after considering all the solutions obtained by the particles at each iteration. Normally the fitness function is being set to have the lowest possible value at an optimum point. In the current study, we also need to have the lowest possible value of the error between the experimental waveform and the proposed model; hence, the fitness function is proposed as follows:

$$\text{Fitness function} = \psi_i = \sum_{k=1}^{\max} \left( \widehat{I}_i(k) - I(k) \right)^2, \quad (7)$$

where  $\widehat{I}_i(k)$  represents the modelled current waveform for particle  $i$ ,  $I(k)$  is the experimental current of the DNA sensor, and  $\psi_i$  is the fitness value of the  $i$ th particle. Based on the fitness function chosen, the best solution will propose the most fitted curve for the current waveform which is desired for a suitable DNA sensor model. The parameters of the PSO algorithm are chosen based on the values tabulated in Table 1, and the strategy of the optimization is shown in a flowchart as in Figure 6.

**3.3. Optimization Results for DNA Sensor Model.** After the optimization process, the best values obtained for the parameters  $A$ ,  $B$ , and  $C$  are tabulated in Table 2. These values are the best among the 20 runs of the optimization algorithm, and the lowest fitness value is the indicator of choosing the best parameters. The lowest obtained fitness value is also shown in the table which determines how good the modelled waveform fits the experimental curve.

The train for the optimizing parameters is performed using the experimental curve of the bare DNA sensor. Figure 7 illustrates the experimental waveform and the optimized model of the probe DNA sensor.

To show the convergence quality of the optimization process using PSO technique, the convergence profile of the best fitness value is shown in Figure 8 which is based on the fitness value versus iteration. The graph shows that the algorithm could converge to the optimized values after

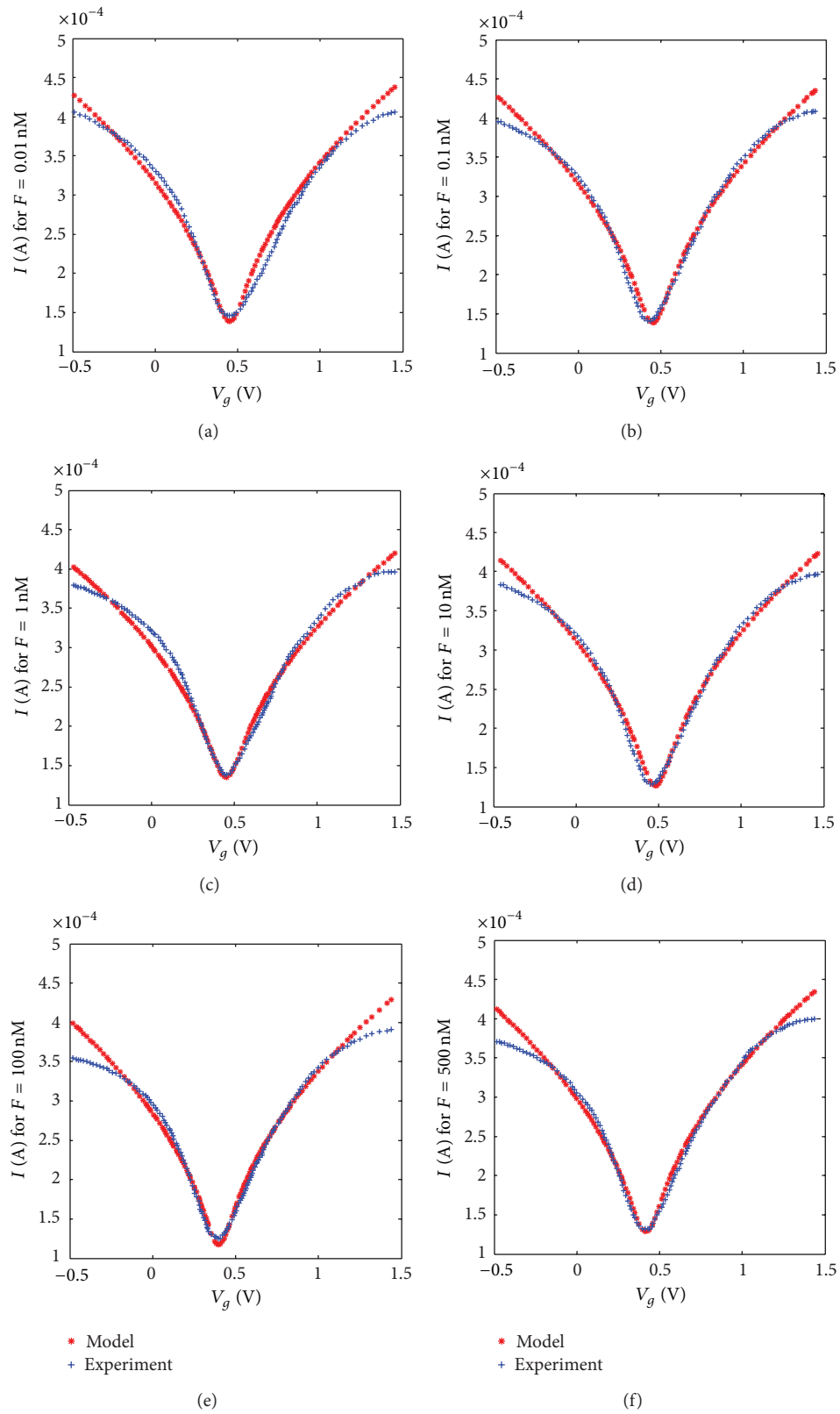


FIGURE 9: The optimized model and experimental waveforms for different concentrations of the DNA sensor: (a)  $F = 0.01$  nM, (b)  $F = 0.1$  nM, (c)  $F = 1$  nM, (d)  $F = 10$  nM, (e)  $F = 100$  nM, and (f)  $F = 500$  nM.

TABLE 1: The parameters chosen for the PSO algorithm.

Number of particles (nop)	Number of dimensions (nod)	$c1$	$c2$	Maximum iteration	Inertia weight ( $W$ )
200	3	2	2	300	$0.4 < W < 1.2$

TABLE 2: The best values of the optimizing parameters over the 20 runs.

The best fitness value obtained	Optimized value for $A$	Optimized value for $B$	Optimized value for $C$
$4.484e - 07$	$1.0865e10$	$9.9662e9$	$-5.921e3$

TABLE 3: The MAPE value with respect to the different concentrations ( $F$ ).

Concentration $F$ (nM)	MAPE value (%)	Accuracy based on MAPE (%)
$F = 0.01$	4.58	95.42
$F = 0.1$	3.52	96.48
$F = 1$	3.33	96.67
$F = 10$	3.39	96.61
$F = 100$	3.52	96.48
$F = 500$	3.94	96.06

around 60 iterations which show a good convergence speed of the proposed method.

Using the values obtained for  $A$ ,  $B$ , and  $C$  parameters, different concentrations of the DNA sensor are modelled and compared with the experimental waveforms with the same concentrations. To evaluate the quality of the obtained waveforms with respect to the experimental results, mean absolute percentage error (MAPE) index is used as an error evaluation parameter as follows:

$$\text{MAPE} = \frac{1}{n} \sum_{k=1}^n \left| \frac{\widehat{I}(k) - I(k)}{I(k)} \right|. \quad (8)$$

The results based on the MAPE index for different concentrations of the DNA sensor are shown in Table 3. The accuracy based on the MAPE value can be obtained as the result of deducting MAPE from 100 percent. Based on the results in the table, the accuracy of the optimized model is more than 95% for all the concentrations which is an acceptable range of accuracy.

Also, the optimized waveforms for different concentrations are seen in Figure 9, where for each concentration the optimized model and experimental waveforms are plotted. It needs to be mentioned that the middle part of the graph is very important, since the voltage used in the experiment is normally between 0 and 1 volts. The optimized model fits even better around the mentioned voltage range.

It needs to be mentioned that the  $V_{g,\min}$  (minimum gate voltage) is a very sensitive indicator for detection of DNA molecules and the optimized model shows a better performance around the (0 and 1 volt) voltage range.

## 4. Conclusion

Due to the unique characteristics of the graphene such as special C–C bonding, 1D structure, large surface-to-volume ratio, high conductivity, and biocompatibility, it has remarkable potential for biosensing material applications. The graphene-based DNA sensor has a similar structure to traditional metal-oxide-semiconductor FET (MOSFET) in which the gate is exposed to the electrolyte solution containing DNA molecules. In these sensors, DNA adsorption occurring on a graphene surface changes the  $I$ - $V$  characteristics of the transistors due to the intrinsic negative charge of DNA. In this research, DNA sensing factor which was presented in our previous work is optimized using particle swarm optimization (PSO) technique. The optimization process is performed in order to find the optimized values of fitting parameters in a current-voltage characteristic of DNA sensor model to predict graphene doping behavior in GFET devices. Based on the results obtained, an accuracy of more than 95% is obtained for the optimized model compared with the available experimental data. It can be concluded that the optimized graphene-based DNA sensor model with the accuracy obtained is now suitable and reliable for being employed in different applications such as diagnosis of genetic and pathogenic diseases.

## Acknowledgments

The authors would like to acknowledge the financial support from the Research University Grant of the Ministry of Higher Education of Malaysia (MOHE) under Project Grant: FRGS-4F149. Also, thanks to the Research Management Center (RMC) of Universiti Teknologi Malaysia (UTM) for providing an excellent research environment in which to complete this work.

## References

- [1] J. L. Su, B.-S. Youn, W. P. Ji, J. H. Niazi, S. K. Yeon, and B. G. Man, "ssDNA aptamer-based surface plasmon resonance biosensor for the detection of retinol binding protein 4 for the early diagnosis of type 2 diabetes," *Analytical Chemistry*, vol. 80, no. 8, pp. 2867–2873, 2008.
- [2] A.-L. Liu, G.-X. Zhong, J.-Y. Chen et al., "A sandwich-type DNA biosensor based on electrochemical co-reduction synthesis of graphene-three dimensional nanostructure gold nanocomposite films," *Analytica Chimica Acta*, vol. 767, pp. 50–58, 2013.
- [3] X. Dong, Y. Shi, W. Huang, P. Chen, and L.-J. Li, "Electrical detection of DNA hybridization with single-base specificity

- using transistors based on CVD-grown graphene sheets,” *Advanced Materials*, vol. 22, no. 14, pp. 1649–1653, 2010.
- [4] Y. Cui, Q. Wei, H. Park, and C. M. Lieber, “Nanowire nanosensors for highly sensitive and selective detection of biological and chemical species,” *Science*, vol. 293, no. 5533, pp. 1289–1292, 2001.
  - [5] P. R. Nair and M. A. Alam, “Performance limits of nanobiosensors,” *Applied Physics Letters*, vol. 88, no. 23, Article ID 233120, 2006.
  - [6] V. Singh, D. Joung, L. Zhai, S. Das, S. I. Khondaker, and S. Seal, “Graphene based materials: past, present and future,” *Progress in Materials Science*, vol. 56, no. 8, pp. 1178–1271, 2011.
  - [7] Y. Shao, J. Wang, H. Wu, J. Liu, I. A. Aksay, and Y. Lin, “Graphene based electrochemical sensors and biosensors: a review,” *Electroanalysis*, vol. 22, no. 10, pp. 1027–1036, 2010.
  - [8] N. Mohanty and V. Berry, “Graphene-based single-bacterium resolution biodevice and DNA transistor: interfacing graphene derivatives with nanoscale and microscale biocomponents,” *Nano Letters*, vol. 8, no. 12, pp. 4469–4476, 2008.
  - [9] X. Dong, X. Zhao, L. Wang, and W. Huang, “Synthesis and application of graphene nanoribbons,” *Current Physical Chemistry*, vol. 3, no. 3, pp. 291–301, 2013.
  - [10] F. Chen, Q. Qing, J. Xia, and N. Tao, “Graphene field-effect transistors: electrochemical gating, interfacial capacitance, and biosensing applications,” *Chemistry*, vol. 5, no. 10, pp. 2144–2153, 2010.
  - [11] M. Zheng, A. Jagota, E. D. Semke et al., “DNA-assisted dispersion and separation of carbon nanotubes,” *Nature Materials*, vol. 2, no. 5, pp. 338–342, 2003.
  - [12] E. Souteyrand, J. P. Cloarec, J. R. Martin et al., “Direct detection of the hybridization of synthetic homo-oligomer DNA sequences by field effect,” *Journal of Physical Chemistry B*, vol. 101, no. 15, pp. 2980–2985, 1997.
  - [13] J. Fritz, E. B. Cooper, S. Gaudet, P. K. Sorger, and S. R. Manalis, “Electronic detection of DNA by its intrinsic molecular charge,” *Proceedings of the National Academy of Sciences of the United States of America*, vol. 99, no. 22, pp. 14142–14146, 2002.
  - [14] F. Wei, B. Sun, Y. Guo, and X. S. Zhao, “Monitoring DNA hybridization on alkyl modified silicon surface through capacitance measurement,” *Biosensors and Bioelectronics*, vol. 18, no. 9, pp. 1157–1163, 2003.
  - [15] M. H. Abouzar, A. Poghossian, A. G. Cherstvy, A. M. Pedraza, S. Ingebrandt, and M. J. Schoening, “Label-free electrical detection of DNA by means of field-effect nanoplate capacitors: experiments and modeling,” *Physica Status Solidi A*, vol. 209, no. 5, pp. 925–934, 2012.
  - [16] D.-S. Kim, Y.-T. Jeong, H.-J. Park et al., “An FET-type charge sensor for highly sensitive detection of DNA sequence,” *Biosensors and Bioelectronics*, vol. 20, no. 1, pp. 69–74, 2004.
  - [17] D.-S. Kim, H.-J. Park, H.-M. Jung et al., “Field effect transistor-based bimolecular sensor employing a Pt reference electrode for the detection of deoxyribonucleic acid sequence,” *Japanese Journal of Applied Physics*, vol. 43, no. 6, pp. 3855–3859, 2004.
  - [18] F. Uslu, S. Ingebrandt, D. Mayer, S. Böcker-Meffert, M. Odenthal, and A. Offenhäuser, “Label-free fully electronic nucleic acid detection system based on a field-effect transistor device,” *Biosensors and Bioelectronics*, vol. 19, no. 12, pp. 1723–1731, 2004.
  - [19] F. Yan, M. Zhang, and J. Li, “Solution-gated graphene transistors for chemical and biological sensors,” *Advanced Healthcare Materials*, 2013.
  - [20] H. Berney, J. West, E. Haefele, J. Alderman, W. Lane, and J. K. Collins, “DNA diagnostic biosensor: development, characterization and performance,” *Sensors and Actuators B*, vol. 68, no. 1, pp. 100–108, 2000.
  - [21] F. Pouthas, C. Gentil, D. Côte, and U. Bockelmann, “DNA detection on transistor arrays following mutation-specific enzymatic amplification,” *Applied Physics Letters*, vol. 84, no. 9, pp. 1594–1596, 2004.
  - [22] L. Gu, J. Han, H. Zhang, and X. Chen, “DNA field effect transistor,” in *Proceedings of the International Conference on Sensor Technology (ISTC '01)*, pp. 47–49, International Society for Optics and Photonics, October 2001.
  - [23] A. Sassolas, B. D. Leca-Bouvier, and L. J. Blum, “DNA biosensors and microarrays,” *Chemical Reviews*, vol. 108, no. 1, pp. 109–139, 2008.
  - [24] T. G. Drummond, M. G. Hill, and J. K. Barton, “Electrochemical DNA sensors,” *Nature Biotechnology*, vol. 21, no. 10, pp. 1192–1199, 2003.
  - [25] F. Schwierz, “Graphene transistors,” *Nature Nanotechnology*, vol. 5, no. 7, pp. 487–496, 2010.
  - [26] A. K. Geim and A. H. MacDonald, “Graphene: exploring carbon flatland,” *Physics Today*, vol. 60, no. 8, pp. 35–41, 2007.
  - [27] A. K. Geim and K. S. Novoselov, “The rise of graphene,” *Nature Materials*, vol. 6, no. 3, pp. 183–191, 2007.
  - [28] T. Kurkina, A. Vlandas, A. Ahmad, K. Kern, and K. Balasubramanian, “Label-free detection of few copies of DNA with carbon nanotube impedance biosensors,” *Angewandte Chemie International Edition*, vol. 50, no. 16, pp. 3710–3714, 2011.
  - [29] I. Heller, A. M. Janssens, J. Männik, E. D. Minot, S. G. Lemay, and C. Dekker, “Identifying the mechanism of biosensing with carbon nanotube transistors,” *Nano Letters*, vol. 8, no. 2, pp. 591–595, 2008.
  - [30] F. Karimi, M. Ahmadi, M. Rahmani, E. Akbari, M. J. Kiani, and M. Khalid, “Analytical modeling of graphene-based DNA sensor,” *Science of Advanced Materials*, vol. 4, no. 11, pp. 1142–1147, 2012.
  - [31] I. Heller, S. Chatoor, J. Männik, M. A. G. Zevenbergen, C. Dekker, and S. G. Lemay, “Influence of electrolyte composition on liquid-gated carbon nanotube and graphene transistors,” *Journal of the American Chemical Society*, vol. 132, no. 48, pp. 17149–17156, 2010.
  - [32] J. Klimeš and A. Michaelides, “Perspective: advances and challenges in treating van der Waals dispersion forces in density functional theory,” *The Journal of Chemical Physics*, vol. 137, Article ID 120901, 12 pages, 2012.
  - [33] A. Poghossian, A. Cherstvy, S. Ingebrandt, A. Offenhäuser, and M. J. Schöning, “Possibilities and limitations of label-free detection of DNA hybridization with field-effect-based devices,” *Sensors and Actuators B*, vol. 111–112, pp. 470–480, 2005.
  - [34] H. K. F. Abadi, R. Yusof, S. M. Eshrati et al., “Current—voltage modeling of graphene-based DNA sensor,” *Neural Computing and Applications*, 2013.
  - [35] M. J. Kiani, M. T. Ahmadi, H. K. F. Abadi, M. Rahmani, and A. Hashim, “Analytical modelling of monolayer graphene-based ion-sensitive FET to pH changes,” *Nanoscale Research Letters*, vol. 8, no. 1, pp. 1–9, 2013.
  - [36] S. Datta, *Electronic Transport in Mesoscopic Systems*, Cambridge University Press, Cambridge, UK, 2002.
  - [37] D. S. L. Abergel, V. Apalkov, J. Berashevich, K. Ziegler, and T. Chakraborty, “Properties of graphene: a theoretical perspective,” *Advances in Physics*, vol. 59, no. 4, pp. 261–482, 2010.

- [38] A. F. Ávila, A. S. Neto, and H. Nascimento Junior, "Hybrid nanocomposites for mid-range ballistic protection," *International Journal of Impact Engineering*, vol. 38, no. 8-9, pp. 669–675, 2011.
- [39] M. T. Ahmadi, Z. Johari, N. A. Amin, A. H. Fallahpour, and R. Ismail, "Graphene nanoribbon conductance model in parabolic band structure," *Journal of Nanomaterials*, vol. 2010, Article ID 753738, 4 pages, 2010.
- [40] B. Huang, N. Tai, and W. Huang, "Optimization and coordination of HAFDV PINN control by improved PSO," *Journal of Control Science and Engineering*, vol. 2013, Article ID 872624, 7 pages, 2013.
- [41] W. He, Y. Cheng, L. Xia, and F. Liu, "A new particle swarm optimization-based method for phase unwrapping of MRI data," *Computational and Mathematical Methods in Medicine*, vol. 2012, Article ID 475745, 9 pages, 2012.
- [42] R. Rahmani, A. Khairuddin, S. M. Cherati, and H. A. Mahmoud Pesaran, "A novel method for optimal placing wind turbines in a wind farm using Particle Swarm Optimization (PSO)," in *Proceedings of the 9th International Power and Energy Conference (IPEC '10)*, pp. 134–139, October 2010.
- [43] R. Rahmani, M. F. Othman, R. Yusof, and M. Khalid, "Solving economic dispatch problem using particle swarm optimization by an evolutionary technique for initializing particles," *Journal of Theoretical and Applied Information Technology*, vol. 46, no. 2, pp. 526–536, 2012.
- [44] J. Lv, Y. Wang, L. Zhu, and Y. Ma, "Particle-swarm structure prediction on clusters," *The Journal of Chemical Physics*, vol. 137, Article ID 084104, 2012.
- [45] S. Das, A. Abraham, and A. Konar, "Particle swarm optimization and differential evolution algorithms: technical analysis, applications and hybridization perspectives," in *Advances of Computational Intelligence in Industrial Systems*, vol. 116 of *Studies in Computational Intelligence*, pp. 1–38, Springer, Berlin, Germany, 2008.
- [46] D. W. Boeringer and D. H. Werner, "Particle swarm optimization versus genetic algorithms for phased array synthesis," *IEEE Transactions on Antennas and Propagation*, vol. 52, no. 3, pp. 771–779, 2004.
- [47] M. Clerc, *Particle Swarm Optimization*, Wiley-ISTE, 2006.
- [48] R. C. Eberhart and Y. Shi, "Particle swarm optimization: developments, applications and resources," in *Proceedings of the Congress on Evolutionary Computation*, pp. 81–86, May 2001.
- [49] Y. Wang, J. Lv, L. Zhu, and Y. Ma, "Crystal structure prediction via particle-swarm optimization," *Physical Review B*, vol. 82, no. 9, Article ID 094116, 2010.
- [50] R. C. Eberhart, Y. Shi, and J. Kennedy, *Swarm Intelligence*, Elsevier, Indianapolis, Ind, USA, 2001.
- [51] R. Poli, J. Kennedy, and T. Blackwell, "Particle swarm optimization," *Swarm Intelligence*, vol. 1, no. 1, pp. 33–57, 2007.
- [52] Y. del Valle, G. K. Venayagamoorthy, S. Mohagheghi, J.-C. Hernandez, and R. G. Harley, "Particle swarm optimization: basic concepts, variants and applications in power systems," *IEEE Transactions on Evolutionary Computation*, vol. 12, no. 2, pp. 171–195, 2008.

## Research Article

# Influence of Electric Field Coupling Model on the Simulated Performances of a GaN Based Planar Nanodevice

K. Y. Xu,<sup>1</sup> Z. N. Wang,<sup>1</sup> Y. N. Wang,<sup>1</sup> J. W. Xiong,<sup>1</sup> and G. Wang<sup>2</sup>

<sup>1</sup>Laboratory of Quantum Engineering and Quantum Materials, School of Physics and Telecommunication Engineering, South China Normal University, Guangzhou 510006, China

<sup>2</sup>State Key Laboratory of Optoelectronic Materials and Technologies, Sun Yat-sen University, Guangzhou 510275, China

Correspondence should be addressed to K. Y. Xu; xuky@scnu.edu.cn

Received 18 October 2013; Revised 18 December 2013; Accepted 19 December 2013

Academic Editor: Razali Ismail

Copyright © 2013 K. Y. Xu et al. This is an open access article distributed under the Creative Commons Attribution License, which permits unrestricted use, distribution, and reproduction in any medium, provided the original work is properly cited.

The performances of a two-dimensional electron gas (2DEG) based planar nanodevice are studied by a two-dimensional-three-dimensional (2D-3D) combined model and an entirely 2D model. In both models, 2DEGs are depicted by 2D ensemble Monte Carlo (EMC) method. However electric field distributions in the devices are obtained by self-consistently solving 2D and 3D Poisson equations for the 2D model and the 2D-3D model, respectively. Simulation results obtained by both models are almost the same at low bias while showing distinguished differences at high bias. The 2D model predicts larger output current and slightly higher threshold voltage of Gunn oscillations. Although the fundamental frequencies of current oscillations obtained by both models are similar, the deviation of wave shape from sinusoidal waveform obtained by the 2D model is more serious than that obtained by 2D-3D model. Moreover, results obtained by the 2D model are more sensitive both to the bias conditions and to the change of device parameters. Interestingly, a look-like second harmonic oscillation has been observed at DC bias. We contribute the origin of divergences in simulation results to the different coupling path of electric field in the two models. And the second-harmonic oscillations at DC bias should be the result of the appearance of concomitant oscillations beside the channel excited by strong electric-field effects.

## 1. Introduction

Continuous miniaturization of semiconductor devices has led to high-speed operations and large-scale integrations of electronics in the past decades. A single silicon chip is now able to contain more than a billion transistors and operate at frequencies higher than GHz. Benefitting from the utilization of planar architecture the operation frequency can be further increased. In planar devices, electrodes are connected side by side to the active semiconductor layer rather than being placed on top of each other, as in conventional multilayered vertical-structured devices. As a result, very low parasitic capacitances are obtainable, leading to a very high operating speed. Planar nanodevices based on 2DEGs in semiconductor heterostructures have been demonstrated to operate at tens of GHz or above [1–4]. In particular, self-switching diodes (SSDs) have been shown to possess zero threshold voltages and be able to detect electromagnetic signals with speed up

to 110 GHz and up to 2.5 THz at room temperature and at a temperature of 150 K, respectively [3, 5].

Apart from the experiments on planar nanodevices, there have been theoretical efforts based on analytical models or advanced numerical models, such as MC models, to further understand the device operations [6–8]. In MC models, electrons transporting in 2DEG layer is usually depicted by 2D EMC methods, and the electric field distributions are obtain by self-consistently solving 2D Poisson equations. This entirely 2D model not only obtains good agreements with experiments, but also predicts additional features of the planar devices, such as very low noise spectra in the THz range and enhanced THz detections by plasma [9–11]. However, the entirely 2D EMC models are unable to directly deal with electric field coupling beyond the 2DEG layer. To overcome this, a 2D-3D combined EMC model and a fully 3D EMC model have been developed, respectively. The previous model has been used to study the effects of electric

field coupling through the substrate and the nearby dielectric layers on the performances of a side-gated transistor [12]. The later model has been applied to study three-terminal T-branch junctions (TBJs) with a top gate terminal, which is modeled as a side gate in entirely 2D models [13–15]. It is noteworthy that in spite of minimizing the need for parameter fitting and including the effect of electron transfer from channel to other layers, the 3D model leads to almost the same results as those obtained from 2D model for GaAs based devices [16]. However, in order to overcome huge time consuming, the EMC domain of 3D simulation should be limited to a small region.

In this work, efforts are devoted to study the influence of electric field coupling model on the simulation results of GaN based planar nanodevices. Unlike the GaAs based devices, the GaN based devices have much higher working voltage. This should lead to higher sensitivity of the device performances to the electric field coupling in the devices. As such, an entirely 2D EMC model and a 2D-3D combined EMC model are applied here and more attention will be paid to the phenomenon of Gunn oscillations that occur under high-field condition. The particular devices we focus on are SSDs, since they are not only based on electric field coupling but benefit for the propagation of Gunn domains [17]. The paper is structured as follows. In Section 2, the structure and working principle of the SSDs are firstly introduced and then the entirely 2D EMC model and the 2D-3D combined EMC model are concisely described, respectively. In Section 3, the performances of SSDs with different parameters are studied by both models under various conditions and results are analyzed in detail. In Section 4, the conclusions of this work are summarized.

## 2. Device Working Principle and Numerical Models

Figures 1(a) and 1(b) show schematically the top view and cross-section of a SSD. The device is based on a GaN/AlGaIn heterostructure, where a 2DEG is formed at the GaN-AlGaIn heterointerface with a carrier concentration of  $8.0 \times 10^{12} \text{ cm}^{-2}$  [18]. The two L-shaped insulating trenches are created by etching, through the 2DEG layer, ensuring that electrons have to pass the narrow channel between the two trenches in order to conduct a current between the left and right terminals. When a positive voltage is applied to the right terminal, positive charge is induced around the trenches, because of field effect, attracting electrons into the channel for the current to flow easily. However, when a negative voltage is applied to the right terminal, the negative charge around the trenches results in depletion of the channel, thus inhibiting the current flow, forming diode-like characteristics, as demonstrated by Song et al. [19].

The entirely 2D model is based on a semiclassical EMC method self-consistently coupled with Poisson equations [20]. As in earlier work, some theoretical assumptions are made in order to enhance the efficiency of the EMC simulations [11, 21, 22]. Firstly, 2D EMC simulations are performed only on the active GaN layer, since it is the 2DEG layer that

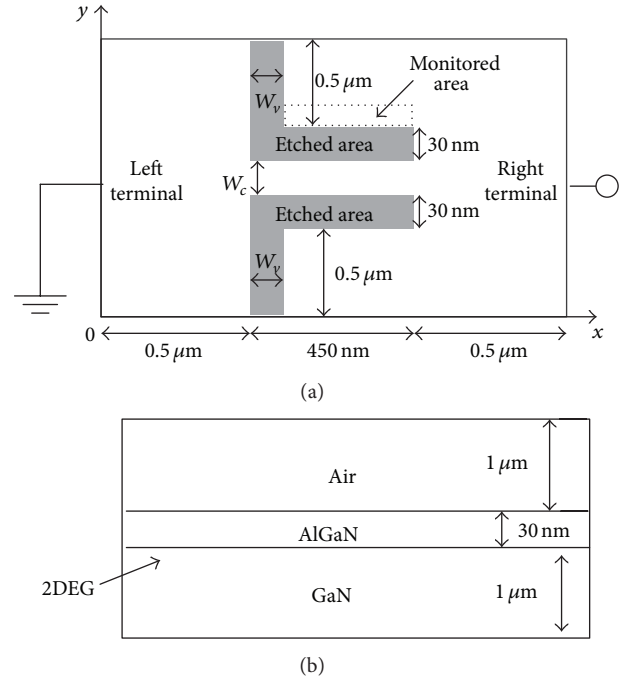


FIGURE 1: Schematic top view (a) and side view (b) of the simulated SSD (not to scale). The gray areas and the white area in the top view represent insulating trenches and 2DEG, respectively. An interface of GaN/AlGaIn heterostructures in (b) is just 30 nm below the device surface, at which a sheet of 2DEG forms. During simulations, all the insulating trenches are assumed to have vertical sidewalls and pass through both the entire AlGaIn layer and the entire GaN one.

largely determines the electronic properties of the device. Secondly, to account for the fixed positive charges of the doping layer, a virtual net background doping  $N_V = 8.0 \times 10^{17} \text{ cm}^{-3}$  (without ionized impurity scattering) is assigned to the GaN layer. In order to model the influence of surface states at semiconductor-air interface a uniform negative charge density,  $N_S = 0.8 \times 10^{12} \text{ cm}^{-2}$ , is also added at the edge of the insulating trenches during the simulations. Since the charge density is constant during the whole simulation process, this treatment is called constant charge (CC) model [18]. The SSD was designed with a channel length of  $L_c = 450 \text{ nm}$  and a horizontal trench width of  $W_h = 30 \text{ nm}$ . Other geometric parameters are defined in Figure 1(a). All simulations are carried out at room temperature, with the left terminal grounded. And the Poisson equations are solved in  $5 \text{ nm} \times 5 \text{ nm}$  meshes with a time step of 1 fs. More information about the model can be found in [21].

The 2D-3D combined EMC model is developed from the previous entirely 2D model. The 2D-3D model is also based on a semi-classical 2D EMC method but self-consistently coupled with 3D Poisson equations. In this model, we assume that electrons are all confined within the 2DEG layer, ignoring the effect of electron transfer from channel to other layers, so that 2D EMC method is enough to depict the micro behaviors of the electrons in the devices. When solving the Poisson equations, the charge related to the 2DEG is considered as

a surface charge involved in a Neumann boundary condition. It has been shown in [12] that the 3D electric field coupling occurs in an effective distance of about 400 nm away from the 2DEG. As the distance between 2DEG and the device surface (top of the AlGa<sub>N</sub> layer) is only 30 nm, the Poisson equations should be solved in a domain beyond the geometry of the devices. As shown in Figure 1(b), the GaN substrate and a region (Air) above the device surface, both with height of 1  $\mu\text{m}$ , are included. In principle, the insulating trenches of the devices are only required to pass through the 2DEG. However, previous study showed that when the trench depth had nonnegligible influences on the device performances [12]. To avoid the influences coming from the variations of trench depth, all the trenches are assumed to have vertical sidewalls and pass through the whole GaN/AlGa<sub>N</sub> heterostructures from the device surface to the bottom of the substrate, which is with depth of 1030 nm. Since the transfers of electrons along the  $z$  direction are ignored, there should be no physical restrictions on the size of meshes [21]. As such and for reducing the computational effort, nonuniform meshes are utilized in the  $z$  direction. Beginning from the 2DEG, with initial value of 1 nm, both to the top of the simulated Air and to the bottom of the simulated substrate, the increase of mesh size obeys a special geometric progression. The common ratio used for the geometric progression changes from 2 to 1.5 and then to 1 when the size of the meshes is larger than 10 nm and 100 nm, respectively. Dielectric constant used in the simulations for Air, AlGa<sub>N</sub>, and GaN is 1, 8.5, and 8.9, respectively. Other treatments are the same as the entirely 2D EMC model. Details of the above 2D-3D combined model can be found in our recent work [12].

### 3. Simulation Results and Analysis

Figure 2 shows the time-dependent output current of the SSD shown in Figure 1. During simulations, we set channel width of  $W_c = 30$  nm and vertical trench width of  $W_v = 30$  nm, respectively. Other simulation parameters can be found in Figure 1. To further study this, we calculated the device current at different bias voltage steps, from 0 to 3.5 V at increments of 0.5 V, for SSDs with different vertical trench widths and different channel widths. Then the right terminal of the SSD is biased to voltage steps from 4 to 24 V on an increase of 2 V for every 10 ps. Red solid line and green dashed line in Figure 2 represent simulation results obtained by the 2D model and the 2D-3D model, respectively. For both results, current peaks with sharp rise and fall can be found after each abrupt change of the applied voltage, which are anticipated as results of the charging of parasitic capacitances in the devices [17]. Apart from the above current peaks, simulation results obtained by both models are almost the same at bias lower than 4 V. And when the bias is beyond 4 V, output current obtained by the 2D model is higher than that obtained by 2D-3D model. However, the threshold voltages of Gunn oscillations are similar, 18 V by the 2D model and 16 V by the 2D-3D model. Since the length of the channel is 450 nm, the threshold electric field for Gunn

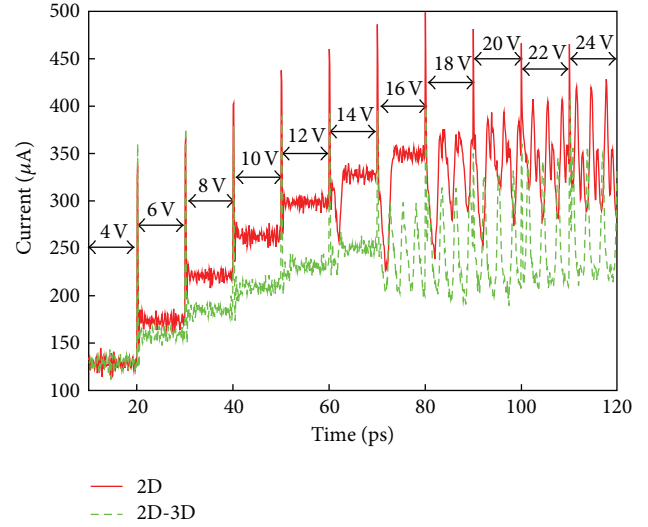


FIGURE 2: Output current of a SSD with channel width of  $W_c = 30$  nm and horizontal trench width of  $W_v = 30$  nm, when a series of time-dependent step voltages are applied at the right terminal. Red solid line is obtained using 2D model and green dashed line using 2D-3D combined model.

oscillations would be about 0.4 MV/cm, which agrees with recent experimental results [23].

One can also find that the period of the oscillations at 18 V obtained by both models is about 3 ps, corresponding to a frequency of about 0.3 THz. However, the waveform of the oscillations obtained by the 2D-3D model is more sinusoidal than that by 2D model. This phenomenon becomes more obvious at higher bias, when a small additional peak emerges in every circle of oscillations obtained by the 2D model.

To understand the above bias-dependent divergence in simulation results, one should come back to the difference between the two models. As described in Section 2, in the 2D model, electric field couplings are well confined within the conducting layer (2DEG). However, in the 2D-3D model, part of electric field couples through the device substrate with longer path and through the Air with lower dielectric constant. As such, electric field couplings in the 2D-3D model are lower than those in the 2D model. Since SSDs are based on electric field effect [2, 8, 21], it is reasonable that the device performances obtained by the 2D model are more sensitive to the bias conditions. Moreover, unlike the electric field couplings within the device, those through the Air are seldom affected by the device structure, so that results obtained by 2D-3D model would be less sensitive to the change of device geometry. To confirm this, SSDs with different geometrical parameters should be further studied by both models.

According to the above simulation results, the two models present large differences at high bias especially when Gunn oscillation occurs. As such, we focus on studying the waveforms of oscillations at bias of 26 V. Shown in Figure 3 are the results for SSDs with different vertical trench width of  $W_v = 30$  nm (red curves), 50 nm (green curves), and 70 nm (blue curves) obtained by (a) the 2D model and (b) the 2D-3D model. Other needed parameters are the same as those used

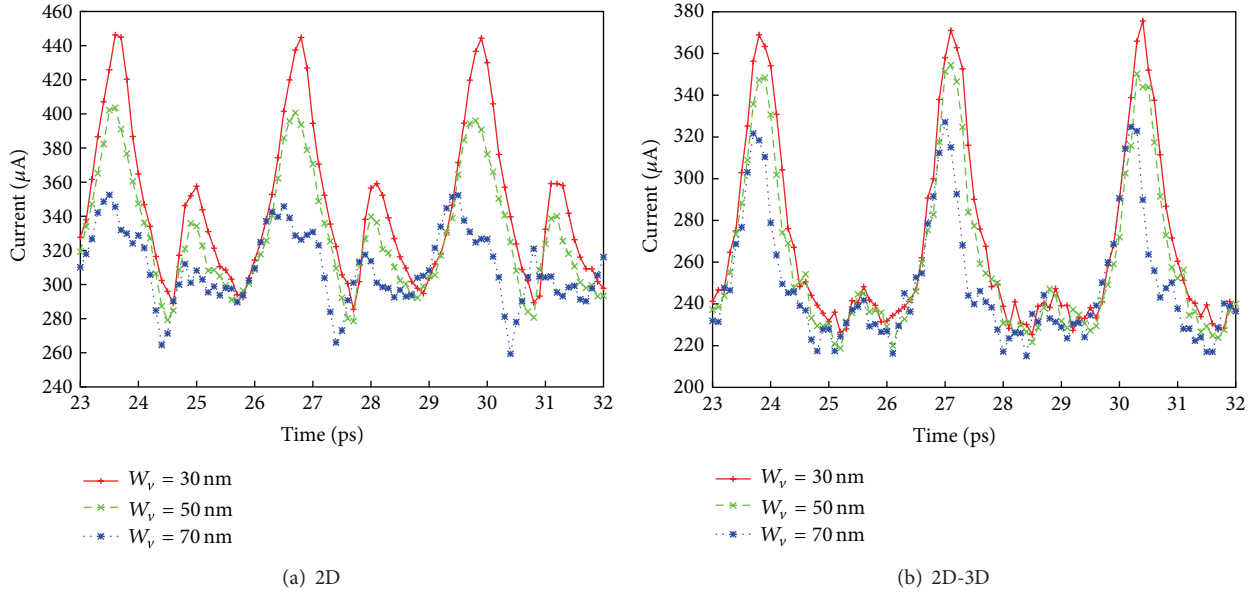


FIGURE 3: Waveforms of oscillations of SSDs with different vertical trench width of  $W_v = 30$  nm (red curves), 50 nm (green curves), and 70 nm (blue curves) at bias of 26 V obtained by (a) 2D model and (b) 2D-3D combined model (other simulation parameters are the same as those used in Figure 2).

in Figure 2. Comparing the results shown in Figure 3, one can find that the waveforms obtained by both models for narrow vertical trench, such as  $W_v = 30$  nm, show similar harmonic components, both with a small additional peak between two large major peaks. However, the amplitude of the additional peak obtained by the 2D-3D model is much lower than that obtained by the 2D model. Moreover, when the vertical trench width increases, the waveforms obtained by the 2D-3D model show just a small reduction in the amplitude. This reduction of the oscillation current is understandable. Since the vertical trench is widened, field effects applied on the channel are weakened [19]. As a result, the resistance of the channel increases, then the output current of the device reduces. In contrast, the waveforms obtained by the 2D model show not only a larger reduction in the amplitude, but also a nonnegligible change in the harmonic components, more additional peaks emerging.

In order to further reveal the divergences of simulation results obtained using different models, the influences of channel width on the waveforms of the oscillations have also been studied. Results are shown in Figure 4(a) using the 2D model and Figure 4(b) using the 2D-3D model. Simulation parameters are the same as those used in Figure 2, except that different channel widths with value of 50 nm (red curves), 60 nm (green curves), and 70 nm (blue curves) are chosen. One can find that additional peaks are also observed in Figure 4, which grow up with the increment of channel width. Once again, results obtained using the 2D model are more sensitive to channel width than those obtained using 2D-3D model. When the channel width is 70 nm, the additional peak obtained by the 2D-3D model is only as high as 30% of the major peak, while that obtained by the 2D model is almost as high as the major peak. Since the additional peak happens

to be in the middle of two nearby major peaks, the waveform looks like second harmonic (blue curve in Figure 4(a)) with frequency of about 0.6 THz.

It is noteworthy that similar phenomenon of second harmonic oscillations at DC bias was also observed in GaN based SSDs using an entirely 2D model [18]. In that work, based on a CC model to include the influence of surface states at semiconductor-air interface, the frequency of Gunn oscillations at DC bias had been proved to lie within the second generation band of oscillations taking place in the presence of an additional AC bias. Furthermore, a self-consistent charge (SCC) model proposed in [24] was also used to make a deeper study of the influences of surface charges on the performances of SSDs. Results obtained using such advanced charge model showed good agreements with experimental data under any bias condition. In the SCC model, the local value of the surface charge was dynamically adjusted depending on the surrounding carrier density resulting in an increase of surface charge density with bias, which suppressed Gunn oscillations in narrow channel devices. Similar suppressions of Gunn oscillations are also observed in our simulations when higher surface charge density is used (results not shown). Moreover, for wide channel devices results obtained based on SCC model exhibited qualitative dependencies and basic operation, including second harmonic oscillations at DC bias, as those obtained using CC model. For the authors who focused on the AC features of the SSDs, little attention was paid to understand the origin of second harmonic oscillations at DC bias.

It is known that for SSDs electrons surrounding the channel play an important role in the properties of electron transport in the channel. This is because the horizontal trenches used to define the channel are on the scale of

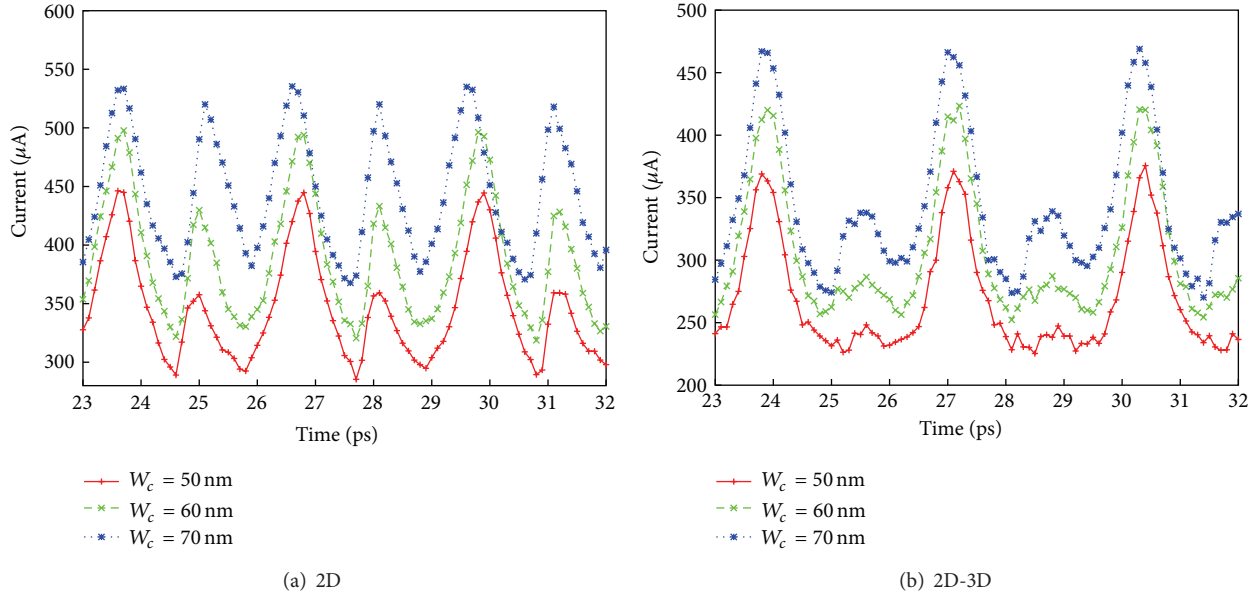


FIGURE 4: Waveforms of oscillations in the SSDs with different channel width of  $W_c = 50$  nm (red curves), 60 nm (green curves), and 70 nm (blue curves) at bias of 26 V obtained by (a) the 2D model and (b) the 2D-3D model (other simulation parameters are the same as those used in Figure 2).

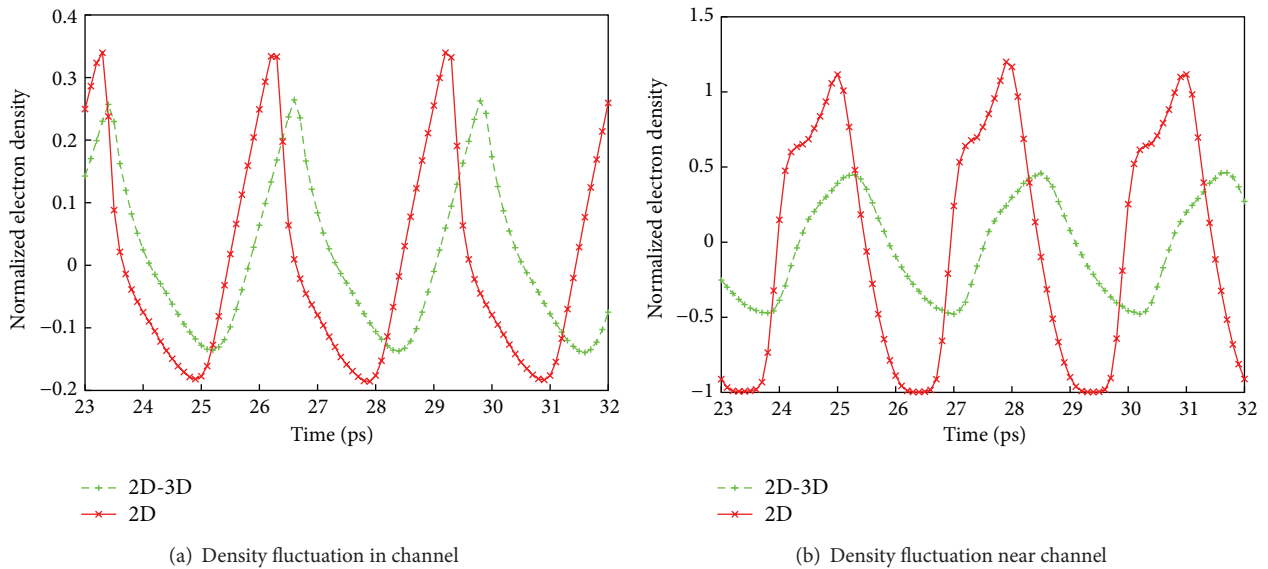


FIGURE 5: Normalized electron density fluctuations with time (a) in the channel and (b) near the channel (i.e., in the monitored area shown in Figure 1(a)) at bias of 26 V obtained by the 2D model (red curves) and the 2D-3D model (green curves). Other simulation parameters are the same as those used for obtaining blue curves in Figure 4.

nanometers resulting in strong electric field couplings of electrons on both sides of the trenches. As such, electron density fluctuations with time in the channel and in the monitored area indicated in Figure 1(a) have been studied for further understanding the device performances, especially the origin of second harmonic oscillations at DC bias. The monitored area is a rectangle with length and width of 420 nm and 35 nm, respectively. Results are shown in Figure 5(a) in the channel and Figure 5(b) near the channel (i.e., in the monitored area). Red curves and green curves are

obtained by the 2D model and the 2D-3D model, respectively. For convenience, results are normalized to time-averaged value. One can find that the changes of electron density with time in the channel obtained by both models are similar, showing obvious oscillations with the frequency about 0.3 THz. Such frequency is just the same as the fundamental frequency of the current oscillations, strongly implying that Gunn oscillations in the channel contribute to the appearance of the major peaks (or fundamental components of the current oscillations) shown in Figure 4. It is interesting

that electron densities near the channel (in the monitored area) also show oscillations with frequency about 0.3 THz. These electron density oscillations are expected to impose an additional AC electric field on the channel, which should give rise to an increase of second harmonic component of the oscillations in the channel. At the same time, oscillations near the channel are just out of phase with those oscillations in the channel, resulting in a counteraction of the fundamental component of oscillations. These two mechanisms should be responsible for the origin of the second harmonic oscillations at DC bias observed in the simulations. Since DC bias only leads to constant distributions of electron potential around the channel, the above electron density oscillation near the channel should only be excited by electric field induced by the Gunn domains in the channel. Moreover, the amplitude of electron density oscillations near the channel obtained by the 2D-3D model is only half of that obtained by the 2D model. Recalling that the additional current peaks (shown in Figure 4) obtained by the 2D-3D model are also lower than those obtained by the 2D model, the understanding of the second harmonic oscillations at DC bias as a result of an accompanying of an oscillation near the channel can be further confirmed.

#### 4. Conclusion

In this paper, we have carried out both entirely 2D EMC model and 2D-3D combined EMC model to analyze the performances of GaN based SSDs under different conditions. We find that both models give almost the same output current at bias lower than 4 V. However, the output current obtained by the 2D model shows a larger increment at bias higher than 4 V and reaches oscillation state at bias of 18 V that is 2 V higher than that obtained by the 2D-3D model. We also find that current oscillations obtained by both models exhibit similar fundamental frequencies, but much different waveforms, especially at high bias. Moreover the deviation of waveform from sinusoidal wave with voltage and device parameters obtained by the 2D model is more distinguished than that obtained by the 2D-3D model. The above divergences in simulation results should come from the different coupling path of electric field in the two models. Interestingly, a look-like second-harmonic waveform has been obtained by the 2D model at DC bias. Further investigations show that electric field induced by Gunn domains in the channel has excited electron density oscillations outside the channel. It is these concomitant oscillations that contribute to the appearance of second harmonic oscillations at DC bias. Our studies also imply that for nanodevices with dominant electric field coupling and working at high bias, electric field distribution should be obtained by 3D Poisson equations; otherwise additional treatments should be introduced for an entirely 2D model.

#### Conflict of Interests

The authors declare that there is no conflict of interests regarding the publication of this paper.

#### Acknowledgments

This work was supported by FOK YING TONG Education Foundation (no. 122004), Natural Science Foundation of Guangdong Province, China (no. S2013010012711), and NSFC (nos. 11374185, 61072029, and U0934002). This work was also supported by the high-performance computing platform of South China Normal University. The authors thank anonymous reviewers for their constructive comments.

#### References

- [1] A. M. Song, "Electron ratchet effect in semiconductor devices and artificial materials with broken centrosymmetry," *Applied Physics A*, vol. 75, no. 2, pp. 229–235, 2002.
- [2] A. M. Song, P. Omling, L. Samuelson, W. Seifert, I. Shorubalko, and H. Zirath, "Room-temperature and 50 GHz operation of a functional nanomaterial," *Applied Physics Letters*, vol. 79, no. 9, pp. 1357–1359, 2001.
- [3] C. Balocco, A. M. Song, M. Åberg et al., "Microwave detection at 110 GHz by nanowires with broken symmetry," *Nano Letters*, vol. 5, no. 7, pp. 1423–1427, 2005.
- [4] L. Worschech, F. Fischer, A. Forchel, M. Kamp, and H. Schweizer, "High frequency operation of nanoelectronic Y-branch at room temperature," *Japanese Journal of Applied Physics*, vol. 40, no. 8 B, pp. L867–L868, 2001.
- [5] C. Balocco, M. Halsall, N. Q. Vinh, and A. M. Song, "THz operation of asymmetric-nanochannel devices," *Journal of Physics Condensed Matter*, vol. 20, no. 38, Article ID 384203, 2008.
- [6] M. Åberg, J. Saijets, A. M. Song, and M. Prunnila, "Simulation and modeling of self-switching devices," *Physica Scripta*, vol. T114, p. 123, 2004.
- [7] M. Åberg and J. Saijets, "DC and AC characteristics and modeling of Si SSD-nano devices," in *Proceedings of the European Conference on Circuit Theory and Design*, pp. 15–18, irl, September 2005.
- [8] J. Mateos, B. G. Vasallo, D. Pardo, and T. González, "Operation and high-frequency performance of nanoscale unipolar rectifying diodes," *Applied Physics Letters*, vol. 86, no. 21, Article ID 212103, 3 pages, 2005.
- [9] I. Iñiguez-de-la-Torre, J. Mateos, D. Pardo, and T. González, "Monte Carlo analysis of noise spectra in self-switching nanodiodes," *Journal of Applied Physics*, vol. 103, no. 2, Article ID 024502, 2008.
- [10] I. Iñiguez-de-la-Torre, J. Mateos, D. Pardo, A. M. Song, and T. González, "Noise and terahertz rectification linked by geometry in planar asymmetric nanodiodes," *Applied Physics Letters*, vol. 94, no. 9, Article ID 093512, 2009.
- [11] K. Y. Xu, X. F. Lu, A. M. Song, and G. Wang, "Terahertz harmonic generation using a planar nanoscale unipolar diode at zero bias," *Applied Physics Letters*, vol. 92, no. 16, Article ID 163503, 3 pages, 2008.
- [12] K. Y. Xu, J. W. Xiong, A. M. Song, and G. Wang, "Effects of three-dimensional electric-field coupling on a side-gated nanotransistor," *Semiconductor Science and Technology*, vol. 26, no. 9, Article ID 095026, 6 pages, 2011.
- [13] T. Sadi, F. Dessenne, and J.-L. Thobel, "Three-dimensional Monte Carlo study of three-terminal junctions based on InGaAs/InAlAs heterostructures," *Journal of Applied Physics*, vol. 105, no. 5, Article ID 053707, 2009.

- [14] T. Sadi and J.-L. Thobel, "Analysis of the high-frequency performance of InGaAs/InAlAs nanojunctions using a three-dimensional Monte Carlo simulator," *Journal of Applied Physics*, vol. 106, no. 8, Article ID 083709, 2009.
- [15] T. Sadi and J.-L. Thobel, "Study of the high-frequency performance of III-As nanojunctions using a three-dimensional ensemble Monte Carlo model," *Journal of Physics: Conference Series*, vol. 193, Article ID 012017, 2009.
- [16] I. Íñiguez-de-la-Torre, T. González, D. Pardo et al., "Three-terminal junctions operating as mixers, frequency doublers and detectors: a broad-band frequency numerical and experimental study at room temperature," *Semiconductor Science and Technology*, vol. 25, no. 12, Article ID 125013, 2010.
- [17] K. Y. Xu, G. Wang, and A. M. Song, "Gunn oscillations in a self-switching nanodiode," *Applied Physics Letters*, vol. 93, no. 23, Article ID 233506, 2008.
- [18] A. Íñiguez-de-la-Torre, I. Íñiguez-de-la-Torre, J. Mateos et al., "Searching for THz Gunn oscillations in GaN planar nanodiods," *Journal of Applied Physics*, vol. 111, no. 11, Article ID 113705, 2012.
- [19] A. M. Song, M. Missous, P. Omling, A. R. Peaker, L. Samuelson, and W. Seifert, "Unidirectional electron flow in a nanometer-scale semiconductor channel: a self-switching device," *Applied Physics Letters*, vol. 83, no. 9, pp. 1881–1883, 2003.
- [20] C. Jacoboni and P. Lugli, *The Monte Carlo Method for Semiconductor Device Simulation*, Springer, New York, NY, USA, 1989.
- [21] K. Y. Xu, X. F. Lu, G. Wang, and A. M. Song, "Strong spatial dependence of electron velocity, density, and intervalley scattering in an asymmetric nanodevice in the nonlinear transport regime," *IEEE Transactions on Nanotechnology*, vol. 7, no. 4, pp. 451–457, 2008.
- [22] K. Y. Xu, X. F. Lu, A. M. Song, and G. Wang, "Enhanced terahertz detection by localized surface plasma oscillations in a nanoscale unipolar diode," *Journal of Applied Physics*, vol. 103, Article ID 113708, 2008.
- [23] N. Ma, B. Shen, F. J. Xu et al., "Current-controlled negative differential resistance effect induced by Gunn-type instability in n-type GaN epilayers," *Applied Physics Letters*, vol. 96, no. 24, Article ID 242104, 2010.
- [24] I. Íñiguez-de-la-Torre, J. Mateos, T. González et al., "Influence of the surface charge on the operation of ballistic T-branch junctions: a self-consistent model for Monte Carlo simulations," *Semiconductor Science and Technology*, vol. 22, no. 6, pp. 663–670, 2007.

## Research Article

# The Effect of Bilayer Graphene Nanoribbon Geometry on Schottky-Barrier Diode Performance

Meisam Rahmani,<sup>1</sup> Razali Ismail,<sup>1</sup> Mohammad Taghi Ahmadi,<sup>1,2</sup> Mohammad Javad Kiani,<sup>3</sup> Mehdi Saeidmanesh,<sup>1</sup> F. A. Hediye Karimi,<sup>4</sup> Elnaz Akbari,<sup>4</sup> and Komeil Rahmani<sup>5</sup>

<sup>1</sup> Faculty of Electrical Engineering, Universiti Teknologi Malaysia, 81310 Skudai, Johor Bahru, Malaysia

<sup>2</sup> Nanotechnology Research Center Nanoelectronic Group, Physics Department, Urmia University, Urmia 57147, Iran

<sup>3</sup> Department of Electrical Engineering, Islamic Azad University, Yasooj Branch, Yasooj 63614, Iran

<sup>4</sup> Centre for Artificial Intelligence and Robotics (CAIRO), UTM, 81310 Skudai, Johor Bahru, Malaysia

<sup>5</sup> Department of Electrical, Computer and Biomedical Engineering, Islamic Azad University, Qazvin Branch, Qazvin 34185-1416, Iran

Correspondence should be addressed to Razali Ismail; [razali@fke.utm.my](mailto:razali@fke.utm.my)

Received 21 August 2013; Revised 11 October 2013; Accepted 17 October 2013

Academic Editor: Munawar A. Riyadi

Copyright © 2013 Meisam Rahmani et al. This is an open access article distributed under the Creative Commons Attribution License, which permits unrestricted use, distribution, and reproduction in any medium, provided the original work is properly cited.

Bilayer graphene nanoribbon is a promising material with outstanding physical and electrical properties that offers a wide range of opportunities for advanced applications in future nanoelectronics. In this study, the application of bilayer graphene nanoribbon in schottky-barrier diode is explored due to its different stacking arrangements. In other words, bilayer graphene nanoribbon schottky-barrier diode is proposed as a result of contact between a semiconductor (AB stacking) and metal (AA stacking) layers. To this end, an analytical model joint with numerical solution of carrier concentration for bilayer graphene nanoribbon in the degenerate and nondegenerate regimes is presented. Moreover, to determine the proposed diode performance, the carrier concentration model is adopted to derive the current-voltage characteristic of the device. The simulated results indicate a strong bilayer graphene nanoribbon geometry and temperature dependence of current-voltage characteristic showing that the forward current of the diode rises by increasing of width. In addition, the lower value of turn-on voltage appears as the more temperature increases. Finally, comparative study indicates that the proposed diode has a better performance compared to the silicon schottky diode, graphene nanoribbon homo-junction contact, and graphene-silicon schottky diode in terms of electrical parameters such as turn-on voltage and forward current.

## 1. Introduction

Graphene nanoribbon (GNR) has attracted much attention of researchers for nanoelectronic applications because of its uniqueness electronic characteristics such as linear energy dispersion and width-tunable energy band gap [1–5]. Due to quantum confinement effect, GNR with width and thickness less than De-Broglie wave length ( $\lambda_D = 10$  nm) can be assumed as a one-dimensional (1D) material [6]. GNR as an unwrapped carbon nanotube (CNT) is illustrated in Figure 1. It is notable that the properties of GNR are similar to CNT, but the planar structure of GNR guarantees better rectification current-voltage characteristic due to more accessible contact compared to other carbon-based materials [6]. Bilayer graphene nanoribbon (BGN) with unique physical

and electrical properties has been incorporated in different nanoscale devices such as field effect transistors (FETs), tunnel transistors, and schottky diodes [7–11]. The BGN schottky-barrier diode has turned out to be of great interest holding the fact that it presents better performance compared to conventional semiconductor *p-n* junction contacts [12]. In this paper, analytical modeling of BGN schottky-barrier diode is presented in which the effect of BGN geometry and temperature on the proposed diode performance is investigated.

## 2. Schottky-Barrier Contact

Schottky-barrier diode is a nonideal contact between a semiconductor and a metal. Rectification of alternating current is

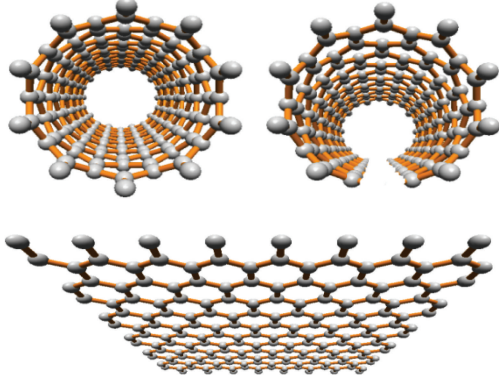


FIGURE 1: Graphene nanoribbon as a promising material for schottky contact.

a main relevant characteristic of the schottky-barrier diode [2]. The thermionic emission theory is known as the most important step in rectifying the contact with an  $n$ -type semiconductor throughout transport of electrons on top of the anticipated barrier [13]. Schottky-barrier diode based on GNR as a powerful device can be applied in a wide range of nanoelectronic applications because of its special advantages such as low junction capacitance, low turn-on voltage, fast recovery time, and high operating frequencies [13, 14, 16–18]. Also, RF signal rectification/detection, mixing, and imaging have been found to be some of its wide applications [13, 14, 16–18]. The different stacking arrangements of BGN (AA and AB) in interlayer coupling between the top and bottom layers are weaker than those of interlayer coupling within layers leading to an electrical conduction [14, 19]. The electrical conduction through the layers is exposed by the carrier hopping between the  $\pi$  orbits, with the van der Waals forces contributing to the coupling interaction among the layers' structure [19]. The transport conduction channels are essentially generated by passing through the layers of BGN rather than between those layers [19]. As shown in Figure 2, the different configuration of AB stacking compared to AA is because of the shift in the distance of lattice in the armchair edges. Apparently, BGN with AB stacking is modeled in form of two honeycomb lattices with pairs of in-equivalent sites as  $(A_1, B_1)$  and  $(B_2, A_2)$  which are located in the top and bottom layers, respectively. However, in AA-stacked BGN, the pairs of in-equivalent sites  $(A_1, B_1)$  and  $(A_2, B_2)$  are located in the top and bottom layers, respectively. It is noteworthy that in BGN the carriers can move only in the  $x$ -direction. However, the carriers are confined to the  $y$ - and  $z$ -Cartesian directions being less than the De-Broglie wave length [14, 19].

Different stacking sequences of BGN show metallic and semiconducting (with a band gap of 0.02 eV) properties, respectively [20–22]. This means that, by engineering of BGN different arrangements, the schottky-barrier contact can be designed as depicted in Figure 3.

### 3. Proposed Model

The energy dispersion relation of BGN in the attendance of a perpendicular electric field is obtained by the tight-binding

technique. In this method, a self-consistent Hartree approximation can be utilized to estimate the induced charges on the different layers of BGN. This is because, as the Fermi surface of the intrinsic BGN communicates to the K-points, the tight-binding method is a suitable technique for the low energy excitations [23]. In addition, the tight-binding method with a single  $p_z$  orbital per atom includes coupling parameters between the neighbor sites within BGN layers. In fact, the  $p_z$  orbitals are considered to study the behavior of electrons around the Fermi level. The different  $sp^2$  orbitals that are lower than the  $p_z$  orbital in energy will have much more overlap with the orbitals of the same symmetry on adjacent atoms [23]. Furthermore, the interaction between the  $p_z$  orbitals of adjacent atoms is small, which results in bonding and antibonding orbitals close to the Fermi level. Therefore, the resulting bonding and antibonding molecular orbitals will recline below and above the Fermi level, respectively [23]. It is notable that the bonding and antibonding combinations are equal and communicate to orbitals which are limited to one of the two sublattices. This means that these orbitals are non-bonding in the nearest-neighbor approximation, so their relative energy is zero [23]. For the proposed 1D BGN schottky-barrier diode, the tight-binding technique is adopted in order to calculate the energy band structure of BGN with AB stacking [24]:

$$E_k(V) = \pm \sqrt{\epsilon_k^2 + \frac{t_{\perp}^2}{2} + \frac{V^2}{4}} \pm \sqrt{(t_{\perp}^2 + V^2)\epsilon_k^2 + \frac{t_{\perp}^4}{4}}, \quad (1)$$

where  $t_{\perp}$  is the interlayer hopping energy,  $V$  is the applied voltage, and  $\epsilon_k^2 = (V^4/4 + V^2 t_{\perp}^2/2)/(V^2 + t_{\perp}^2)$ . Equation (1) can be exposed as

$$E(k) \approx \Delta - \alpha k^2 + \beta k^4, \quad (2)$$

where  $\Delta = V/2$  is the bias voltage,  $k$  is the wave vector,  $\alpha = (V/t_{\perp}^2)v_F^2$ ,  $\beta = v_F^4/Vt_{\perp}^2$ ,  $v_F = 3t \times a_{c-c}/2$  is the Fermi velocity, and  $a_{c-c} = 1.41 \text{ \AA}$  is the lattice-spacing [25–28]. Figure 4 illustrates the energy band structure of BGN near the Fermi level which is plotted based on (2).

Unbiased BGN ( $V = 0$ ) indicates zero band gap; however, energy dispersion of biased BGN by nonzero value of the applied voltage ( $V$ ) makes a gap between the conduction and valance bands. It is notable that the size of gap depends on the applied voltage and can be externally controlled by perpendicular electric field.

The density of states (DOS) as a fundamental factor shows the number of available states at each energy level that is occupied [29]. Hence DOS for BGN can be modeled as

$$D(k) = \frac{1}{2\pi(4\beta k^3 - 2\alpha k)}. \quad (3)$$

Over energy band structure, carrier concentration can be calculated by integrating the distribution function as

$$dn = \frac{1}{2\pi(4\beta k^3 - 2\alpha k)} \frac{1}{(1 + e^{(E-E_F)/k_B T})} dE, \quad (4)$$

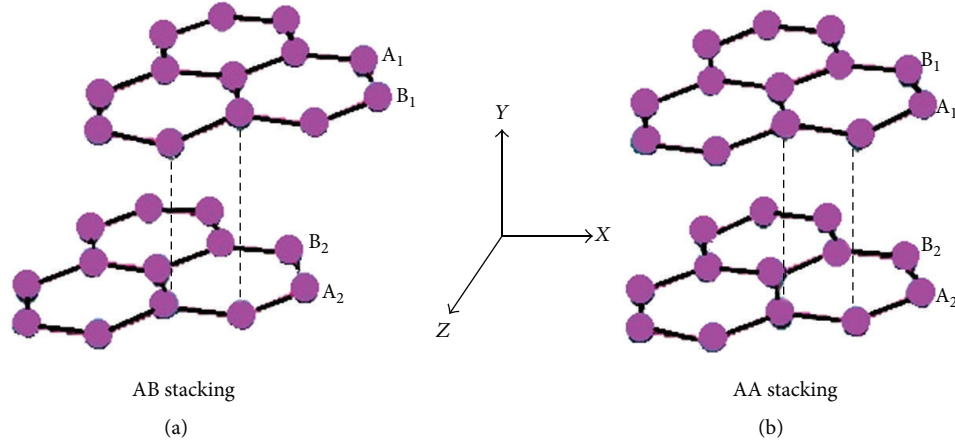


FIGURE 2: Configuration of BGN: (a) AB stacking and (b) AA stacking.

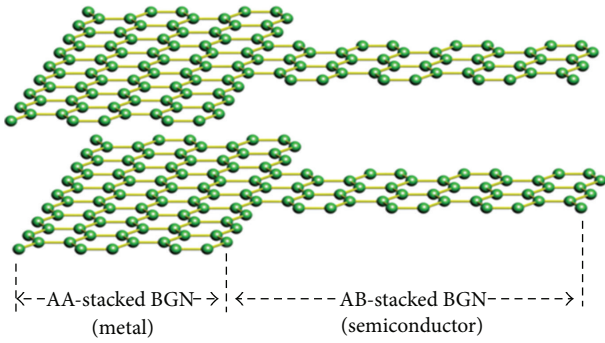


FIGURE 3: The proposed schematic of BGN schottky-barrier contact.

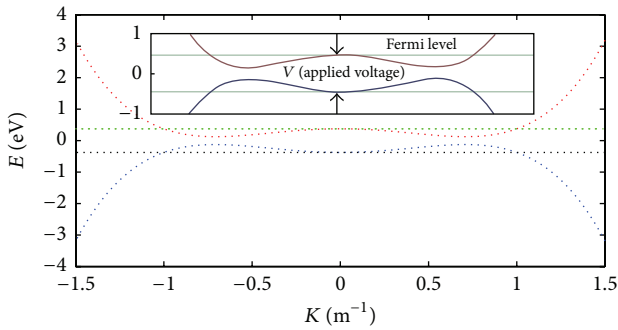


FIGURE 4: The energy band structure of BGN near the Fermi level.

where  $k = [(\alpha \pm \sqrt{\alpha^2 - 4(E - \Delta)\beta})/2\beta]^{1/2}$ , which is achieved from the band energy equation (2). Considering the importance of carrier concentration, the proposed model of carrier concentration for BGN schottky-barrier diode in the degenerate and nondegenerate regimes is analytically studied. The band gap exhibits a nondegenerate approximation as the distance of Fermi level is more than  $3K_B T$  from either the conduction or valence bands [30]. In this region, because of high difference between  $E$  and  $E_F$ , one (1) can be neglected in comparison with the exponential function as specified in

(4). Consequently, the model in the nondegenerate regime is carried out by the following equation as

$$n_{\text{Nondegenerate}} = \int_0^\infty \left( e^{-(E-E_F)/k_B T} dE \right) \times \left( 2\pi \left[ 4\beta \left( \frac{\alpha \pm \sqrt{\alpha^2 - 4(E - \Delta)\beta}}{2\beta} \right)^{3/2} - 2\alpha \left( \frac{\alpha \pm \sqrt{\alpha^2 - 4(E - \Delta)\beta}}{2\beta} \right)^{1/2} \right] \right)^{-1} \quad (5)$$

Fermi level in the degenerate approximation is located less than  $3K_B T$  away from the conduction and valence bands or situated within a band [30]. In this case, we can neglect the  $\exp(E - E_F)$  in comparison with (1) because the value of  $E - E_F$  is very small. Therefore, the model of carrier concentration in the degenerate regime is proposed as

$$n_{\text{Degenerate}} = \int_0^\infty \left( dE \times \left( 2\pi \left[ 4\beta \left( \frac{\alpha \pm \sqrt{\alpha^2 - 4(E - \Delta)\beta}}{2\beta} \right)^{3/2} - 2\alpha \left( \frac{\alpha \pm \sqrt{\alpha^2 - 4(E - \Delta)\beta}}{2\beta} \right)^{1/2} \right] \right)^{-1} \right) \quad (6)$$

As shown in Figure 5, the proposed model of carrier concentration for BGN schottky-barrier diode is approximated by the nondegenerate limit, particularly in low value of the

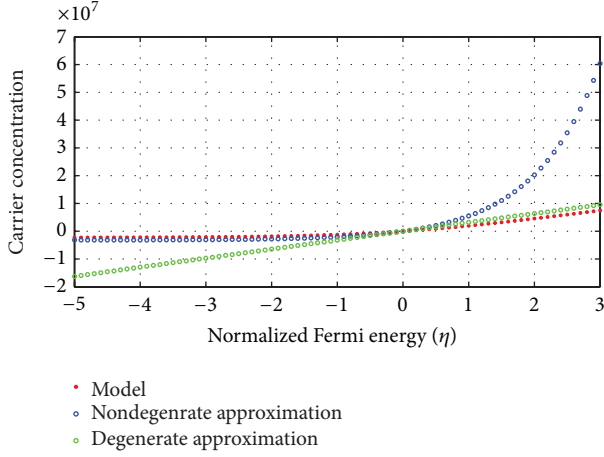


FIGURE 5: Carrier concentration of BGN in the degenerate and nondegenerate regimes.

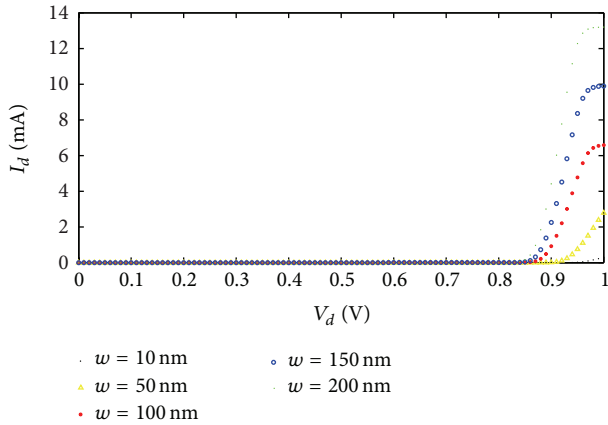


FIGURE 6: Rectification I-V characteristic of BGN schottky-barrier diode at different values of width  $w$  ( $l = 100$  nm).

normalized Fermi energy  $\eta$  ( $\eta \leq 0.5$ ), where ( $\eta = (-E_C + E_f)/k_B T$ ). On the other hand, the model can be approximated by the degenerate limit, specifically in high value of  $\eta$  ( $\eta > 0.5$ ).

In the structure of schottky-barrier contact, carriers are injected directly from the metal into the empty space of semiconductor. So, current density  $J_{s \rightarrow m}$  is defined [13] as

$$J_{s \rightarrow m} = e \int_{-\infty}^{+\infty} v_x dn, \quad (7)$$

where  $e$  is the magnitude of the electronic charge and  $v_x$  is the carrier velocity in the direction of transport. Kinetic energy is utilized as a main parameter over the Fermi level to calculate the current density [14]. By substitution of the carrier concentration model in (7), the current of BGN schottky-barrier diode is analytically derived as (8). As specified in (8), the current of the proposed diode is a function of various physical and electrical characteristics including the carrier effective

mass ( $m^*$ ), channel area ( $A$ ), temperature ( $T$ ), applied bias voltage ( $V_A$ ), and thermal voltage ( $V_T$ ):

$$\begin{aligned} I_{s \rightarrow m} &= \frac{\sqrt{2}e(k_B T)^{3/2} A}{2\pi \sqrt{m^*}} \\ &\times \int_0^\eta \left( x^{1/2} dx \right. \\ &\times \left( \left[ 4\beta \left( \frac{\alpha \pm \sqrt{\alpha^2 - 4(k_B T)\beta x}}{2\beta} \right)^{3/2} \right. \right. \\ &\quad \left. \left. - 2\alpha \left( \frac{\alpha \pm \sqrt{\alpha^2 - 4(k_B T)\beta x}}{2\beta} \right)^{1/2} \right] \right. \\ &\quad \left. \left. \times (1 + e^{x-\eta}) \right)^{-1} \right), \end{aligned} \quad (8)$$

where  $A$  is the area of the channel which is proportional with channel width,  $x = (E - E_C)/k_B T$ , and  $\eta \approx (V_A - V_T)/(k_B T/e)$  [31].

## 4. Results and Discussion

The purpose of this study is to highlight the influence of BGN geometry and temperature characteristics on the performance of the schottky-barrier diode. As can be seen in Figure 6, the rectification current-voltage characteristic of the proposed diode at different values of the width is illustrated. Apparently, there is a significant rise in the forward current of the diode as the BGN width increases. Strong dependence of I-V characteristic to the mentioned geometry parameter demonstrates that the increment of BGN width plays an important role in the forward current of the device. In other words, the diode performance will be enhanced by the left-shifted turn-on voltage. To get a better insight into the effect of BGN geometry on the increment of the diode current, two significant factors play an important role, which are the transparency of schottky-barrier contact and the extension of the energy for carrier concentration [32]. For the first parameter, as the diode current and schottky-barrier height are affected significantly by the charges, the channel width effect on the current through the schottky-barrier contact is taken into account in the proposed model. Furthermore, when the center of the channel is unoccupied with the charge impurities, the current increases due to the fact that free electrons are not affected by the positive charges [32]. The effect of second parameter emerges at the beginning of the channel where the barrier potential reduces as a result of

TABLE 1: Turn-on voltage of BGN schottky-barrier diode at different values of BGN width.

BGN Width (nm)	10	50	100	150	200
Turn-on Voltage (V)	0.95	0.92	0.88	0.87	0.86

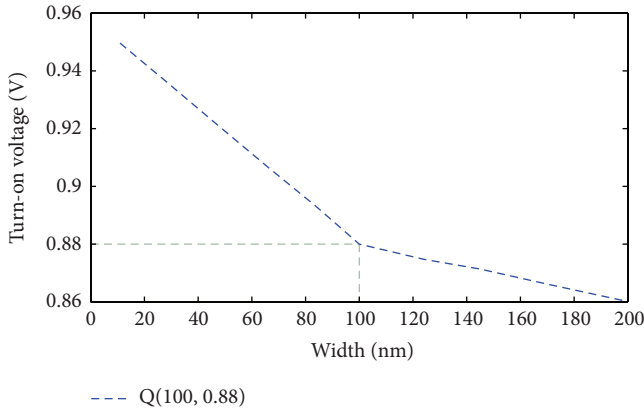


FIGURE 7: Turn-on voltage versus width characteristic of BGN schottky-barrier diode.

low charge density. This phenomenon leads to widening the energy casement and relieve of electron flow in the channel [32]. Moreover, due to the long mean free path (MFP) of GNR, scattering effect is not dominant [32]; therefore increasing the BGN geometry will result in a larger forward current.

Figure 7 indicates the turn-on voltage versus width characteristic of BGN schottky-barrier diode in which the turn-on voltage of diode decreases by increasing the width of BGN. As depicted in Figure 7, Q (100, 0.88) as an inflection point can be considered a turning point after which a remarkable change is expected to result.

According to Figures 6 and 7, the turn-on voltage of the diode is obtained for different values of BGN width as shown in Table 1.

Thermodynamic stability is one of the most important properties of BGN [30]. In fact, the carrier transport in BGN is a vital phenomenon that determines the I-V characteristic of the device. The effect of temperature on current-voltage characteristic of BGN schottky-barrier diode is investigated in Figure 8. According to the relationship between the current and conductance [31], the presented model indicates a strong temperature dependence of current-voltage characteristic showing that the lower value of turn-on voltage appears as the more temperature increases.

In other words, the turn-on voltage will be shifted leftwards and the proposed diode performance will be enhanced. In fact, the conductance of BGN is expected to be affected by the temperature. It has been demonstrated that the minimum conductance of BGN depends on the bias voltage [30]. In BGN, the temperature dependence of conductance is strongly affected by lower applied perpendicular electric field, and weakly temperature dependence of conductance has been

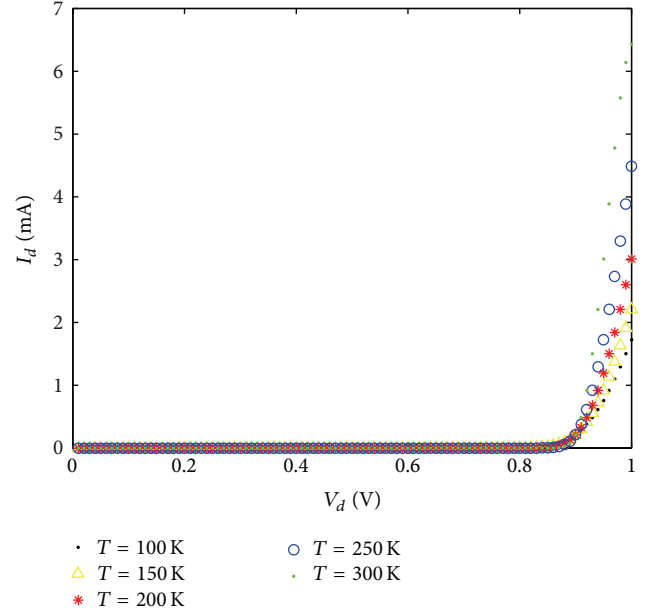


FIGURE 8: Rectification I-V characteristic of BGN schottky-barrier diode at different temperatures ( $w = 100$  nm,  $l = 100$  nm).

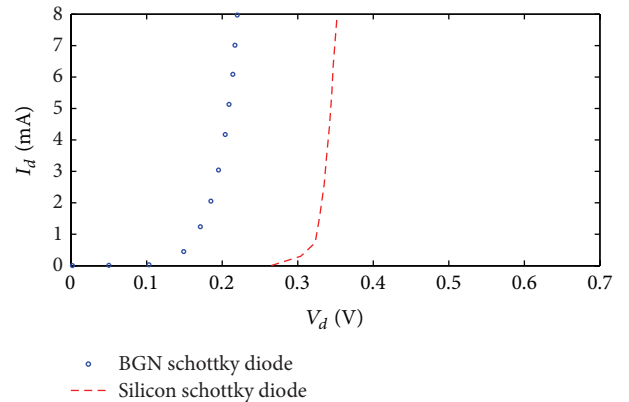


FIGURE 9: Comparison between BGN schottky-barrier diode with silicon schottky diode [13, 14].

reported in higher electric field [30]. According to the zero-gap semiconductor characteristic, the conductance of GNR near the charge-neutrality peak is basically temperature independent for small bias voltages. In contrary, the temperature dependence of conductance in BGN is markedly different from that measured in the GNR. On the other hand, no sign of increase in BNG conductivity with increasing temperature away from the neutrality point has not been observed [30]. It is notable that the temperature dependence of current-voltage characteristic in BGN revealed a new effect of a memory step close to the charge neutrality voltage. The effect is related to the slow relaxation processes in BGN. This characteristic of electron transport in BGN can be adopted in high-temperature applications. It is concluded

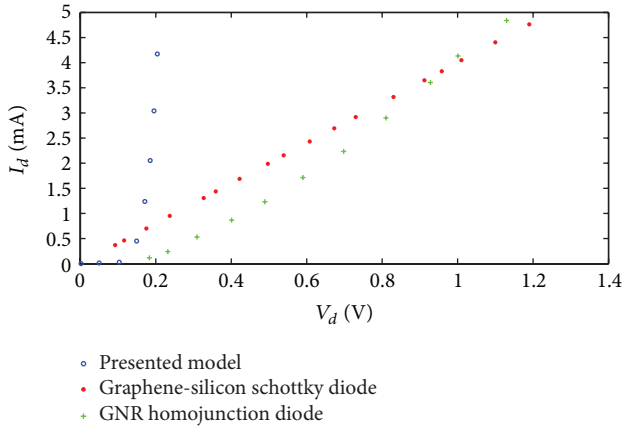


FIGURE 10: Comparison between the BGN schottky-barrier diode with graphene-silicon schottky diode and GNR homojunction diode [6, 15].

that temperature is an effective factor in the forward current and turn-on voltage of BGN schottky-barrier contact, leading to movement of free carriers in diode. According to the simulated result in Figure 7, the point of Q (100, 0.88) is an inflection point, and hence the width of 100 nm is considered as an inflection width in Figure 8.

Figure 9 indicates a comparative study of the proposed device and the typical I-V characteristic of a silicon schottky diode [13, 14]. Apparently, the effective turn-on voltage of silicon schottky diode is about 0.3 V. The proposed BGN schottky-barrier diode also possesses a turn-on voltage of 0.1 V that is smaller than the voltage of silicon schottky diode. Accordingly, the proposed diode shows a better performance compared to the conventional silicon schottky diode in terms of the turn-on voltage.

As shown in Figure 10, the proposed BGN schottky-barrier diode has a better performance compared to the graphene-silicon schottky diode and GNR homojunction diode in terms of forward current. Moreover, smaller turn-on voltage of the proposed diode (0.1 V) in comparison with GNR homojunction diode is indicated in Figure 10. Accordingly, an acceptable rectifying performance is seen comparable with conventional rectification behavior of the schottky diodes.

Difference between the BGN schottky-barrier diode and the conventional diodes in terms of mentioned electrical parameters can be associated with diode switching characteristics. It clearly gives an illustration of the fact that GNR-based device characterized by steep subthreshold slope displays a faster transient between on-off states [32]. In fact, a small value of subthreshold slope denotes a small change in the input bias which can modulate the output current and thus leads to less power consumption [32]. It is concluded that due to some excellent properties of GNR such as quantum transport, long spin-diffusion length, and extremely high carrier mobility [32], the proposed schottky-barrier diode can be used as a high speed device in future nanoelectronics.

## 5. Defects Effect on the Device Performance

There are various controllable defects in GNR, including the adatoms, vacancies, substitution, disorder, and stone wales (SW) defects [33]. It is noteworthy that the electronic properties of GNR can be functionalized via inhomogeneities, vacancies, topological defects, doping, adsorption, chemical functionalization, and molecular junctions [34]. It has been investigated that the existence of the defects in GNR is energetically more favorable than in fullerene or CNT [33]. The inhomogeneities, vacancies, and defects can lead to scattering in GNR. These defects persuade long-range deformations, which alter the electron routes [35]. The bond angle of the edge close to the SW defects is reduced from  $120^\circ$  to  $116^\circ$ . In contrast to the shrinking through the width axis, the SW defects stretch from  $4.88^\circ\text{A}$  to  $5.38^\circ\text{A}$  through the length axis direction, and the transformation energy for the symmetric SW defects is 5.95 eV [33]. SW defects have been predicted to modify the band structure and DOS of GNR and hence to impact upon its transport properties [36]. Recent results demonstrate that the defects alter GNR's chemical reactivity on the chemisorption processes [36]. SW defects can enhance the tendency of graphitic layers to transform into the nonplanar nanostructures, and the defects can play an important role in the intrinsic rumpling of GNR [37]. Additionally, the symmetry effects yield a remarkable conductance decrease in the SW defects configuration [33]. Moreover, the maximum value of Fermi velocity considering the SW defects is  $5.25 \times 10^5$  m/s which is about 50% less than the perfect GNR. This is because the defects modify the electron trajectories [38]. According to the ballistic conductance and carrier velocity dependence of current-voltage characteristic [39, 40], it is concluded that the performance of the schottky-barrier diode can be infused by inhomogeneities, vacancies, and defects. As a future work, the effects of SW defects on the BGN schottky-barrier diode performance will be analytically studied.

## 6. Conclusion

In this study, BGN with various stacking arrangements (AA and AB) is applied as a metal and semiconductor contact in a junction schottky-barrier device. According to this assumption, an analytical model for BGN schottky-barrier diode is presented, and the effect of BGN geometry and temperature on I-V characteristic of the device is studied. Based on what has been discussed, by increasing the BGN width, the forward current of diode increases. Moreover, the simulated result indicates that the lower value of turn-on voltage appears as the more temperature increases, which guarantees a better performance of the proposed diode. Finally, a comparative study of the proposed model with silicon schottky diode, GNR homojunction contact, and graphene-silicon schottky diode is presented. Accordingly, an acceptable rectifying performance is seen comparable with conventional rectification behavior of the schottky diodes. To optimize the performance of BGN schottky-barrier diode, the presented model can be applied as a useful

tool. It is concluded that the model can assist in comprehending experiments involving GNR schottky-barrier based devices.

## Acknowledgments

The authors would like to acknowledge the financial support by Research University grant of the Ministry of Higher Education (MOHE), Malaysia, under Projects Q.J130000.7123.02H24 and Q.J130000.7123.02H04. Also thanks are due to the Research Management Center (RMC) of Universiti Teknologi Malaysia (UTM) for providing excellent research environment in which they completed this work.

## References

- [1] K. S. Novoselov, A. K. Geim, S. V. Morozov et al., "Electric field in atomically thin carbon films," *Science*, vol. 306, no. 5696, pp. 666–669, 2004.
- [2] A. Kargar and D. L. Wang, "Analytical modeling of graphene nanoribbon Schottky diodes," in *Carbon Nanotubes, Graphene and Associated Devices III*, vol. 7761 of *Proceedings of the SPIE*, San Diego, Calif, USA, August 2010.
- [3] K. Alam, "Transport and performance of a zero-Schottky barrier and doped contacts graphene nanoribbon transistors," *Semiconductor Science and Technology*, vol. 24, no. 1, Article ID 015007, 2009.
- [4] M. H. Ghadiry, M. Nadi, M. Rahmani, M. T. Ahmadi, and A. B. A. Manaf, "Modelling and simulation of saturation region in double gate graphene nanoribbon transistors," *Semiconductors*, vol. 46, no. 1, pp. 126–129, 2012.
- [5] M. T. Ahmadi, Z. Johari, N. A. Amin, A. H. Fallahpour, and R. Ismail, "Graphene nanoribbon conductance model in parabolic band structure," *Journal of Nanomaterials*, vol. 2010, Article ID 753738, 4 pages, 2010.
- [6] M. T. Ahmadi, M. Rahmani, M. H. Ghadiry, and R. Ismail, "Monolayer graphene nanoribbon homojunction characteristics," *Science of Advanced Materials*, vol. 4, no. 7, pp. 753–756, 2012.
- [7] Y. Ouyang, Y. Yoon, and J. Guo, "Scaling behaviors of graphene nanoribbon FETs: a three-dimensional quantum simulation study," *IEEE Transactions on Electron Devices*, vol. 54, no. 9, pp. 2223–2231, 2007.
- [8] Y. Yoon, G. Fiori, S. Hong, G. Iannaccone, and J. Guo, "Performance comparison of graphene nanoribbon FETs with Schottky contacts and doped reservoirs," *IEEE Transactions on Electron Devices*, vol. 55, no. 9, pp. 2314–2323, 2008.
- [9] Q. Zhang, T. Fang, H. Xing, A. Seabaugh, and D. Jena, "Graphene nanoribbon tunnel transistors," *IEEE Electron Device Letters*, vol. 29, no. 12, pp. 1344–1346, 2008.
- [10] A. Naeemi and J. D. Meindl, "Conductance modeling for graphene nanoribbon (GNR) interconnects," *IEEE Electron Device Letters*, vol. 28, no. 5, pp. 428–431, 2007.
- [11] Q. Liang and J. Dong, "Superconducting switch made of graphene-nanoribbon junctions," *Nanotechnology*, vol. 19, no. 35, Article ID 355706, 2008.
- [12] D. Jena, T. Fang, Q. Zhang, and H. Xing, "Zener tunneling in semiconducting nanotube and graphene nanoribbon p-n junctions," *Applied Physics Letters*, vol. 93, no. 11, Article ID 112106, 3 pages, 2008.
- [13] D. A. Neamen, *Semiconductor Physics and Devices*, University of New Mexico, Albuquerque, NM, USA, 3rd edition, 2003.
- [14] M. Rahmani, M. T. Ahmadi, R. Ismail, and M. H. Ghadiry, "Performance of bilayer graphene nanoribbon Schottky diode in comparison with conventional diodes," *Journal of Computational and Theoretical Nanoscience*, vol. 10, no. 2, pp. 323–327, 2013.
- [15] C.-C. Chen, M. Aykol, C.-C. Chang, A. F. J. Levi, and S. B. Cronin, "Graphene-silicon Schottky diodes," *Nano Letters*, vol. 11, no. 5, pp. 1863–1867, 2011.
- [16] S. Sankaran and K. O. Kenneth, "Schottky barrier diodes for millimeter wave detection in a foundry CMOS process," *IEEE Electron Device Letters*, vol. 26, no. 7, pp. 492–494, 2005.
- [17] A. Kargar and C. Lee, "Graphene nanoribbon schottky diodes using asymmetric contacts," in *Proceedings of the 9th IEEE Conference on Nanotechnology*, pp. 243–245, Genoa, Italy, July 2009.
- [18] D. Jimenez, "A current-voltage model for Schottky-barrier graphene-based transistors," *Nanotechnology*, vol. 19, no. 34, Article ID 345204, 2008.
- [19] S. M. Mousavi, M. T. Ahmadi, H. Sadeghi et al., "Bilayer graphene nanoribbon carrier statistic in degenerate and non degenerate limit," *Journal of Computational and Theoretical Nanoscience*, vol. 8, no. 10, pp. 2029–2032, 2011.
- [20] S. Latil and L. Henrard, "Charge carriers in few-layer graphene films," *Physical Review Letters*, vol. 97, no. 3, Article ID 036803, 4 pages, 2006.
- [21] M. Koshino, "Electron delocalization in bilayer graphene induced by an electric field," *Physical Review B*, vol. 78, no. 15, Article ID 155411, 5 pages, 2008.
- [22] M. Koshino, "Electronic transport in bilayer graphene," *New Journal of Physics*, vol. 11, no. 9, Article ID 095010, 2009.
- [23] M. Rahmani, R. Ismail, M. T. Ahmadi, and M. H. Ghadiry, "Quantum confinement effect on trilayer graphene nanoribbon carrier concentration," *Journal of Experimental Nanoscience*, 2013.
- [24] E. V. Castro, K. S. Novoselov, S. V. Morozov et al., "Electronic properties of a biased graphene bilayer," *Journal of Physics Condensed Matter*, vol. 22, no. 17, Article ID 175503, 2010.
- [25] T. Stauber, N. M. R. Peres, F. Guinea, and A. H. C. Neto, "Fermi liquid theory of a Fermi ring," *Physical Review B*, vol. 75, no. 11, Article ID 115425, 10 pages, 2007.
- [26] D. S. Novikov, "Numbers of donors and acceptors from transport measurements in graphene," *Applied Physics Letters*, vol. 91, no. 10, Article ID 102102, 2007.
- [27] Z. Q. Li, E. A. Henriksen, Z. Jiang et al., "Band structure asymmetry of bilayer graphene revealed by infrared spectroscopy," *Physical Review Letters*, vol. 102, no. 3, Article ID 037403, 4 pages, 2009.
- [28] E. V. Castro, N. M. R. Peres, J. M. B. L. Dos Santos, F. Guinea, and A. H. C. Neto, "Bilayer graphene: gap tunability and edge properties," *Journal of Physics: Conference Series*, vol. 129, no. 1, Article ID 012002, 2008.
- [29] F. Guinea, A. H. C. Neto, and N. M. R. Peres, "Interaction effects in single layer and multi-layer graphene," *European Physical Journal*, vol. 148, no. 1, pp. 117–125, 2007.
- [30] H. Sadeghi, S. M. Mousavi, M. Rahmani, M. T. Ahmadi, and R. Ismail, "Bilayer graphene nanoribbon transport model," in *Advanced Nanoelectronics*, chapter 7, Taylor & Francis, New York, NY, USA, 2012.

- [31] S. Datta, *Quantum Transport: Atom to Transistor*, Cambridge University Press, New York, NY, USA, 2005.
- [32] M. Rahmani, M. T. Ahmadi, H. Karimi, M. Saeidmanesh, E. Akbari, and R. Ismail, "Analytical modeling of trilayer graphene nanoribbon Schottky-barrier FET for high-speed switching applications," *Nanoscale Research Letters*, vol. 8, no. 1, article 55, 2013.
- [33] H. Zeng, J. Zhao, J. W. Wei, and H. F. Hu, "Effect of N doping and Stone-Wales defects on the electronic properties of graphene nanoribbons," *The European Physical Journal B*, vol. 79, no. 3, pp. 335–340, 2011.
- [34] J. Kotakoski, A. V. Krasheninnikov, U. Kaiser, and J. C. Meyer, "From point defects in graphene to two-dimensional amorphous carbon," *Physical Review Letters*, vol. 106, no. 10, Article ID 105505, 4 pages, 2011.
- [35] A. H. C. Neto, F. Guinea, N. M. R. Peres, K. S. Novoselov, and A. K. Geim, "The electronic properties of graphene," *Reviews of Modern Physics*, vol. 81, no. 1, pp. 109–162, 2009.
- [36] L. Chen, H. Hu, Y. Ouyang, H. Z. Pan, Y. Y. Sun, and F. Liu, "Atomic chemisorption on graphene with Stone-Thrower-Wales defects," *Carbon*, vol. 49, no. 10, pp. 3356–3361, 2011.
- [37] J. Ma, D. Alfè, A. Michaelides, and E. Wang, "Stone-Wales defects in graphene and other planar  $sp^2$ -bonded materials," *Physical Review B*, vol. 80, no. 3, Article ID 033407, 4 pages, 2009.
- [38] Y. J. Sun, F. Ma, D. Y. Ma, K. W. Xu, and P. K. Chu, "Stress-induced annihilation of Stone-Wales defects in graphene nanoribbons," *Journal of Physics D*, vol. 45, no. 30, Article ID 305308, 2012.
- [39] M. Rahmani, R. Ismail, M. T. Ahmadi, M. J. Kiani, and K. Rahmani, "Carrier velocity in high-field transport of trilayer graphene nanoribbon field effect transistor," *Science of Advanced Materials*. In press.
- [40] M. Rahmani, M. T. Ahmadi, H. F. A. Karimi, M. J. kiani, E. Akbari, and R. Ismail, "Analytical modeling of monolayer graphene-based NO<sub>2</sub> sensor," *Sensor Letters*, vol. 11, no. 2, pp. 270–275, 2013.

## Research Article

# Thermodynamic and Theoretical Study of the Preparation of New Buckyballs from Corannulene, Coronene, and Circulene

Hasan R. Obayes,<sup>1</sup> Ghadah H. Alwan,<sup>2</sup> Ahmed A. Al-Amiery,<sup>1,3</sup>  
Abdul Amir H. Kadhum,<sup>3</sup> and Abu Bakar Mohamad<sup>3</sup>

<sup>1</sup> Applied Chemical Division, Applied Science Department, University of Technology, Baghdad, Iraq

<sup>2</sup> Ministry of Sciences and Technology, Industrial Research & Development Directorate, Industrial Applications Center, Baghdad, Iraq

<sup>3</sup> Department of Chemical and Process Engineering, Faculty of Engineering and Built Environment, Universiti Kebangsaan Malaysia, 43600 Bangi, Selangor, Malaysia

Correspondence should be addressed to Ahmed A. Al-Amiery; [dr.ahmed1975@gmail.com](mailto:dr.ahmed1975@gmail.com)

Received 29 July 2013; Revised 16 September 2013; Accepted 7 October 2013

Academic Editor: Mohammad Taghi Ahmadi

Copyright © 2013 Hasan R. Obayes et al. This is an open access article distributed under the Creative Commons Attribution License, which permits unrestricted use, distribution, and reproduction in any medium, provided the original work is properly cited.

We applied density functional theory (DFT) to study three polycyclic aromatic compounds (PAHs), corannulene, coronene, and circulene, for the preparation of twelve new buckyballs with molecular dimensions of less than a nanometer. The results showed that the corannulene molecule is bowl-shaped, the coronene molecule is planar, and the circulene molecule has a unique saddle-shaped structure. Cyclic polymerization of the three molecules can be used to prepare new buckyballs, and this process produces hydrogen molecules. The most symmetric buckyball is also the most stable based on the values of the HOMO energy levels and has the most efficient gap energy, making it potentially useful for solar cell applications.

## 1. Introduction

Polycyclic aromatic hydrocarbons (PAHs) are a class of unique compounds that consist of fused, conjugated aromatic rings that do not contain heteroatoms or carry substituents [1]. Alternate PAHs contain only six-membered rings, and certain alternant PAHs are called “benzenoid” PAHs. “Small” and “large” PAHs contain up to or more than six fused aromatic rings, respectively. Most research has focused on small PAHs due to their availability [2]. Corannulene has the shape of a bowl because it contains a five-membered ring, which inverts rapidly. In addition to its nonstandard geometry and dynamic behavior, this molecule has attracted considerable interest as an important building block for the synthesis of C<sub>53</sub>. Additionally, the solid state packing behavior of corannulene is interesting [3]. As discussed in detail by Kawasa and Kurata, [4] not only bowl-shaped but also ball- and belt-shaped aromatic systems provide an exciting opportunity to study concave-convex interactions. Coronene (6-circulene) is an aromatic planar symmetric molecule, which has been studied, synthesized, and well characterized [5].

Both corannulene and coronene have interesting conductive properties due to their large electronic resonance. Circulene, the next member of this molecular family, consists of a central cyclooctatetraene fragment surrounded by phenyl rings. Despite the efforts of researchers [6], circulene has not yet been synthesized. Several theoretical studies [7], but no detailed studies, have been carried out on the structure of this molecule. Theoretical predictions of the existence of buckyball molecules appeared in the late 1960s and early 1970s, but these predictions were largely unnoticed. The discovery of buckyballs was unexpected because the scientists were producing carbon plasmas to replicate and characterize unidentified interstellar matter. Mass spectrometry analysis of their product indicated the formation of spheroidal carbon molecules [8].

## 2. The Calculation Method

To calculate ground-state geometries, Gaussian 03, Revision C.01 [9] was optimized to a local minimum without

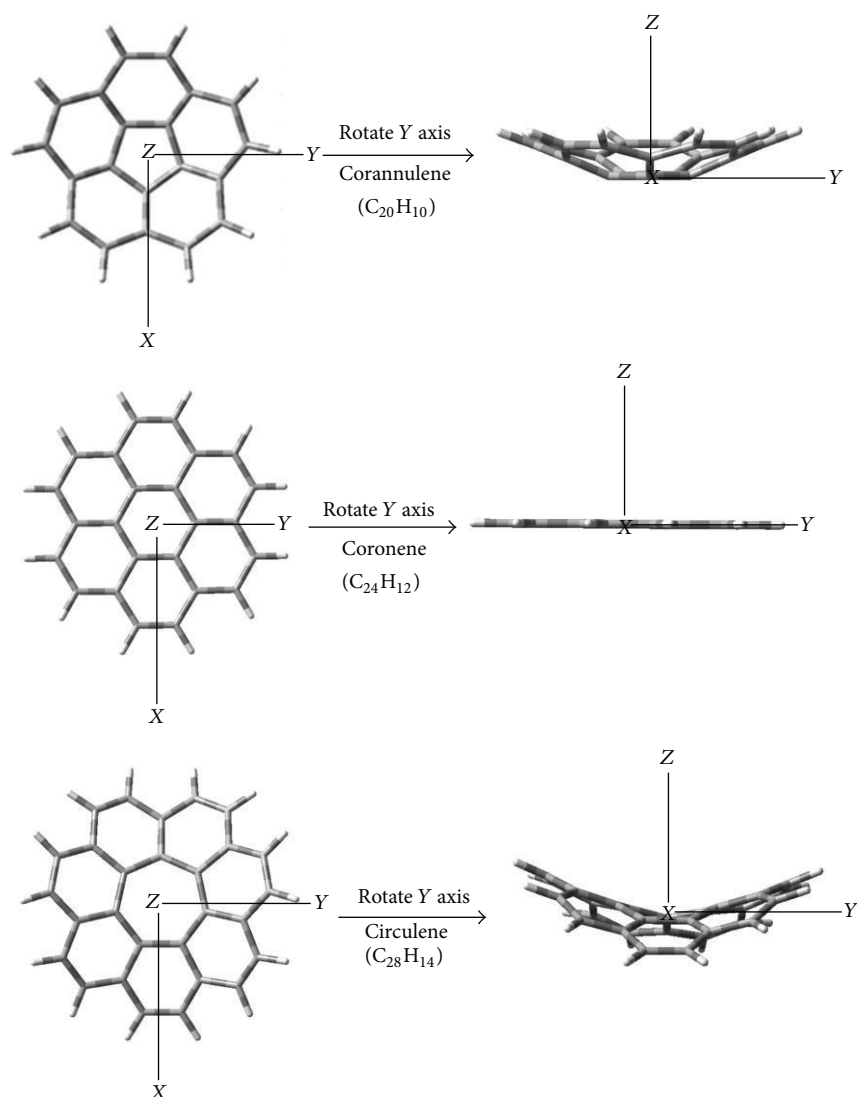


FIGURE 1: B3LYP/6-31G optimized structures of corannulene, coronene, and circulene.

symmetry restrictions using basis set 6-31G [10, 11]. The combination of the Becke three-parameter hybrid (B3) [12, 13] exchange functional and the Lee-Yang-Parr (LYP) [14] correlation functional (B3LYP) [15, 16] was used for all geometry optimizations, thermodynamic functions (at 298.150 Kelvin and 1.0 atm), Highest Occupied Molecular Orbital Energies ( $E_{\text{HOMO}}$ ), Lowest Unoccupied Molecular Orbital Energies ( $E_{\text{LUMO}}$ ), and physical properties for the molecules in this study.

### 3. Results and Discussion

Previous studies have shown that not all polycyclic aromatic hydrocarbons (PAHs) are flat molecules. We selected aromatic compounds known as circulenes for this study. The circulenes include 5-circulene (corannulene), 6-circulene (coronene), and 7-circulene (circulene). According to Density Function Theory (DFT) calculations, not all of these

molecules are flat, as shown in Figure 1. Corannulene is bowl-shaped, coronene is planar, and circulene has a unique saddle-shaped structure, which are consistent with the literature.

**3.1. Density Function Theory (DFT).** A DFT calculation introduces an additional step to each major phase of a Hartree-Fock calculation. This additional step is a numerical integration of the functional (or various derivatives of the functional). Thus, in addition to the sources of numerical error in Hartree-Fock calculations (integral accuracy, SCF convergence, and CPHF convergence), the accuracy of DFT calculations also depends on the number of points used in the numerical integration. The “fine” integration grid is the default in Gaussian 03. This grid greatly enhances the calculation accuracy at minimal additional cost. We do not recommend using a smaller grid in production DFT calculations. It is important to use the same grid for all calculations when energies will be compared (e.g., computing

		$\Delta_r H$ (kcal·mol <sup>-1</sup> )	$\Delta_r S$ (cal·mol <sup>-1</sup> ·K <sup>-1</sup> )	$\Delta_r G$ (kcal·mol <sup>-1</sup> )
3(C <sub>20</sub> H <sub>10</sub> ) Corannulene	1 → Buckyball C <sub>60</sub> H <sub>2</sub> (I) + 14H <sub>2</sub>	-79.114	+271.255	-159.989
	2 → Buckyball C <sub>60</sub> H <sub>2</sub> (II) + 14H <sub>2</sub>	-78.311	+267.663	-158.115
	3 → Buckyball C <sub>60</sub> H <sub>2</sub> (III) + 14H <sub>2</sub>	-80.844	+270.005	-161.346
	4 → Buckyball C <sub>60</sub> H <sub>2</sub> (IV) + 14H <sub>2</sub>	-75.196	+265.705	-154.416

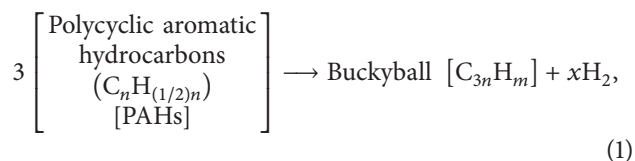
SCHEME 1: The reaction of formation of buckyball C<sub>60</sub>H<sub>2</sub> from three molecules of corannulene and the values of the change of enthalpy ( $\Delta_r H$ ), the change of entropy ( $\Delta_r S$ ), and the change of Gibbs energy ( $\Delta_r G$ ).

		$\Delta_r H$ (kcal·mol <sup>-1</sup> )	$\Delta_r S$ (cal·mol <sup>-1</sup> ·K <sup>-1</sup> )	$\Delta_r G$ (kcal·mol <sup>-1</sup> )
3(C <sub>24</sub> H <sub>12</sub> ) Coronene	1 → Buckyball C <sub>72</sub> (I) + 18H <sub>2</sub>	-111.781	+370.563	-222.264
	2 → Buckyball C <sub>72</sub> (II) + 18H <sub>2</sub>	-100.742	+364.235	-209.339
	3 → Buckyball C <sub>72</sub> (III) + 18H <sub>2</sub>	-99.535	+362.512	-207.618
	4 → Buckyball C <sub>72</sub> (IV) + 18H <sub>2</sub>	-99.911	+363.072	-208.161

SCHEME 2: The reaction of formation of buckyball C<sub>72</sub> from three molecules of coronene and the values of  $\Delta_r H$ ,  $\Delta_r S$  and  $\Delta_r G$ .

energy differences, heats of formation, and so forth). Larger grids are available, for example, for tight optimization of certain systems. An alternate grid may be selected in the route section [17–20].

To prepare new buckyballs, a fundamental understanding of the polymerization of polycyclic aromatic hydrocarbons (PAHs) is important. The polymerization process for new buckyballs revealed the production of hydrogen molecules [21, 22], and the general reaction of formation of new buckyballs from three molecules of polycyclic aromatic hydrocarbons (PAHs) is as follows,



where  $n$  is number of carbon atoms,  $x$  is  $(3/4)n - (1/2)m$ ,  $m$  is 2 in corannulene and circulene, and  $m$  is 0 in coronene.

**3.1.1. The Cyclic Polymerization of Three Corannulene Molecules.** Scheme 1 shows all possible cyclic polymerization reactions of three molecules of corannulene. Reaction (1) produced a new buckyball C<sub>60</sub>H<sub>2</sub> (I) by forming five butagons, three pentagons, three hexagons, and two decagon cycles from three corannulene molecules. Reaction (2) produced a new buckyball C<sub>60</sub>H<sub>2</sub> (II) through the formation of three butagons, five pentagons, three hexagons, and two nonagon cycles. Reaction (3) produced a new buckyball C<sub>60</sub>H<sub>2</sub> (III) by forming three butagons, three pentagons, five hexagons,

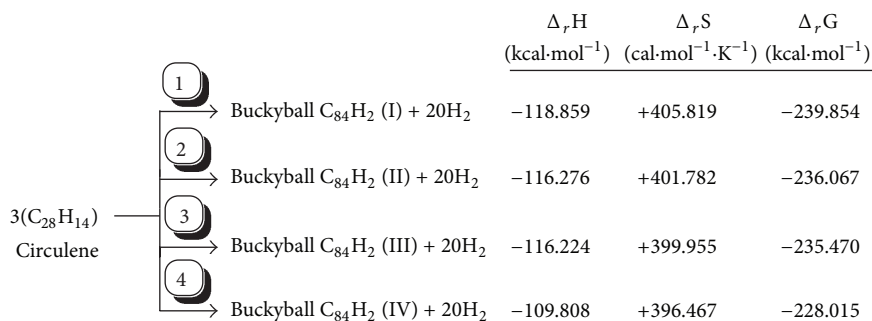
and two octagon cycles. Reaction (4) produced a new buckyball C<sub>60</sub>H<sub>2</sub> (IV) by forming eleven pentagons and two nonagon cycles. Thirteen different cycles were formed in these four reactions. All of these reactions are spontaneous and exothermic according to the values of the entropy change ( $\Delta_r S$ ), the Gibbs energy change ( $\Delta_r G$ ), and the enthalpy change ( $\Delta_r H$ ). The results for the E<sub>HOMO</sub> (the Energy of High Occupied Molecular Orbital) and the total energy for the four reaction products in Table 1 reveal that the products are stable, that the new buckyball C<sub>60</sub>H<sub>2</sub> (IV) is the most stable among the four, and that the increase in the E<sub>HOMO</sub> for C<sub>60</sub>H<sub>2</sub> (IV) is (-0.4530 eV), (-0.6177 eV), and (-0.6236 eV) relative to C<sub>60</sub>H<sub>2</sub> (I), C<sub>60</sub>H<sub>2</sub> (II), and C<sub>60</sub>H<sub>2</sub> (III) respectively. Additionally, the increase in the total energy is -0.1978 a.u or -124.121 KCal·mol<sup>-1</sup>, -0.1365 a.u or -85.655 KCal·mol<sup>-1</sup>, and -0.2260 a.u or -141.817 KCal·mol<sup>-1</sup> for C<sub>60</sub>H<sub>2</sub> (I), C<sub>60</sub>H<sub>2</sub> (II), and C<sub>60</sub>H<sub>2</sub> (III), respectively. The structures of the four new buckyballs are shown in Figure 2.

The molecular dimensions of the four new buckyballs are as follows: C<sub>60</sub>H<sub>2</sub> (I)—(0.85  $x$ -axis, 0.75  $y$ -axis, and 0.52  $z$ -axis) nm, C<sub>60</sub>H<sub>2</sub> (II)—(0.83  $x$ -axis, 0.73  $y$ -axis, and 0.49  $z$ -axis) nm, C<sub>60</sub>H<sub>2</sub> (III)—(0.84  $x$ -axis, 0.72  $y$ -axis, and 0.48  $z$ -axis) nm, and C<sub>60</sub>H<sub>2</sub> (IV)—(0.84  $x$ -axis, 0.73  $y$ -axis, and 0.48  $z$ -axis) nm.

**3.1.2. The Cyclic Polymerization of Three Molecules of Coronene.** Scheme 2 shows all possible cyclic polymerization reactions of three molecules of coronene. Reaction (1) produced a new buckyball C<sub>72</sub> (I) and forms nine butagons, six hexagons, and two nonagon cycles from the three

TABLE I: Physical values of all new buckyballs were calculated with B3LYP/6-31G.

Molecules	Total energy a.u.	Enthalpy (H) Kcal·mol <sup>-1</sup>	Entropy (S) Cal·mol <sup>-1</sup> ·K <sup>-1</sup>	E <sub>HOMO</sub> eV	E <sub>LUMO</sub> eV	Gap energy (E <sub>LUMO</sub> - E <sub>HOMO</sub> ) eV
Hydrogen molecule (H <sub>2</sub> )	-1.1755	7.847	31.132	-11.8086	+2.7235	14.5321
Corannulene	-767.9696	154.105	103.100	-6.0170	-1.5783	4.4387
Buckyball C <sub>60</sub> H <sub>2</sub> (I)	-2286.0419	273.343	144.707	-5.4453	-3.9097	1.5356
Buckyball C <sub>60</sub> H <sub>2</sub> (II)	-2286.1032	274.146	141.115	-5.2806	-3.9288	1.3518
Buckyball C <sub>60</sub> H <sub>2</sub> (III)	-2286.0137	271.613	143.457	-5.2747	-4.2510	1.0237
Buckyball C <sub>60</sub> H <sub>2</sub> (IV)	-2286.2397	277.261	139.157	-5.8983	-3.7968	2.1015
Coronene	-921.6885	185.772	115.845	-5.4880	-1.4049	4.0831
Buckyball C <sub>27</sub> (I)	-2741.7592	304.289	157.722	-4.9922	-3.9154	1.0768
Buckyball C <sub>27</sub> (II)	-2742.1237	315.328	151.394	-5.2425	-4.1043	1.1382
Buckyball C <sub>27</sub> (III)	-2741.9284	316.535	149.671	-5.0902	-4.2567	0.8335
Buckyball C <sub>27</sub> (IV)	-2742.1856	316.159	150.231	-5.7024	-3.3212	2.3812
Circulene	-1075.2072	216.027	132.547	-5.1430	-1.4348	3.7082
Buckyball C <sub>84</sub> H <sub>2</sub> (I)	-3199.7795	372.282	180.179	-5.2175	-3.6338	1.5837
Buckyball C <sub>84</sub> H <sub>2</sub> (II)	-3199.9262	374.865	176.142	-5.2404	-3.7780	1.4624
Buckyball C <sub>84</sub> H <sub>2</sub> (III)	-3199.9163	374.917	174.315	-5.0417	-4.0741	0.9676
Buckyball C <sub>84</sub> H <sub>2</sub> (IV)	-3200.2067	381.333	170.827	-5.7372	-3.8110	1.9262

SCHEME 3: The reaction of formation of C<sub>84</sub>H<sub>2</sub> buckyballs from three molecules of circulene and the values of  $\Delta_r H$ ,  $\Delta_r S$  and  $\Delta_r G$ .

coronene molecules. Reaction (2) produced a new buckyball C<sub>72</sub> (II) by forming three butagons, ten pentagons, two hexagons, and two octagon cycles. Reaction (3) produced a new buckyball C<sub>72</sub> (III) and formed two butagons, ten pentagons, three hexagons, and two heptagon cycles. Reaction (4) produced a new buckyball C<sub>72</sub> (IV) and formed six butagons, and eleven hexagon cycles. Seventeen cycles were formed in each reaction. Every reaction is spontaneous and exothermic according to the values of  $\Delta_r S$ ,  $\Delta_r G$ , and  $\Delta_r H$ . The E<sub>HOMO</sub> and the total energy for the four reaction products in Table I reveal that the products are stable, that the new buckyball C<sub>72</sub> (IV) is the most stable among the four, and that the increase in E<sub>HOMO</sub> for C<sub>72</sub> (IV) is (-0.7102 eV), (-0.4599 eV), and (-0.6122 eV) relative to new buckyballs C<sub>72</sub> (I), C<sub>72</sub> (II) and C<sub>72</sub> (III), respectively. Additionally, the increases in total energy are -0.4264 a.u or -267.570 KCal·mol<sup>-1</sup>, -0.0619 a.u or -38.843 KCal·mol<sup>-1</sup>, and -0.2572 a.u or -161.395 KCal·mol<sup>-1</sup> for new buckyballs

C<sub>72</sub> (I), C<sub>72</sub> (II), and C<sub>72</sub> (III), respectively. The structures of the four new buckyballs are shown in Figure 3.

The molecular dimensions of all four new C<sub>72</sub> buckyballs are as follows: C<sub>72</sub> (I)—(0.82 *x*-axis, 0.80 *y*-axis, and 0.52 *z*-axis) nm, C<sub>72</sub> (II)—(0.83 *x*-axis, 0.78 *y*-axis, and 0.55 *z*-axis) nm, C<sub>72</sub> (III)—(0.88 *x*-axis, 0.77 *y*-axis, and 0.55 *z*-axis) nm, and C<sub>72</sub> (IV)—(0.82 *x*-axis, 0.79 *y*-axis, and 0.56 *z*-axis) nm.

**3.1.3. The Cyclic Polymerization for Three Molecules of Circulene.** Scheme 3 shows all possible cyclic polymerization reactions of three molecules of circulene. Reaction (1) produced a new buckyball C<sub>84</sub>H<sub>2</sub> (I) by forming seven butagons, five pentagons, five hexagons, and two decagon cycles from three circulene molecules. Reaction (2) produced a new buckyball C<sub>84</sub>H<sub>2</sub> (II) by forming five butagons, seven pentagons, five hexagons, and two nonagon cycles. Reaction (3) produced

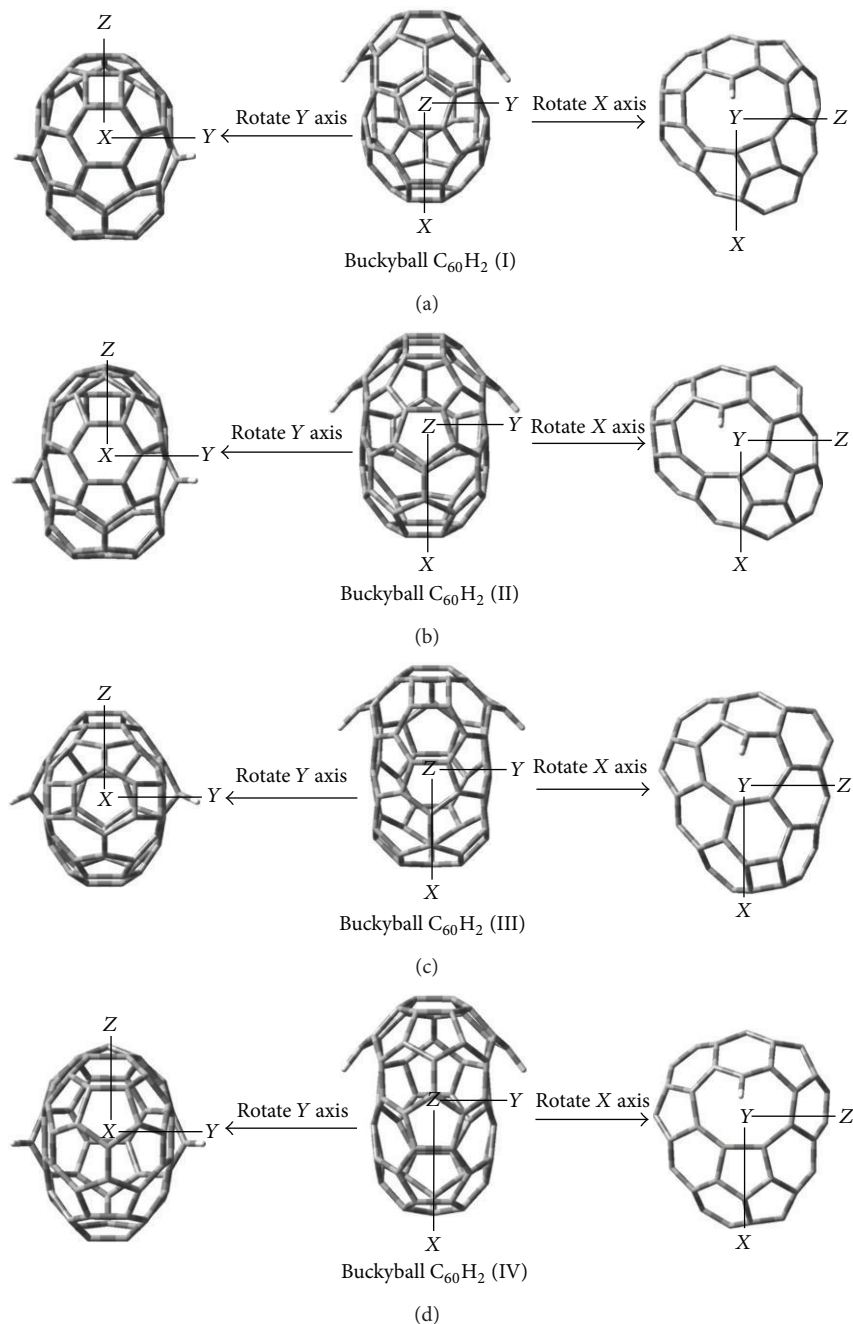


FIGURE 2: B3LYP/6-31G optimized structures of four new buckyballs:  $C_{60}H_2$  (I),  $C_{60}H_2$  (II),  $C_{60}H_2$  (III), and  $C_{60}H_2$  (IV).

a new buckyball  $C_{84}H_2$  (III) and formed five butagons, five pentagons, seven hexagons, and two octagon cycles. Reaction (4) produced a new buckyball  $C_{84}H_2$  (IV), seventeen pentagons, and two nonagon cycles. Nineteen different cycles were formed in each reaction. All of these reactions are spontaneous and exothermic according to the values of the change of entropy ( $\Delta_r S$ ), the change of Gibbs energy ( $\Delta_r G$ ), and the change of enthalpy ( $\Delta_r H$ ). However, the the Energy of the Highest Occupied Molecular Orbital ( $E_{HOMO}$ ) and the total energy for the reaction products in Table 1 reveal that the product has more stability, in this state the product

new buckyball  $C_{84}H_2$  (IV), most stable among the four new buckyballs, was  $C_{84}H_2$  (IV) with an increase in the  $E_{HOMO}$ , that is ( $-0.5197$  eV), ( $-0.4968$  eV), and ( $-0.6955$  eV) relative to  $C_{84}H_2$  (I),  $C_{84}H_2$  (II), and  $C_{84}H_2$  (III), respectively. Additionally, the increases in total energy are  $-0.4272$  a.u or  $-268.072$   $KCal \cdot mol^{-1}$ ,  $-0.2805$  a.u or  $-176.016$   $KCal \cdot mol^{-1}$ , and  $-0.2904$  a.u or  $-182.228$   $KCal \cdot mol^{-1}$  relative to  $C_{84}H_2$  (I),  $C_{84}H_2$  (II) and  $C_{84}H_2$  (III), respectively. The structures of the four new  $C_{84}H_2$  buckyballs are shown in Figure 4. The molecular dimensions of all four new  $C_{84}H_2$  buckyballs are as follows:  $C_{84}H_2$  (I)—( $0.86$   $x$ -axis,  $0.85$   $y$ -axis, and

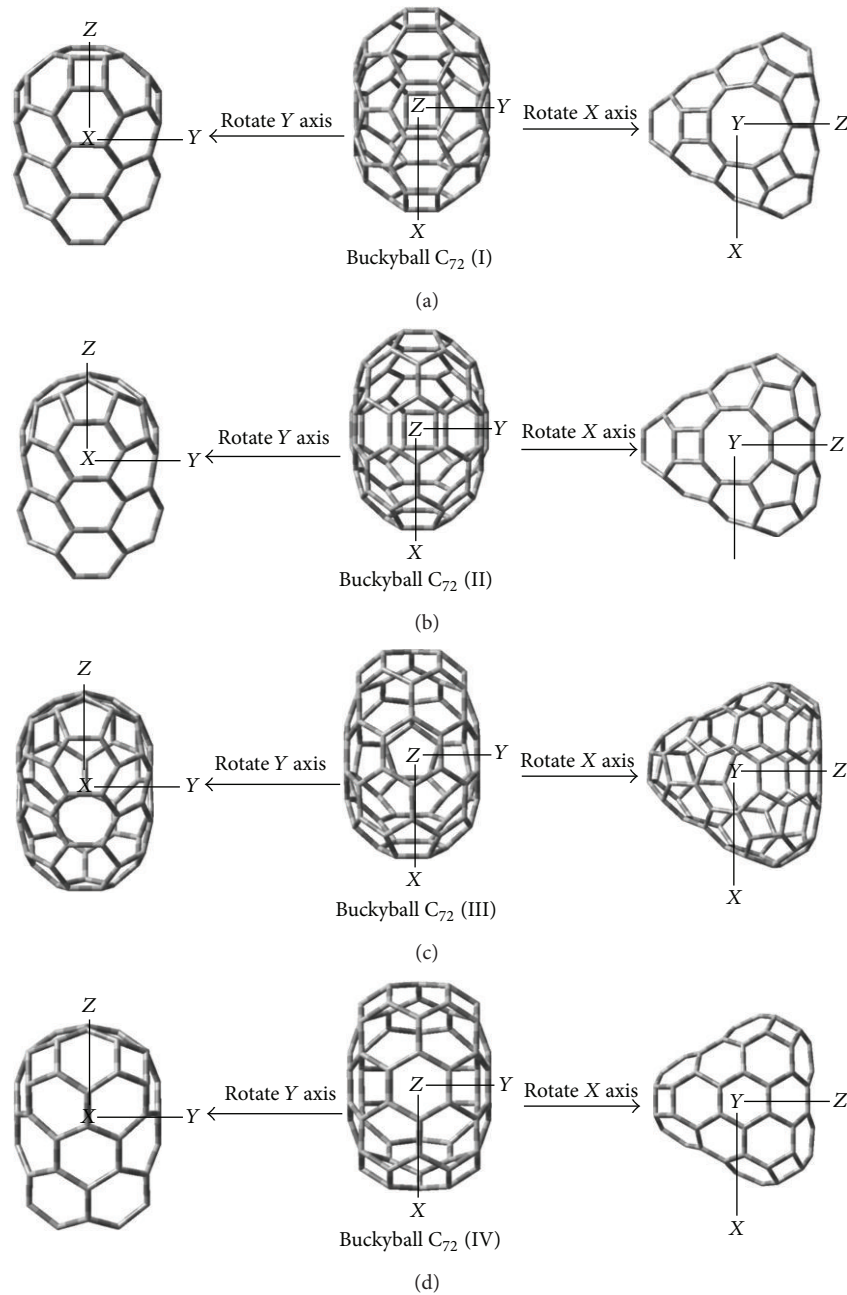


FIGURE 3: B3LYP/6-31G optimized structures of new buckyballs  $C_{72}$  (I),  $C_{72}$  (II),  $C_{72}$  (III), and  $C_{72}$  (IV).

0.66 z-axis) nm,  $C_{84}H_2$  (II)—(0.90 x-axis, 0.88 y-axis, and 0.61 z-axis) nm,  $C_{84}H_2$  (III)—(0.89 x-axis, 0.87 y-axis, and 0.60 z-axis) nm, and  $C_{84}H_2$  (IV)—(0.90 x-axis, 0.87 y-axis, and 0.60 z-axis) nm.

**3.2. Energy Gap.** The energy gap, which is also called the band gap, is an energy range in a solid where no electron states can exist. The gap energy generally refers to the energy difference (in electron volts) between the Lowest Unoccupied Molecular Orbital (LUMO) and the Highest Occupied Molecular Orbital (HOMO) in insulators and semiconductors. This gap energy is equivalent to the energy required to free an outer

shell electron from its orbit about the nucleus to become a mobile charge carrier that moves freely within the solid material. The band gap is a major factor that determines the electrical conductivity of a solid. Substances with large gap energies are generally insulators, materials with smaller gap energies are semiconductors, and conducting materials have very small or no gaps energies. The Shockley-Queisser limit gives the maximum possible efficiency of single junction solar cells under unconcentrated sunlight as a function of the semiconductor band gap. If the band gap is too high, then the material cannot absorb most daylight photons; if the band gap is too low, then most photons have much more energy than

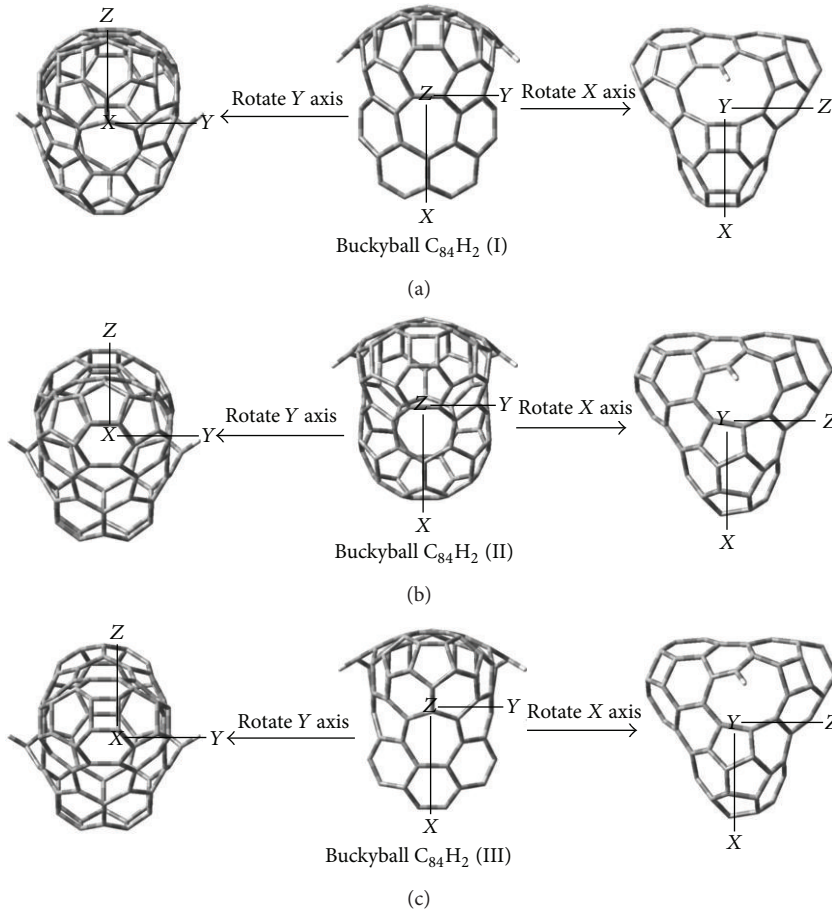


FIGURE 4: B3LYP/6-31G optimized structures of new buckyballs  $C_{84}H_2$  (I), buckyballs  $C_{84}H_2$  (II),  $C_{84}H_2$  (III), and  $C_{84}H_2$  (IV).

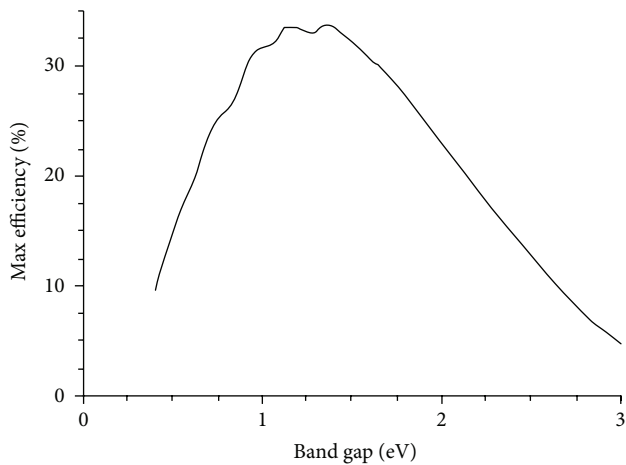


FIGURE 5: The Shockley-Queisser limit for the energy efficiency of a gap.

is necessary to excite electrons across the band gap, and the rest is wasted. The semiconductors that are used commonly in commercial solar cells have band gaps near the peak of this curve shown in Figure 5.

In Table 1, the values of the energy gaps for all buckyballs in the (0.8335–2.3812) eV range, arranged by the increases in energy gap, are as follows:

- Buckyball  $C_{27}$  (III) < Buckyball  $C_{84}H_2$  (III)
- < Buckyball  $C_{60}H_2$  (III)
- < Buckyball  $C_{27}$  (I)
- < Buckyball  $C_{27}$  (II)
- < Buckyball  $C_{60}H_2$  (II)
- < Buckyball  $C_{84}H_2$  (II) (2)
- < Buckyball  $C_{60}H_2$  (I)
- < Buckyball  $C_{84}H_2$  (I)
- < Buckyball  $C_{84}H_2$  (IV)
- < Buckyball  $C_{60}H_2$  (IV)
- < Buckyball  $C_{27}$  (IV).

## 4. Conclusions

A quantum chemistry calculation is performed using the Density Function Theory (DFT) method to study the preparation of twelve new buckyballs from the cyclic polymerization of three polycyclic aromatic hydrocarbons (PAHs), corannulene, coronene, and circulene, and the production of hydrogen molecules. The results obtained for the new buckyballs show that the most symmetric buckyball is the most stable, depending on the values of  $E_{\text{HOMO}}$ . The molecular dimensions of all the new buckyballs are less than a nanometer, and the new buckyballs are characterized by the high efficiency of their energy gaps.

## Conflict of Interests

The authors declare that there is no conflict of interests regarding the publication of this paper.

## References

- [1] J. C. Fetzer, *The Chemistry and Analysis of the Large Polycyclic Aromatic Hydrocarbons*, John Wiley, New York, NY, USA, 2000.
- [2] X. Feng, W. Pisula, and K. Müllen, "Large polycyclic aromatic hydrocarbons: synthesis and discotic organization," *Pure and Applied Chemistry*, vol. 81, no. 12, pp. 2203–2224, 2009.
- [3] Y. T. Wu and J. S. Siegel, "Aromatic molecular-bowl hydrocarbons: synthetic derivatives, their structures, and physical properties," *Chemical Reviews*, vol. 106, pp. 4843–4867, 2006.
- [4] T. Kawasa and H. Kurata, "Ball-, bowl-, and belt-shaped conjugated systems and their complexing abilities: exploration of the concave-Convex  $\pi$ - $\pi$  interaction," *Chemical Reviews*, vol. 106, pp. 5250–5273, 2006.
- [5] J. C. Hanson and C. E. Nordman, "The crystal and molecular structure of corannulene,  $\text{C}_{20}\text{H}_{10}$ ," *Acta Crystallographica*, vol. B32, p. 1147, 1976.
- [6] K. Yano, M. Osatani, and K. Tani, "On attempted synthesis of 8-shaped circulene: synthesis and characterization of [2,2](4,4')-biphenyl-(3,11)-dibenzo[*c*,*l*]chrysenophane and its cyclophadiene," *Bulletin of the Chemical Society of Japan*, vol. 73, pp. 185–189, 2000.
- [7] T. Liljefors and O. Wennerstrom, "Molecular mechanics calculations on the structures and conformational properties of [8]circulene and some related phane compounds," *Tetrahedron*, vol. 33, no. 22, pp. 2999–3003, 1977.
- [8] E. A. Katz, "Fullerene thin films as photovoltaic material," in *Nanostructured Materials for Solar Energy Conversion*, pp. 361–443, Elsevier, 2006.
- [9] J. A. Pople, M. J. Frisch, G. W. Trucks et al., "Gaussian Inc., 2004 Gaussian 03W (Revision C.01)," Gaussian Inc., Wallingford, Conn, USA, 2003.
- [10] W. J. Pietro, M. M. Francl, W. J. Hehre, D. J. Defrees, J. A. Pople, and J. S. Binkley, "Self-consistent molecular orbital methods. 24. Supplemented small split-valence basis sets for second-row elements," *Journal of the American Chemical Society*, vol. 104, no. 19, pp. 5039–5048, 1982.
- [11] K. D. Dobbs and W. J. Hehre, "Molecular orbital theory of the properties of inorganic and organometallic compounds 5. Extended basis sets for first-row transition metals," *Journal of Computational Chemistry*, pp. 861–879, 1987.
- [12] A. D. Becke, "Density-functional exchange-energy approximation with correct asymptotic behavior," *Physical Review*, vol. 38, pp. 3098–3100, 1988.
- [13] A. D. Becke, "Density-functional thermochemistry—III. The role of exact exchange," *The Journal of Chemical Physics*, vol. 98, no. 7, pp. 5648–5652, 1993.
- [14] C. Lee, W. Yang, and R. G. Parr, "Development of the Colle-Salvetti correlation-energy formula into a functional of the electron density," *Physical Review*, vol. 37, pp. 785–789, 1988.
- [15] A. A. Al-Amiery, H. D. Jaffar, H. R. Obayes et al., "Thermodynamic studies on 4-aminocoumarin tautomers," *International Journal of Electrochemical Science*, vol. 7, pp. 8468–8472, 2012.
- [16] J. H. Naama, G. H. Alwan, H. R. Obayes et al., "Curcuminoids as antioxidants and theoretical study of stability of curcumin isomers in gaseous state," *Research on Chemical Intermediates*, vol. 39, no. 9, pp. 4047–4059, 2013.
- [17] A. D. Becke, "Density-functional thermochemistry—V. Systematic optimization of exchange-correlation functionals," *Journal of Chemical Physics*, vol. 107, no. 20, pp. 8554–8560, 1997.
- [18] S. W. Benson, *Thermochemical Kinetics*, Wiley and Sons, New York, 1968.
- [19] R. Berger and M. Klessinger, "Algorithms for exact counting of energy levels of spectroscopic transitions at different temperatures," *Journal of Computational Chemistry*, vol. 18, no. 10, pp. 1312–1319, 1997.
- [20] G. Zheng, H. A. Witek, P. Bobadova-Parvanova et al., "Parameter calibration of transition-metal elements for the spin-polarized self-consistent-charge density-functional tight-binding (DFTB) Method: Sc, Ti, Fe, Co, and Ni," *Journal of Chemical Theory and Computation*, vol. 3, no. 4, pp. 1349–1367, 2007.
- [21] H. R. Obayes, "Theoretical study for the preparation of new buckyballs from the cyclic dimerization reaction of two molecules corannulene, coronene and circulene aromatic compounds," *Journal of Engineering & Technology*, vol. 31, no. 5, pp. 594–602, 2013.
- [22] H. R. Obayes, A. A. Al-Amiery, H. D. Jaffar et al., "Theoretical study for the preparation of sub-carbon nano tubes from the cyclic polymerization reaction of two molecules from corannulene, coronene and circulene aromatic compounds," *Journal of Computational and Theoretical Nanoscience*, vol. 10, pp. 2459–2463, 2013.